
ETD Archive

2018

Limits of Small Scale Pressure Swing Adsorption

Aaron A. Moran
Cleveland State University

Follow this and additional works at: <https://engagedscholarship.csuohio.edu/etdarchive>

 Part of the [Chemical Engineering Commons](#)

[How does access to this work benefit you? Let us know!](#)

Recommended Citation

Moran, Aaron A., "Limits of Small Scale Pressure Swing Adsorption" (2018). *ETD Archive*. 1050.
<https://engagedscholarship.csuohio.edu/etdarchive/1050>

This Dissertation is brought to you for free and open access by EngagedScholarship@CSU. It has been accepted for inclusion in ETD Archive by an authorized administrator of EngagedScholarship@CSU. For more information, please contact library.es@csuohio.edu.

LIMITS OF SMALL SCALE PRESSURE SWING ADSORPTION

AARON A. MORAN

Bachelor of Science in Chemical Engineering

Miami University

May 2012

Master of Science in Chemical Engineering

Cleveland State University

June 2014

Submitted in partial fulfillment of requirements for the degree

DOCTOR OF ENGINEERING

at the

CLEVELAND STATE UNIVERSITY

May 2018

ACKNOWLEDGEMENTS

First and foremost, I would like to offer my sincerest gratitude to Dr. Talu for encouraging me to pursue my doctoral degree and for all his support along this journey. I am extremely grateful for his willingness to allow me to pursue a topic that excited me, despite it not always being his favorite. Without a doubt, I would not be the scientist/engineer I am today without him. Not only has he taught me how to be a better experimentalist and researcher, but he also significantly enhanced my teaching ability. The wide ranging advice he has given me over the years has been invaluable and I will never forget it.

Next, I would like to thank my committee, Dr. Gatica, Dr. Wirth, Dr. Ungarala, and Dr. Fodor for their input and critique of my thesis. Dr Ungarala deserves additional acknowledgement for allowing use of the PSA model he developed, which was instrumental in the data analysis and improving my understanding of the PSA process. Dr. Thrash, Dr. Shah, and Dr. Gumma have also provided valuable input on various papers and presentations along the way of which I am very grateful. Finally, I would like to thank Dr. Belovich for her guidance and mentoring during my three years as a teaching assistant under her.

Additionally, I wish to thank Jim Barker for his help with the electrical side of the setup of the PSA process used in this thesis and wish him all the best in his retirement. Becky Laird and Darlene Montgomery deserve extra thanks for all the help they have provided during my time at CSU. I have also had the pleasure of mentoring several graduate students who have worked extremely hard and did excellent work (Mihir Patel,

Himabindu Gandra, Muhammet Köksal, and Philipp Schandelmaier). I would not have been able to finish this dissertation as quickly as I did without their assistance and patience with me as I tried my best to teach them what I know. Mihir and Qian Qian Zhou deserve special mention as well as some of the data used in the work was collected by them. Dustin Bowden also deserves acknowledgment for helping take the SEM images in this study.

Lastly, I would like to thank my family and friends for their love and support over the years I have undertaken this project. A special shout out goes out to my roommates Steve Cook and Mike Salem who put up with my often strange schedule and lack of social life. I finally must express my utmost gratitude to my parents for their love and encouragement throughout this process. Without their support in my times of need, I would not be in the position I am today.

LIMITS OF SMALL SCALE PRESSURE SWING ADSORPTION

AARON A. MORAN

ABSTRACT

Portable or small scale pressure swing adsorption (PSA) systems have gained increasing popularity in both industry and literature due to the commercial success of personal oxygen concentrators (POCs). While these processes have much in common with larger PSA systems, significant differences exist that make understanding process limitations difficult. These include faster cycle times, smaller adsorbent particles, and a reduced column size.

Macropore diffusion is traditionally assumed to control the mass transfer rate in columns packed with zeolite particles in an oxygen production process. While numerous studies have confirmed this assumption for the particle size used in industrial size PSA processes, it has not been validated for the much smaller particle size used in small scale PSA. Smaller particles improve the mass transfer rate by increasing interfacial area per volume as well as decreasing diffusion distance. Despite this reduction, small scale PSA simulations often still assume a mass transfer rate solely limited by macropore diffusion. This approach fails to adequately account for the influence of other mass transfer mechanisms whose impact increases due to particle size reduction. This study experimentally demonstrates the dominant mass transfer mechanism is no longer macropore diffusion for the particle size used in small scale PSA for oxygen production. Depending on the gas velocity, axial dispersion effects either become the limiting mechanism or equally as important as macropore diffusion. It also shows that improperly

accounting for axial dispersion effects has a significant impact on the mass transfer coefficient estimation, often measured with breakthrough experiments.

An important limitation for small scale PSA processes is the limit on adsorbent utilization. Decreasing cycle time for a PSA process typically results in a gain in adsorbent utilization, often represented in industry by the bed size factor (BSF). Increasing adsorbent utilization is represented by a decrease in BSF. A low BSF is desirable because it represents a smaller overall process size, which is highly attractive for portable systems. Currently, there is no consensus in literature if a lower limit for the BSF exists and what may cause it.

In this study, a two column small scale PSA process was used to measure the cycle time of a minimum BSF. It represents the first experimental literature example of a minimum BSF for a two column air separation process. The data was then used with a literature model to better understand why the minimum was occurring and what was primarily causing it. It was determined that macropore diffusional resistance is the primary cause of a minimum BSF.

TABLE OF CONTENTS

	Page
ABSTRACT.....	iv
LIST OF TABLES.....	xi
LIST OF FIGURES.....	xiii
NOMENCLATURE.....	xvi
CHAPTER	
I. INTRODUCTION.....	1
1.1. Purpose.....	1
1.2. Scope of Work.....	2
1.3. Intellectual Contributions.....	4
II. BACKGROUND.....	5
2.1 Zeolites.....	5
2.1.1 Zeolite History.....	6
2.1.2 Zeolite Composition and Structure.....	7
2.1.3 Zeolite Applications.....	11
2.2 Adsorption.....	13
2.2.1 Adsorption Fundamentals.....	13
2.2.2 Adsorption Thermodynamics.....	15
2.2.3 Diffusion in Microporous Adsorbents.....	16
2.3 Air Separation through Pressure Swing Adsorption.....	19
2.3.1 PSA Principles.....	19
2.3.2 History and Growth of PSA.....	21
2.3.3 Improvements to PSA Cycles.....	25

2.3.4	Air Separation Applications.....	27
2.3.5	Future Challenges for PSA.....	28
III.	THEORY.....	30
3.1	Intermolecular forces.....	30
3.1.1	Electrostatic Forces.....	31
3.1.2	Induction and Dispersion Forces.....	32
3.1.3	N ₂ and O ₂ Interaction with Zeolites.....	33
3.1.4	Exchangeable Cations.....	35
3.2	Adsorption Equilibrium Modeling.....	36
3.2.1	Henry's Law.....	37
3.2.2	The Langmuir Isotherm.....	37
3.2.3	Dual Site Langmuir Model.....	39
3.3	Adsorption Column Dynamics.....	41
3.3.1	Adsorption Rate.....	41
3.3.2	Axial Dispersion.....	43
IV.	CHALLENGES OF SMALL SCALE PSA.....	48
4.1	Effect of Particle Size Reduction in Small Scale PSA.....	48
4.1.1	Current Assumptions.....	49
4.1.2	MTC Estimation for Small Particles.....	51
4.1.3	Axial Dispersion Coefficient Estimation.....	53
4.1.4	Impact of Higher Axial Dispersion Effects with Small Particles.....	55
4.2	Small Scale PSA.....	58

4.2.1	Evolution of Small Scale PSA.....	59
4.2.2	Limitations of Small Scale PSA.....	60
4.3	Possible Causes of a Minimum BSF.....	61
4.3.1	Pressure Drop.....	61
4.3.2	Heat Transfer Limitations.....	63
4.3.3	Mass Transfer Limitations.....	63
4.3.4	BSF Model.....	64
4.4	Study Aims and Experimental Plan Overview.....	65
4.4.1	Study Aims.....	65
4.4.2	Overview of Experimental Plan.....	66
V.	MATERIAL AND METHODS.....	67
5.1	Type of Zeolite.....	67
5.2	Isotherms.....	68
5.3	Column Packing and Activation.....	70
5.4	Breakthrough Study.....	70
5.4.1	Breakthrough System.....	70
5.4.2	Breakthrough Measurements.....	71
5.4.3	Constant Pattern.....	73
5.4.4	MTC Calculation.....	74
5.4.5	van Deemter Model.....	77
5.5	PSA System.....	79
5.5.1	PSA Flow Diagrams.....	80

5.5.2	PSA Instrumentation, Process Control, and Data	
	Collection.....	83
5.5.3	System Design.....	85
5.5.4	Material Balances.....	87
5.5.5	Design Parameters.....	89
5.5.6	Performance Parameters.....	91
5.5.7	Pressure Drop Study.....	93
5.5.8	Minimum BSF Study.....	96
5.6	PSA Model Framework.....	100
5.6.1	Mass Balance.....	101
5.6.2	Equilibrium Model.....	101
5.6.3	Momentum Balance.....	102
5.6.4	Energy Balance.....	102
VI.	RESULTS AND DISCUSSION.....	103
6.1	Axial Dispersion Effects in Small Scale PSA.....	103
6.1.1	Experimental MTC Measurement.....	104
6.1.2	Mass Transfer Parameter Estimation.....	106
6.1.3	Rate Limiting Contribution.....	109
6.1.4	Skin Resistance.....	112
6.2	Role of Pressure Drop in Small Scale PSA.....	114
6.2.1	Experimental Results.....,,.....	114
6.2.2	Simulation Results.....	117
6.3	Adsorbent Utilization Limit in Small Scale PSA.....	127

6.3.1	Measurement of a Minimum BSF.....	127
6.3.2	What Causes a Minimum BSF?.....	133
VII.	CONCLUSIONS.....	136
7.1	On the Effects of Axial Dispersion in Small Scale PSA.....	136
7.2	On the Role of Pressure Drop in Small Scale PSA.....	137
7.3	On the Existence of a Minimum BSF.....	139
7.4	Summary of Intellectual Contributions.....	139
7.5	Future Work.....	140
	REFERENCES.....	141
	APPENDIX.....	153
A.	PSA Model.....	153
B.	Breakthrough Experiments.....	159
C.	PSA Pressure Drop Experiments.....	167
D.	Minimum BSF Experiments.....	170

LIST OF TABLES

Table	Page
3.1 Quadrupole Moment and Polarizabilities of Nitrogen and Oxygen Molecules....	34
4.1 Comparison of parameters used for estimates of $k_{overall}$ in Figure 4.2.....	57
5.1 Nitrogen and oxygen DSL parameters for LiLSX particles used in simulations..	69
5.2 Breakthrough column specifications.....	72
5.3 PSA schematic symbol description.....	82
5.4 Experimental column specifications for pressure drop study.....	95
5.5 Cycle specifications for short column cycles in pressure drop study.....	95
5.6 Cycle specifications for long column cycles in pressure drop study	96
5.7 Experimental column specifications for minimum BSF study.....	97
5.8 Cycle specifications for long column cycles with pressure ratio 3.5 in minimum BSF study.....	98
5.9 Cycle specifications for long column cycles with pressure ratio 3 in minimum BSF study	98
5.10 Cycle specifications for long column cycles with pressure ratio 2.5 in minimum. BSF study	99
5.11 Cycle specifications for short column cycles with pressure ratio 3.5 in minimum. BSF study	99
5.12 Cycle specifications for long column cycles with pressure ratio 3 in minimum BSF study	100
6.1 Comparison of van Deemter constants determined from experimental data and previously cited literature values.....	108

6.2	Comparison of equation 4.1 contributions for a nitrogen overall MTC at a... Reynolds number of 20 and two different particle sizes.....	111
6.3	Comparison of experimental and simulation results at similar cycle times and different column dimensions (Pressure drop study).....	118
6.4	Comparison of experimental and simulation results at different cycle times and. same column dimensions (Pressure drop study).....	122
6.5	Slope and intercept of k' vs. superficial velocity in Figure 6.18 for long columns.....	131
6.6	Slope and intercept of k' vs. superficial velocity in Figure 6.18 for short columns.....	131

LIST OF FIGURES

Figure	Page
2.1 Examples of zeolite basic secondary units.....	9
2.2 Sodalite unit with Si, Al atoms.....	9
2.3 Structure of Type A and Type X or Y zeolites.....,,.....	10
2.4 Potential energy diagram for adsorption.....	14
2.5 The five types of isotherms.....	15
2.6 Depiction of pores and mass transfer resistances in adsorbent particle.....	18
2.7 Basic two-column pressure swing adsorption system	24
2.8 Column pressure during Skarstrom cycle	25
3.1 Calculated potential energy curves of nitrogen and oxygen.....	34
3.2 Potential energy curves of Na^+N_2 and Li^+N_2	36
3.3 Mass transfer zone inside a column.....	45
3.4 Shapes of isotherms in determining the sharpness of concentration wavefront....	46
3.5 Self-sharpening wavefront and dispersive wavefront.....	46
3.6 Column breakthrough curve.....	47
4.1 Limiting Peclet number vs particle diameter for flow through packed beds.....	54
4.2 Comparison of predicted overall nitrogen MTC using constants and correlations according to Table 1.....	58
5.1 Oxygen isotherms for LiLSX zeolite.....	68
5.2 Nitrogen isotherms for LiLSX zeolite	69
5.3 Breakthrough experimental setup.....	72
5.4 Comparison of experiment and simulation breakthrough curve.....	77

5.5	PSA middle exit manifold schematic.....	80
5.6	PSA system feed side schematic.....	81
5.7	PSA system product side schematic	81
5.8	Comparison of isothermal capacity and working capacity in a PSA process.....	93
6.1	Experimental data vs. correlation predictions of the nitrogen overall MTC.....	105
6.2	HETP vs. superficial velocity from experimental breakthrough experiment.....	108
6.3	Experimental overall MTC plotted against overall nitrogen MTC predictions...	109
6.4	Comparison of $k_{overall}$ predictions for a 0.5 mm particle and 2 mm particle.....	111
6.5	SEM images of an extruded particle edge.....	113
6.6	SEM images of LiLSX particle used in this study.....	113
6.7	Comparison of oxygen recovery decline with increasing production step superficial velocity	116
6.8	Comparison of BSF with increasing production step superficial velocity for columns of different dimensions.....	117
6.9	Comparison of gas phase nitrogen composition at the end of the production step for the short columns and long columns	119
6.10	Comparison of gas phase nitrogen composition at the end of the purge step for the short columns and long columns.....	119
6.11	Comparison of solid nitrogen loading at the end of the production and purge steps for the short columns and long columns	121
6.12	Comparison of gas phase nitrogen composition at the end of the production step for the slow cycle and fast cycle	124

6.13	Comparison of gas phase nitrogen composition at the end of the purge step for the slow cycle and fast cycle	124
6.14	Comparison of solid nitrogen loading at the end of the production and purge steps for the slow cycle and fast cycle	125
6.15	Comparison of solid temperature profiles at the end of the production and purge steps.....	126
6.16	Oxygen recovery results for long, thin columns and short, wide columns.....	128
6.17	BSF results for long, thin columns and short, wide columns.....	128
6.18	k' plotted against superficial velocity of high pressure feed step for long, thin columns and short, wide columns.....	130
6.19	BSF plotted against superficial velocity of high pressure feed step for long columns	132
6.20	BSF plotted against superficial velocity of high pressure feed step for long columns (pressure ratio 3).....	134

NOMENCLATURE

b	adsorption equilibrium constant
b_i^0	pre-exponential constant (DSL model) for gas i for first site
c_i	gas phase concentration of species i ,
d	equilibrium constant for second site (DSL model)
d_i^0	pre-exponential constant (DSL model) for gas i for second site
d_p	adsorbent particle diameter
D_c	micropore diffusivity
D_L	axial dispersion coefficient
D_k	Knudsen gas diffusivity
D_m	molecular gas diffusivity
D_p	macropore diffusivity
E	potential energy
e	electron charge
F	instantaneous flow rate
\bar{F}	average flow rate
f	force
G	Gibbs free energy
g	ionic valences
H	enthalpy
h	distance between charges
j	number of components
K	dimensionless Henry's law constant
K_H	Henry's law constant

K_0	Henry's Law constant at a reference state
k	mass transfer coefficient
k'	empirical constant
k_a	adsorption rate constant
k_b	desorption rate constant
k_f	film mass transfer coefficient
$k_{overall}$	overall mass transfer coefficient
L	column length
L_{MTZ}	mass transfer zone length
M	quadrupole moment
MTZ_{time}	mass transfer zone time
N_i	total number of moles of component i
N_T	total number of moles of adsorbate
n_i^*	equilibrium value of adsorbed phase concentration of component i ,
n_i	average adsorbed phase concentration over an adsorbent particle of component i ,
n_s	saturation capacity
r_c	crystal radius
r_p	adsorbent particle radius
P	pressure
P_s	saturated vapor pressure
p	partial pressure
$Pé_\infty$	limiting Peclet number
Q	heat of adsorption
R	ideal gas constant

Re	Reynolds number
S	entropy
s	selectivity
Sc	Schmidt number
Sh	Sherwood number
T	temperature
t	time
t_c	time stoichiometric center exits column
t_{ct}	cycle time
s	selectivity
u	interstitial gas velocity
u_w	wave velocity
w	magnitude of charge
WC_{ideal}	isothermal working capacity
$x,$	mole fraction in the adsorbed phase
y	mole fraction in the fluid phase
z	axial coordinate

Greek Symbols

ε_0	dielectric permittivity
α	polarizability
θ	fractional surface coverage
ρ_b	column bulk density
ρ_p	particle density

ε_b	bed/column porosity
ε_p	particle macroporosity
γ_1, γ_2	axial dispersion constant
ϵ	error of material balance
μ_g	gas viscosity
ρ_g	gas density
τ_p	pore tortuosity

Commonly Used Abbreviations

BSF = bed size factor

CSS = cyclic steady state

DSL = dual-site Langmuir

LDF = linear driving force

LiLSX = lithium low silica X zeolite

MTC = mass transfer coefficient

MTZ = mass transfer zone

POC = personal oxygen concentrator

PSA = pressure swing adsorption

TPD = tons per day

CHAPTER I

INTRODUCTION

1.1 Purpose

The abundance of life on Earth depends on oxygen, which composes around 21% of our atmosphere. However, demand for high purity oxygen has risen tremendously to support new manufacturing processes and treat various medical conditions. Industrial uses for purified oxygen include steel production, chemicals, petrochemicals, glass, ceramics, and paper. The primary medical application is oxygen therapy for patients suffering from conditions such as asthma and COPD (Chronic Obstructive Pulmonary Disease).

Generating nearly pure oxygen from air is possible through either cryogenic distillation or pressure swing adsorption (PSA). The high energy cost of cryogenic distillation limits its economic viability to large scale oxygen demand or when > 96% oxygen is required. PSA cannot separate oxygen and argon, which limits the maximum oxygen purity to 96%. Since purity above 90% is acceptable for most personal

applications, PSA is the logical choice for small medical devices, often labeled personal oxygen concentrators (POCs). These small scale devices have numerous advantages over oxygen cylinders, the alternative option for oxygen therapy, including portability and permitted use on airplanes. However, the technology is not fully mature and opportunity remains to improve the size and efficiency of these devices. Creating a superior device is lucrative because the market for oxygen therapy in North America alone is expected to grow from around \$2.7 billion in 2014 to over \$7 billion in 2024. Moreover, COPD has been projected to become the third leading cause of death in the world by 2030, which further increases future need for oxygen therapy.¹

While large scale PSA processes are well researched, less is known about small scale operations. Significant differences exist between large and small scale processes that potentially change process limitations. The goal of this dissertation is characterizing and understanding these differences to improve the future design of POCs.

1.2 Scope of Work

The most significant difference between large and small scale processes, other than overall process size, is the smaller particle size used in the packed column(s). In literature, it is well known that diffusion in the macropores of the adsorbent is the primary mass transfer resistance in columns packed with large zeolite particles ($> 2\text{mm}$).² Despite little proof this applies to the particle size used in small scale processes, it is still often assumed as a reasonable approximation. As this study will demonstrate, this assumption is not correct, which has significant implications on how the mass transfer rate is measured or estimated. A suitable approximation for the mass transfer rate is critical for designing and simulating a small scale PSA process. Hence, a primary goal of

this dissertation is to demonstrate what limits the mass transfer rate in columns of small particles.

Limitations of small scale processes are currently not well understood because a commercial market for these processes has not existed until recently. Large scale processes operate much slower than small scale processes. Furthermore, the size of small scale processes is miniscule compared to industrial units where the production rate is orders of magnitude larger; hence limitations of larger units will not apply to these small units. Maximizing process performance relies on understanding these limitations. One particular challenge highlighted in this study is determining what limits adsorbent utilization. Decreasing cycle time for a PSA process typically results in a gain in adsorbent utilization, often represented in industry by the bed size factor (BSF). Increasing adsorbent utilization results in a lower BSF and smaller overall process size, which is highly attractive for portable systems. Currently, there is no consensus in literature if a lower limit for the BSF exists and what causes it. Furthermore, if a limit does exist, the primary cause of it remains unknown. Hence, the other main goal of this dissertation is to improve the understanding on what limits the size and speed of small scale PSA processes.

This dissertation is organized in the following manner. Chapter 2 provides a broad overview of zeolites, adsorption, and pressure swing adsorption for those readers unfamiliar with these subjects. Chapter 3 provides specific details about the zeolite and equilibrium model used in this dissertation and introduces concepts related to column dynamics that are useful to understand this study. Chapter 4 reviews literature related to small scale PSA and introduces the challenges currently facing the field that are

addressed through this dissertation. Chapter 5 details the methods and materials used in this dissertation for the breakthrough and pressure swing adsorption experiments. Finally, Chapter 6 discusses the results of the study and offers further discussion on what conclusions can be drawn from the data collected.

1.3 Intellectual Contributions

- Experimentally demonstrates the importance of axial dispersion effects for small LiLSX particles for the first time in literature
- Determined axial dispersion effects are the dominant contribution to an overall MTC for Reynolds numbers applicable to breakthrough experiments and most small scale PSA processes.
- Experimentally demonstrates pressure drop does not have a significant effect on small scale PSA performance
- First literature experimental measurement of a minimum BSF for a two column small scale process
- The minimum BSF was proposed to be determined by macropore diffusional resistance

CHAPTER II

BACKGROUND

This chapter introduces the ideas and concepts required to understand the methods and results of this dissertation. In general, adsorption is a separation process that involves the attraction of molecules to an adsorbent surface based on its size or molecular interactions with the solid. This dissertation will focus on a specific adsorbent, LiLSX zeolite, and specific adsorption process, pressure swing adsorption, for the application of oxygen production from air.

2.1 Zeolites

Zeolites are one of many adsorbents used for separation and purification processes. Adsorbents are microporous materials that permit mobility of adsorbate molecules (molecules that adsorb to an adsorbent surface) within the adsorbent and

provide a high surface area to enhance interactions of guest molecules with the solid surface. Adsorbents vary in structure and composition enabling them to interact differently with various types of molecules. Selection of the right type of adsorbent is critical to any adsorption process to achieve the desired separation.

2.1.1 Zeolite History

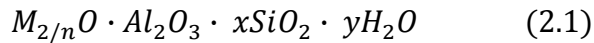
A Swedish man named Baron Cronstedt first depicted zeolites in literature in the 1750's. He proposed the name "zeolite" after heating a natural zeolite and witnessing it bubble and dance as steam released from the zeolite pores.³ Natural occurring zeolites usually contain impurities and an irregular chemical composition that limit their impact scientifically and industrially.⁴ Consequently, zeolites went largely unstudied for close to 200 years as they were viewed as rare minerals without a purification method. In 1905 in Germany, a synthetic zeolite with a larger capacity compared to natural zeolites was manufactured, which permitted the first commercial use of zeolites as a way to soften water.³

Organized research into zeolites did not begin until the late 1930's when Richard Barrer classified zeolites by their pore size. His research at Union Carbide led to the synthesis of the first synthetic zeolites (i.e. zeolites A, X, and Y) for industrial use.^{3, 5, 6} Union Carbide used readily available raw materials along with a lower synthesis pressure and temperature compared to former methods to create these zeolites. The key features of synthetic zeolites compared to the natural version were a larger pore size to accommodate larger molecules, an enhanced pore volume to increase the capacity, and a higher purity of the crystalline phase.⁶ The ability to create a zeolite with a structure and

function tailored to a specific process allowed the industrial potential of zeolites to expand.³ This has produced zeolites today that are crucial to many industrial processes as adsorbents and catalysts.

2.1.2 Zeolite Composition and Structure

Of the approximately 40 naturally occurring zeolites, only chabazite, faujasite, and mordenite are primarily used in industry. Commercially, the most important synthetically created zeolites are Type A, Type X or Y, synthetic mordenite, and all of their ion-exchanged variations.⁷ The composition of a zeolite consists of microporous crystalline aluminosilicates with a chemical formula of the form seen in equation 2.1:



where M is a metal cation of valence n , x is 2.0 or more, and y is the moles of water in the pores. Cavities (or cages) within the zeolite structure are linked to other cavities by pores that allow adsorbate molecules to permeate into the structure. Zeolites differ from other adsorbents through their uniform crystalline structure that provides a well defined pore size for molecules to travel through, while also allowing them to act as effective molecular sieves. IUPAC convention classifies pores by their size as follows:⁸

- 1) Micropores: Less than 2 nm
- 2) Mesopores: Between 2-50 nm
- 3) Macropores: Greater than 50 nm

Micropores, unlike larger mesopores and macropores, are able to trap guest molecules using their solid surface force field. The larger pores serve to assist with diffusion by allowing molecules to travel to the micropores easily. Zeolites have pore sizes less than 2

nm and are therefore completely microporous. The porosity of a zeolite provides a much larger total surface area compared to its external surface, which produces a high adsorption capacity solid where adsorption only occurs in the micropores. Molecular characteristics specific to a zeolite (i.e. pore size, shape, and properties like polarity) control how adsorption and desorption (opposite of adsorption) occur within a zeolite.

The main building blocks of zeolites consist of SiO_2 and Al_3O_2 units that connect tetrahedrally through oxygen atoms. Several of these units form larger secondary units that serve as building blocks for the zeolite structure. These secondary units, shown in Figure 2.1, illustrate silicon and aluminum atoms at the apices with lines representing oxygen bridges between them. More secondary units exist, but the units in Figure 2.1 represent the units used to build the more common zeolite types A, X, and Y. These secondary units are linked in 3-D space to create a porous crystalline structure. For example, shown in Figure 2.2 is a sodalite unit formed from S4R and S6R units (Figure 2.1). Eight sodalite units form the eight-membered oxygen ring of type A zeolites and connect to the final crystal (Figure 2.3) through D4R units (Figure 2.1). Type X and Y zeolites are formed by ten sodalite units connected by D6R units (Figure 2.1) organized in 3-D space to form a twelve-membered oxygen ring as the smallest pore diameter (Figure 2.3). These oxygen rings are responsible for providing entry for adsorbate molecules into the cavity of the zeolite. They determine pore size and what molecules can enter the structure. Since zeolites are 3-dimensional structures, accurately representing them on a 2-D surface is difficult. Figure 2.3 is one of the better illustrations in texts and literature.⁹ By comparison, a single nitrogen molecule is approximately 3.6 Å.

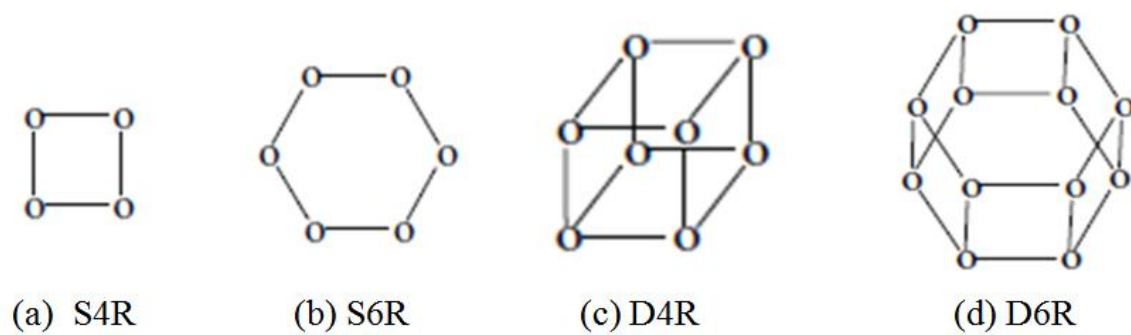


Figure 2.1 Examples of zeolite basic secondary units⁵

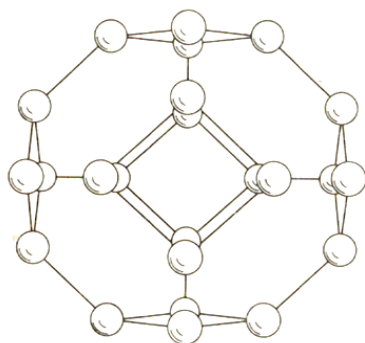


Figure 2.2 Sodalite unit with Si, Al atoms¹⁰

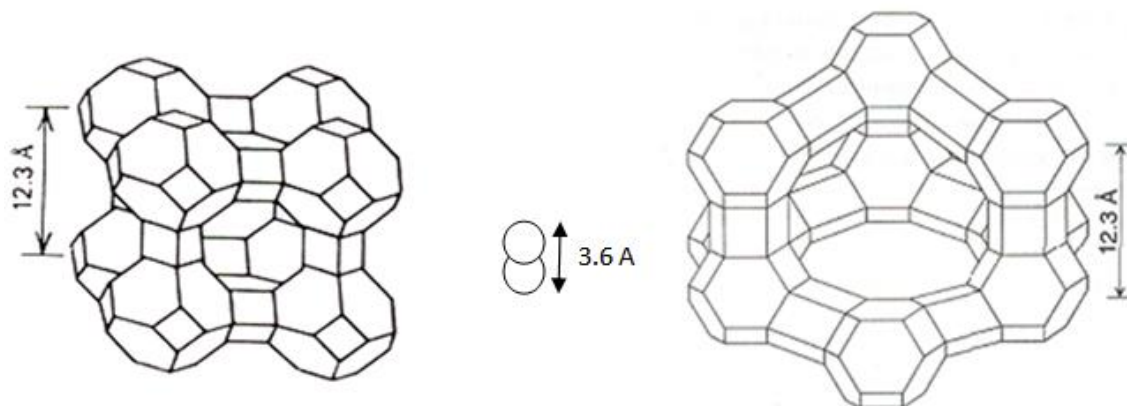


Figure 2.3 Structure of Type A (left), nitrogen molecule (center), and Type X or Y zeolites (right)⁷

The silicon and aluminum atoms within zeolites are interchangeable (although it can be difficult), allowing for a range of Si/Al ratios between one and infinity.⁹ If the ratio is reduced below one, the structure collapses. An aluminum atom induces a net negative charge on the structure, requiring an exchangeable cation to preserve structure electroneutrality. Cations are electrostatically bonded near an Al atom and are therefore not part of the zeolite structure; hence cation exchange is possible. Adjusting the Si/Al ratio and type of exchangeable cation permits zeolite modification for a specific purpose. A higher Si/Al ratio increases the hydrophobic nature of a zeolite, which is useful for removal of organics from water and catalytic applications where water is undesirable. The Si/Al ratio differentiates Type X and Y zeolites. It is between 1 and 1.5 for Type X zeolites, while the ratio is between 1.5 and ∞ for Type Y zeolites. A lower Si/Al ratio increases cation exchange capacity and the ability to adsorb polar molecules. Examples of commonly used exchangeable cations include Na⁺, K⁺, and Ca²⁺.

The exchangeable cation determines the pore size and properties of the zeolite. For example, a Type 4A zeolite utilizes the exchangeable cation Na^+ and all twenty three available sites within a unit cell. For a Type A zeolite, Na^+ cations located on the eight membered ring that serves as the opening into the central cavity will restrict the free diameter of the ring to 3.8 Å (commonly referred to as a 4A zeolite). Forming a 3A zeolite requires substitution of Na^+ with K^+ , which further reduces the free diameter since K^+ is larger than Na^+ . A Ca^{2+} or Mg^{2+} cation substitution creates a relatively unobstructed ring since one bivalent cation replaces two univalent cations. This causes the cation to shift location from the main cavity window to inside the main cavity. The number of cations per unit cell controls the location of the exchangeable cations in the zeolite. A sodalite structure contains Type I, Type II, and Type III active exchangeable ion location sites, each with a different cation capacity. Type I sites are the most readily accessible and fill up first while Type III sites are the most difficult to access and fill up last.

2.1.3 Zeolite Applications

The benefit of zeolites to industry has grown enormously over the last sixty years.⁶ Primary industrial applications include petroleum refining, petrochemical processing, detergent production, and separation and purification processes. Consumer applications include portable oxygen concentrators, stationary refrigerant drying, and air brake dryers for trucks and trains.⁶ Perhaps the largest industrial application is catalysis, which first became important in 1962 with the addition of zeolites as catalysts in a petroleum process called fluid catalytic cracking. Zeolites developed during this time

were significantly more reactive in comparison to their predecessors, which decreased processing costs and substantially increased gasoline production.⁴

Examples of zeolites used in separation and purification processes include: 1) Removal of CO₂, chlorides, and mercury from different process streams in petroleum refining; 2) Drying of hydrocarbon liquids, hydrogen, and cracked gas in petrochemical processes; 3) Drying and desulfurizing natural gas; 4) Removal of water, N₂, and CO₂ from air for cryogenic distillation or PSA processes; 5) Hydrogen purification; and 6) Xylene isomer separation, etc.

Three types of separation are possible with zeolites. First, equilibrium separation occurs if there exists a difference in molecular interactions between the zeolite surface and adsorbate molecules. Equilibrium separation usually hinges on the polarity of the zeolite surface and adsorbate molecules. Another possibility, kinetic separation, exists if there is a difference in the transport rate (i.e. diffusion) of the adsorbate into the internal cavity of the zeolite. This requires the adsorbent micropore size to be similar to that of the adsorbate molecules undergoing separation. Finally, molecular sieving occurs if the size of a zeolite pore is too small for one molecule but not another in a fluid mixture. Air separation, the topic of this dissertation, involves equilibrium separation where the zeolite preferentially adsorbs nitrogen allowing for production of nearly pure oxygen at feed pressure. 5A and 13X zeolites are commonly used to accomplish this separation in a PSA process.

2.2 Adsorption

Adsorption by definition is the accumulation of fluid molecules at a surface. This phenomenon occurs because of an attraction between adsorbate molecules (either a gas or liquid) and an adsorbent surface (porous solid).⁷ There are two adsorption mechanisms, physical adsorption and chemisorption. Physical adsorption is of interest because it is easily reversible and can form more than one molecular layer. Chemisorption involves the formation of bonds between the adsorbate molecule and adsorbent surface. However, it can only form one molecular layer on a solid surface and it is not easily reversible, which limits its industrial impact for separation and purification processes. Air separation occurs via physical adsorption, hence all references to adsorption from this point forward in this dissertation refer to physical adsorption only.

2.2.1 *Adsorption Fundamentals*

The attraction between an adsorbent and adsorbate molecules results from molecular interactions, which are a combination of permanent dipoles, induced dipoles, and London dispersion forces. Permanent dipoles occur in polar molecules as a result of an uneven distribution of charge in the electron cloud. Polar molecules can also induce an uneven charge distribution (i.e. polarity) in nonpolar molecules if they are close enough to interact. Nonpolar molecules do not have permanent dipoles when their charge is averaged over time. However, at any instantaneous moment they will have a dipole that has potential to induce a dipole on another nonpolar molecule, creating London Dispersion forces. Repulsion forces occur when molecules are too close to each other and their electron clouds overlap. When adsorption occurs, equilibrium exists between

repulsive and attractive forces. Figure 2.4 shows potential energy (sum of all the interactions that exist between the adsorbate and adsorbent) as a function of the distance of the adsorbate molecule from the adsorbent surface. The high positive repulsive potential energy near the adsorbent surface is where the electron cloud overlap would occur. The potential well depth, $U(r_0)$, is related to the interaction strength between the adsorbate and solid surface. The larger the potential energy difference, the greater the attraction. At zero Kelvin (no kinetic energy), a molecule would settle at the bottom of the well. At all other finite temperatures, the molecule oscillates around the minimum potential energy.

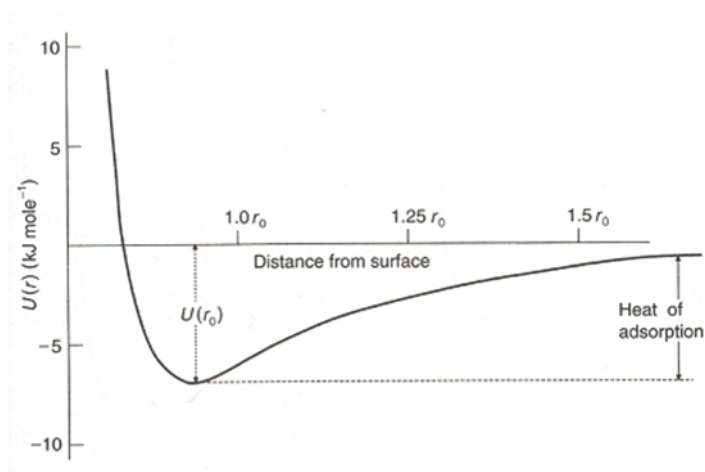


Figure 2.4 Potential energy diagram for adsorption⁷

2.2.2 Adsorption Thermodynamics

Adsorption equilibrium determines how much of a fluid molecule is trapped in an adsorbent at a defined pressure, temperature, and composition. Adsorption causes a gas molecule to lose at least one of its translational degrees of freedom because it restricts the gas molecule to move along the adsorbent surface. This causes a decrease in entropy (ΔS) and since adsorption is a spontaneous process, Gibbs free energy (ΔG) is reduced as well. According to the thermodynamic expression in equation 2.2, ΔH (enthalpy) also must decrease (heat is released), making adsorption an exothermic process.

$$\Delta G = \Delta H - T\Delta S \quad (2.2)$$

Isotherms are a typical method of representing equilibrium for single component adsorption. Isotherms are measured at a constant temperature while the pressure is varied and the amount of adsorbate is measured. They form different shapes as shown in Figure 2.5. Type I isotherms are most relevant to this study and represent adsorbents that have pores similar in size to the adsorbate molecules and fill up as a saturation limit is approached. The other types of isotherms have larger pores compared to the adsorbate and hence do not experience this saturation limit, except for type IV and V isotherms near P_s . Type III isotherms represent systems where an adsorbate interacts more strongly with other adsorbates than with the adsorbent. Type II isotherms can have multiple adsorbed layers because of their larger pore size distribution and represents the other type of isotherm sometimes used in a PSA process.

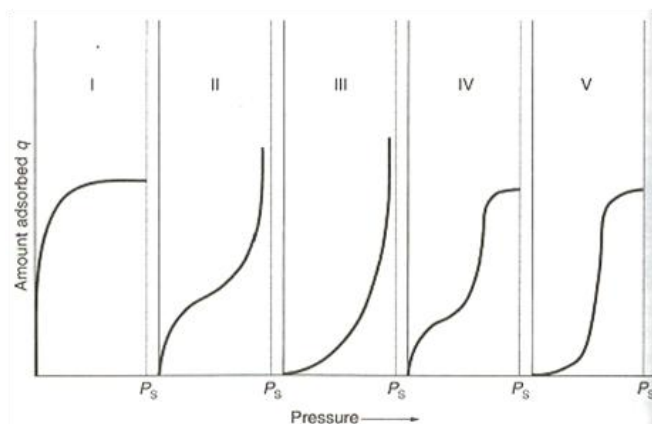


Figure 2.5 The five types of isotherms⁷

2.2.3 Diffusion in Microporous Adsorbents

Diffusional resistances affect the approach to equilibrium in an adsorption process. There are three resistances to mass transfer related to an adsorbent particle. The first occurs around adsorbent particles as film resistance if the fluid is a mixture, due to accumulation of the less adsorbed component on the surface. The other two occur within the particle in the macro/mesopores between the crystals and in the micropores within the crystals themselves. These resistances are in series, but typically only one is rate controlling. Zeolites are also often synthesized with a porous binder material that holds the crystals together, especially for separation processes where a sudden change in pressure occurs. An example of a zeolite particle structure is represented in Figure 2.6.

Macropore diffusion occurs in adsorbent pores significantly larger than the diameter of the diffusing sorbate. In zeolite particles, these exist between microporous crystals. When pore size is much greater than the mean free path of the sorbate molecules, diffusion occurs by bulk gas diffusion. At low pressures and with smaller

pores, collisions between the diffusing molecule and pore wall become important resulting in Knudsen diffusion. Furthermore, Poiseuille flow (pressure driven flow inside a particle) becomes relevant with larger pore and particle sizes and at higher pressures, such as the pressurization step of a PSA process. Under high adsorbate concentrations and if the adsorbed phase is mobile, adsorbed molecules may diffuse on the pore surface as well.⁸

Micropore diffusion occurs in pores of comparable size to the adsorbate molecules. For a zeolite particle, this occurs within the crystals where pore size into the cavity of the zeolite is limited by the oxygen windows. If a binder is present, micropore diffusion will occur through the binder as well. The “adsorbed phase” in this type of diffusion refers to the combination of molecules adsorbed on the pore wall and trapped in the middle of the pore.⁸ Micropore diffusion is an activated process because unlike macropore diffusion, it is not possible for the adsorbate molecules to escape the forces of the pore wall; hence temperature strongly influences micropore diffusion. The type and distribution of the exchangeable cation will affect adsorbate diffusivity into the micropores, along with how strongly the adsorbate molecules are attracted on to the surface.

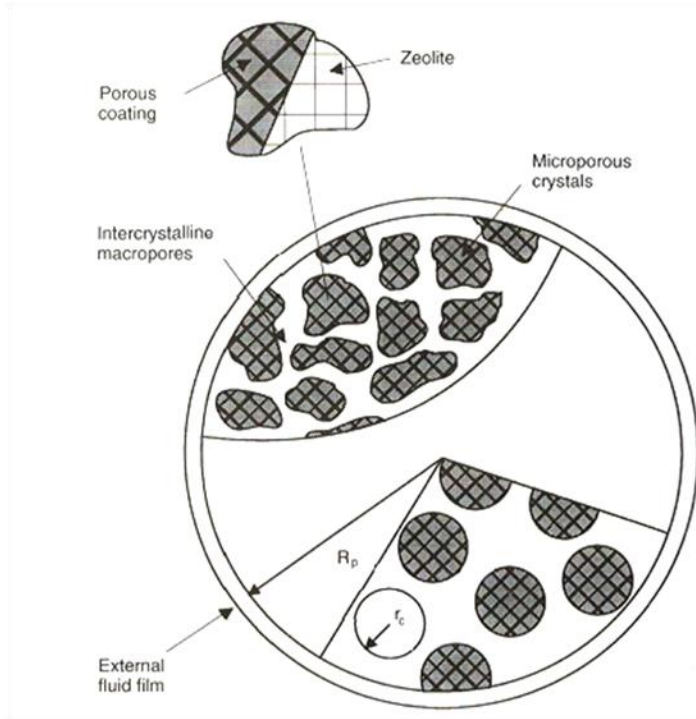


Figure 2.6 Depiction of pores and mass transfer resistances in an adsorbent particle⁷

2.3 Air Separation by Pressure Swing Adsorption

Pressure swing adsorption (PSA) is a process designed for efficient gas separation and purification by utilizing the ability of molecules to adsorb on the surface of an adsorbent. This study focuses only on equilibrium separation for oxygen production. Air separation utilizing equilibrium separation is feasible because nitrogen is selectively adsorbed over oxygen by X-type zeolites.

2.3.1 *PSA Principles*

The basic premise of a PSA process involves one or more columns packed with an adsorbent (zeolite, carbon molecular sieve, etc.) that preferentially adsorbs one type of gas molecule over another. This normally occurs at some pressure above atmospheric pressure until the gas nearly saturates the column with the more strongly adsorbed gas molecule (heavy component). The “raffinate” product is the gas molecule type that adsorbs less (light component) and exits the product end of the column. Once a column is nearly saturated with the heavy component, it needs to be removed through regeneration (desorption) in order to reuse the column later in the process. Desorption is critical to process efficiency. As previously mentioned, adsorption equilibrium is determined by the gas composition, temperature, and pressure. A change in any of these properties can be used to regenerate the adsorbent in the column. Since desorption is the opposite of adsorption, the process is endothermic in nature. Desorption in a PSA process occurs through a change in column pressure and composition as they provide quicker methods of regeneration compared to a change in temperature. Desorption occurs at either atmospheric or vacuum pressure causing the pressure to swing from high

pressure during adsorption to a low pressure during desorption, hence the name “Pressure Swing”.

While most separation processes operate under steady state, a PSA process is dynamic as conditions within the column are constantly changing at every location. The process operates as cycles in which a column repeatedly experiences a series of pressurization, adsorption, and regeneration steps. PSA processes ideally operate under cyclic steady state (CSS), which occurs when column conditions at the end of each step do not change from cycle to cycle. At CSS, the cycle performance remains the same over time.

PSA performance is typically evaluated based on product purity, recovery, and productivity. Adsorbent selectivity primarily determines the possible product purity. Selectivity, s , of a zeolite (or any adsorbent) is the degree to which a zeolite can adsorb one type of molecule over another. It is numerically described as:

$$s = \frac{x_i/y_i}{x_j/y_j} \quad (2.3)$$

where x_i and y_i represent the mole fractions of component i in the adsorbed and fluid phases respectively. Selectivity depends on the temperature, pressure, type of zeolite used and the molecules undergoing separation.

Product recovery measures the amount of desired component in the high pressure product stream compared to that in the feed stream. Purity and recovery indirectly measure separation efficiency and determine if a process design is capable of producing the desired results.¹¹ There is a trade-off between recovery and purity; i.e. high purity

usually results in lower recovery. Maximum potential recovery is established by the affinity of the solid for the heavy component over the light component through equilibrium. Recovery determines the energy efficiency of the process since it determines how much high pressure feed is utilized per product rate.

Productivity is a measure of adsorbent utilization and is related to the speed and size of a process. The mass transfer rate in the column primarily determines the size, cycle time, and amount of adsorbent, all of which impact the process productivity. All of these performance parameters are mutually dependent on each other and changing one will impact the others.

2.3.2 History and Growth of PSA

Pressure swing adsorption is a technology that has developed primarily within the last 50 years. It has become a valuable part of processes such as air drying, hydrogen purification, n-paraffin removal, xylene isomer separations, and air separation.⁹ Several important factors make PSA more feasible compared to other separation techniques. First, an extra thermodynamic degree of freedom to define the adsorption process provides greater design flexibility compared to processes like distillation, extraction, and absorption. Second, the large number of adsorbents including zeolites, activated carbons, silica gels etc., with different properties allow for various separations. Finally, optimizing a process for a specific adsorbent or end product allows for creativity, engineering, and continuous growth in PSA technology.¹² For example, there are numerous ways to design and operate an air separation process to achieve essentially equivalent results. Improvement of PSA processes occur through either developing new

adsorbents (material science) or developing more efficient steps in the cycle (engineering).¹¹

PSA processes were originally researched for air separation in the 1950's and 1960's.⁹ Production of ultrapure oxygen through cryogenic distillation is economically feasible only in large scale applications because of the extremely low temperature (96 K) required. However, for smaller scale operations or when a high purity is not required, PSA processes are more economical than cryogenic distillation. The low adsorption selectivity of early solids rendered air separation before the 1950's challenging. However, with the development of synthetic zeolites (i.e. 5A, 13X), air separation was thrust into the forefront of adsorption research.⁹ This led to the development of two different types of PSA cycles in the late 1950's that served as the basis for later designs of PSA systems. The first patent was for the Skarstrom cycle assigned to Esso Research and Engineering Company.¹³ The other was for the Guerin-Domine cycle assigned to L'Air Liquide.¹⁴ The regeneration method is the main difference between the cycles.⁸

Figure 2.7 illustrates an example of a traditional two column Skarstrom cycle, which is the base cycle used in this study. A cycle consists of both columns experiencing the following steps: 1) pressurization, 2) production, 3) countercurrent (opposite of feed flow) blowdown, 4) countercurrent purge. The pressurization and production steps are

similar in that they both involve the input of feed gas and hence are referenced in the future as a combined “feed” step where the flow direction is defined as the same as the feed flow. The cycle works such that one column undergoes the feed step while the other is counter-currently blowing down and purging. The purge step involves passing a fraction of the purified light product through the column at low pressure after the blowdown step. Figure 2.8 illustrates the pressure variation in the column during each step. Skarstrom cycles usually operate their feed step at a pressure above atmospheric pressure while the blowdown and purge steps occur at pressure slightly above atmospheric to prevent a vacuum pump. Regeneration in a Skarstrom cycle occurs primarily by lowering the column partial pressure of nitrogen. The blowdown step accomplishes this by dropping the overall pressure to atmospheric pressure. The exit stream from the blowdown step is primarily composed of the heavy component concentration or “extract”. The purge step further lowers the nitrogen partial pressure by countercurrently flowing part of the purified oxygen product through the column. The purge step is perhaps the most important step because it pushes back the heavy component concentration front towards the feed side of the column, preventing negative effects on product purity in the next cycle. Product purity rises when the purge amount increases, but only to a maximum purity of 96%. Raising the purge amount also has an obvious negative impact of reducing recovery since it reduces the amount of product left available. At a higher column operating pressure, the portion of the product gas required for the purge step reduces because of the volume increase going from higher to lower pressure.

However, higher pressure creates a greater energy requirement and eventually, any extra adsorption that occurs does not outweigh the energy costs of the higher column pressure. Also, higher column pressure increases the amount of raffinate product lost during the blowdown step, which eventually limits recovery at high pressures.⁸ Part of designing a PSA system deals with finding the optimum pressure ratio (ratio of adsorption pressure to desorption pressure) and critical purge. Critical purge occurs when just enough purge gas is taken from the product to achieve a specified product purity. This is useful information to determine the optimal operating conditions of the process. Finding the optimal purge amount that provides the necessary purity and highest possible recovery is a major challenge when engineering a PSA process.

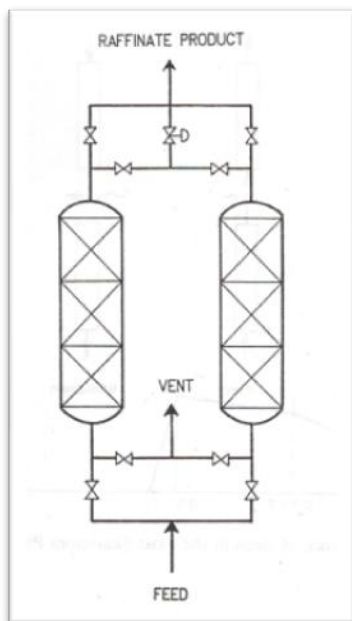


Figure 2.7 Basic two-column pressure swing adsorption system⁸

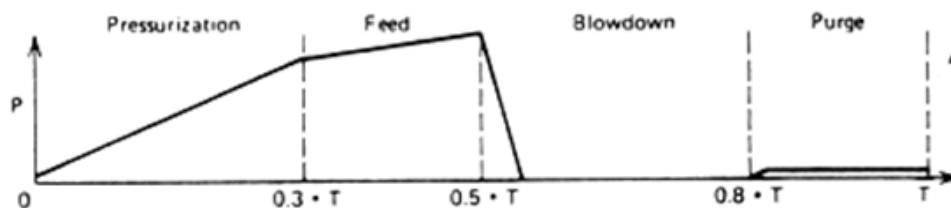


Figure 2.8 Column pressure during Skarstrom cycle⁸

2.3.3 Improvements to PSA Cycles

The Skarstrom process is effective for air drying, but air separation only produced 90% oxygen at a recovery of 10% with a 13X zeolite adsorbent.⁸ Enhancements to the cycle were clearly necessary in order for it to become economical for air separation. Several key improvements to the original Skarstrom cycle have allowed it to become a viable option for smaller scale air separation operations. These improvements aim to increase recovery, lower energy requirements, and reduce process size. They include adding additional steps to the original 4-step cycle, operating at lower than atmospheric pressure, and cycling faster.

One method of improving recovery uses product gas to pressurize a column after the purge step. Often called product pressurization, this increases product purity because the product gas helps keep the product end clean of the heavy component by pushing back the heavy component front further towards the column feed side. A nearly full pressurization with product gas requires a large tank, hence a full product pressurization is not always desirable. However, a partial pressurization is still advantageous to

improve recovery while maintaining a high purity. The product gas used for partial pressurization reduces the purge gas requirement and is mostly recovered during the feed step.

Another important improvement is the addition of a pressure equalization step, first suggested in a patent filed in 1964 by Marsh.¹⁵ The concept is intended to conserve what is normally waste gas during the blowdown step, and use it to partially pressurize another column before the feed step. Instead of an immediate blowdown step after the end of the feed step, two columns are connected and pressure equalizes between the two columns. This saves energy because the column that is partially pressurized now needs less feed gas achieve the desired adsorption pressure. If raffinate is the desired product, then the product side of the columns are connected so any leftover raffinate product from the depressurizing column travels to the pressurizing column. This conserves separative work during the following feed step, which increases recovery.¹¹ For large capacity operations, using pressure equalization with more than two columns further improves the recovery and allows for a more continuous product stream flow without requiring an extra storage tank.^{8, 11}

Another possible improvement to the Skarstrom cycle is blowing down the column to vacuum instead of atmospheric pressure. If the high pressure step is atmospheric, the process is called vacuum swing adsorption (VSA). When adsorption pressure is above atmospheric, then it is considered a hybrid PVSA process. Under vacuum, less purge flow is required to regenerate the adsorbent. The extra energy requirement to attain vacuum is offset to some extent by a lower adsorption pressure requirement in the column, which makes VSA and PVSA economical in some

applications. Vacuum operation in air separation usually lies in the Henry's law region of the isotherm where pressure ratio determines the possible purity and recovery.⁸ Under vacuum, adsorbent selectivity is always higher which improves recovery of the raffinate product and up to 30% in energy savings.⁷

By definition, there are three ways to increase PSA process productivity. First, employing an adsorbent with an increased capacity allows for either increased production of raffinate or a reduction in the amount of sorbent needed in the column, both of which will increase productivity.¹¹ Another method is cycle time reduction. Typical industrial PSA processes have a cycle time as long as 10 minutes. When the cycle time is lowered to 30 seconds or below, it is often referred to as rapid PSA (RPSA).

2.3.4 Air Separation Applications

The largest application of air separation is the production of 90-94% pure oxygen gas for use in industrial processes and medical applications. The advancements discussed earlier produced improved PSA/VSA units in the mid-1980's and 1990's that used five times less adsorbent and two times less power.⁶ A simple two-column VSA system was able to produce over 100 tons of oxygen per day, which provided an alternative to cryogenic air separation. Compared to cryogenic systems with similar production, the VSA system had a higher capital cost, but allowed for a significant energy savings.⁶

A significant application for air separation through small scale PSA is personal oxygen concentrators (POC) for oxygen therapy. These oxygen concentrators utilize rapid cycling to significantly reduce the device weight to less than 4.5 kilograms and provide up to 6 liters per minute of oxygen. Originally POC's were designed for use in

ambulances and short term travel. Currently they are found in nursing homes and for everyday use in place of oxygen cylinders. Numerous companies have entered POC market including Inogen One, Invacare, AirSep, and Respirationics. POCs all have a similar design because they all operate on the same engineering and design fundamentals. The difference in performance comes from trade-offs made in the design process to provide different specifications and characteristics that reduce the energy requirement and target specific patient needs.¹⁶

2.3.5 Future Challenges for PSA

Modeling of a PSA process remains difficult because the complex and dynamic nature of a PSA process; hence the design and optimization of the process remains principally experimental in nature. Modeling the process requires numerous partial differential equations describing the number of different process steps, initial conditions, and boundary conditions for each step. Solving these equations is both time consuming and difficult to do with the accuracy and reliability.¹² Further adding to the problem is the difficulty in understanding multi-component gas-solid interactions that are needed for solving the equations in the model. Predicting these interactions from limited experimental data is difficult because of the range of conditions (pressure, temperature, and composition) that occur within PSA system throughout the process. Currently the best solution is developing simplified models for predicting a PSA process and then improving the process through a pilot plant.¹² Improving the knowledge of multi-component adsorption will remain the focus of research for years to come because of the challenges it provides. While air separation is a fairly established PSA process, utilizing the technology for other applications is another challenge for researchers. Current work

is directed at improving PSA process for CO₂ capture from flue gases, olefin-paraffin separation, and CH₄-CO₂ separation.⁷

CHAPTER III

THEORY

This section introduces the theory and concepts behind gas adsorption on a surface through a brief discussion of intermolecular forces. Using these concepts, the interaction of oxygen and nitrogen molecules with zeolites is then explained with consideration for how different exchangeable cations affect selectivity. Finally, isotherm models are reviewed along with the column dynamics that occur within a PSA process.

3.1 Intermolecular Forces

Intermolecular forces were briefly discussed in the previous section. However, a more rigorous description of these forces is required to understand zeolite selectivity. In a PSA process for air separation, interaction of oxygen and nitrogen molecules with a zeolite is dependent on electrostatic, induction, and dispersion forces. These forces are reviewed to the extent necessary to understand air separation. Additional resources are available that specifically discuss intermolecular forces in greater detail.^{17, 18}

3.1.1 *Electrostatic Forces*

An electrostatic force is a broad term encompassing several types of intermolecular forces. Coulomb's law illustrates the simplest type where two ions approximated as point charges have a force, f , between them, defined as:

$$f = \frac{w_i w_j}{4\pi\epsilon_0 h^2} \quad (3.1)$$

where w is the magnitude of the point charges, h is the distance between the point charges, and ϵ_0 is the dielectric permittivity. Integration of equation 3.1 gives the potential energy, E , between the two ions as:

$$E_{ij} = \frac{g_i g_j e^2}{4\pi\epsilon_0 h} \quad (3.2)$$

where g_i and g_j are ionic valences of the two point charges and e is the electron charge. Potential energy between the ions is inversely related to the distance between the ions. When the ions are not approximated as point charges, their charge is shielded by ionic electron clouds, which causes potential energy to vary inversely with distance (between the ions) to a power greater than one.¹⁸

Electrostatic forces are not solely between ions, interactions between molecules with dipole and quadrupole moments are also included in these forces. Polar molecules exhibit dipole moments because their asymmetrical shape creates an unbalanced distribution of electrons around the molecule, resulting in a separation of effective charge between any two locations in the molecule. Non-polar molecules have a symmetrical geometry, which does not produce an effective charge distribution resulting in a dipole

moment. Molecules may also exhibit higher order charge distribution. For example, a quadrupole signifies an effective charge difference at four points in the molecule and an octupole signifies an effective charge difference at eight points in the molecule.¹⁷ For oxygen generation via air separation, the difference between quadrupoles of N₂ and O₂ is exploited (see Table 3.1).

3.1.2 Induction and Dispersion Forces

Intermolecular interactions also take the form of induction forces when electrons of a molecule become disturbed in an electrical field. The molecule (polar or non-polar) essentially gains an instantaneous charge distribution from the electrical field of another polar (or quadrupolar) molecule or ion in the immediate vicinity; hence the name “induced” electrostatic interaction. This causes the molecules to experience an attractive force with polar (or quadrupolar) molecules or ions. The ease with which electrons are dislocated in a molecule is called polarizability, α , of the molecule. Accordingly, induced electrostatic interactions are a strong function of polarizability.¹⁷

Finally, intermolecular interactions also occur due to instantaneous coupling of electron clouds of two molecules approaching each other. This type of interaction, called a dispersion force, exists for all molecules in nature, even if the molecules are non-polar since the effective charge distribution for a non-polar molecule is only zero when averaged over time. At any given instant, the molecule (polar or nonpolar) has a momentary dipole moment capable of inducing an effective charge distribution on a neighboring molecule. Hence, electrons in the interacting molecules essentially move in tandem resulting in a net attractive (negative) potential energy. The ionization potential

and polarizability of the involved molecules determine the level of interaction.¹⁸ Dispersion forces, together with dipole-dipole (and higher order charge distributions), and induction forces are collectively called van der Waals forces.

3.1.3 *N₂ and O₂ Interaction with Zeolites*

A simple way to view the interaction of oxygen and nitrogen molecules with zeolites is to treat the exchangeable cations of zeolites as point charges.¹⁹ With this model, the important intermolecular forces are due to interaction of the oxygen or nitrogen quadrupole moment with the point charge and the always present dispersion energy. When the point charge and one of the molecules are arranged linearly (most energetically stable orientation), interaction due to the quadrupole moment depends on $1/h^3$, while the interaction energy due to the induced dipole depends on $1/h^4$. Hence, quadrupole interaction energy is effective further away from the point charge compared to the induced dipole interaction energy. Table 3.1 shows a significant difference between the quadrupole moment of a nitrogen and oxygen molecule, while their polarizability is nearly identical. A similar polarizability indicates nitrogen and oxygen have similar induction and dispersion forces with the point charge. Therefore, a zeolite attracts nitrogen over oxygen largely because of the quadrupole moment disparity between them. Beyond this simple demonstration, additional factors also affect zeolite selectivity including the relative position of the cations in the zeolite, orientation of the nitrogen and oxygen molecules relative to the exchangeable cation, and the zeolite structure.¹⁹ Figure 3.1 illustrates the difference in potential energy between the two molecules as they approach the point charge (y-axis).

Table 3.1 Quadrupole moment and polarizabilities of nitrogen and oxygen molecules^{17, 18}

Molecule	$M \times 10^{40} \text{ (C-m}^2\text{)}$	$\alpha \times 10^{25} \text{ (cm}^3\text{)}$
O ₂	-1.3	16.0
N ₂	-5.0	17.7

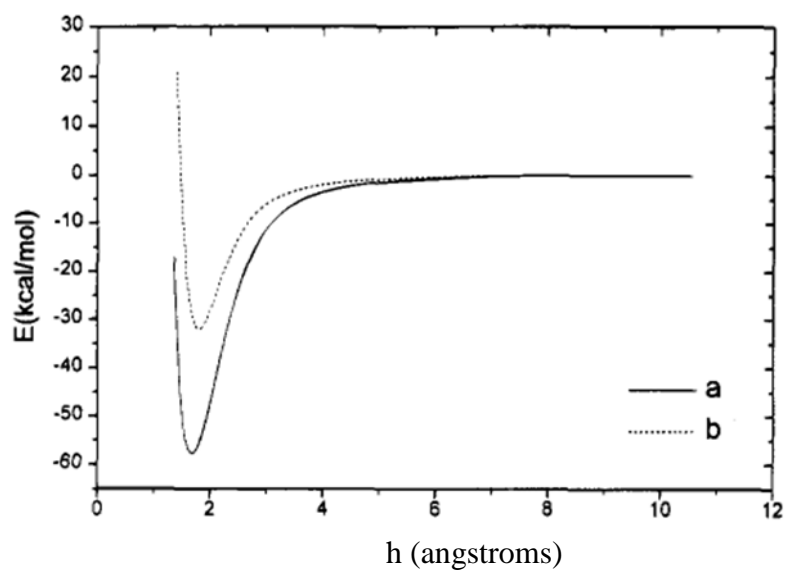


Figure 3.1 Calculated potential energy curves of N₂ (a) and O₂ (b) in the linear arrangement as a function of distance, h , between the point charge and midpoint of the diatomic molecules¹⁹

3.1.4 Exchangeable Cations

The type of exchangeable cations in a zeolite significantly impacts its selectivity for nitrogen. Papai et al.¹⁹ studied how different exchangeable cations affect zeolite selectivity. Their conclusion was that substituting Li^+ for Na^+ increases the binding energy for nitrogen molecules more than it does for oxygen molecules, which increases selectivity for nitrogen. Figure 3.2 compares the potential energy curve of Li^+N_2 with that of Na^+N_2 . The potential energy difference is explained by the lack of core electrons for Li^+ . The core electrons of Na^+ provide a lower charge density than Li^+ , which also has a smaller ionic radius. The higher charge density of Li^+ enhances interaction with nitrogen molecules. A smaller ionic radius also enhances the attraction due to short range interaction forces. The smaller cation increases potential well depth and decreases separation between the ion and nitrogen molecule (i.e. collision diameter). Figure 3.2 compares the location of the minimum potential for Li^+N_2 to the minimum potential of Na^+N_2 .

Use of Li^+ ions in zeolites was studied as early as 1964 by Mckee.²⁰ Chao further explored the extent of Li^+ cation exchange necessary for effective nitrogen adsorption.²¹ His invention showed a greater Li^+ ion exchange, preferably around 90%, increased zeolite capacity and selectivity for nitrogen. He further noted that a Si/Al ratio near 1.0 significantly increased adsorption capacity and selectivity.

Ion exchange using Li^+ does have some limitations. Highly Li^+ exchanged zeolites are expensive to produce since ion exchange with Li^+ is less thermodynamically favorable than with Na^+ or Ca^{2+} . However, the cost of producing highly exchanged Li-X

zeolites has recently been reduced and they are now considered the state of the art material for oxygen generation via air separation for large and small scale processes.

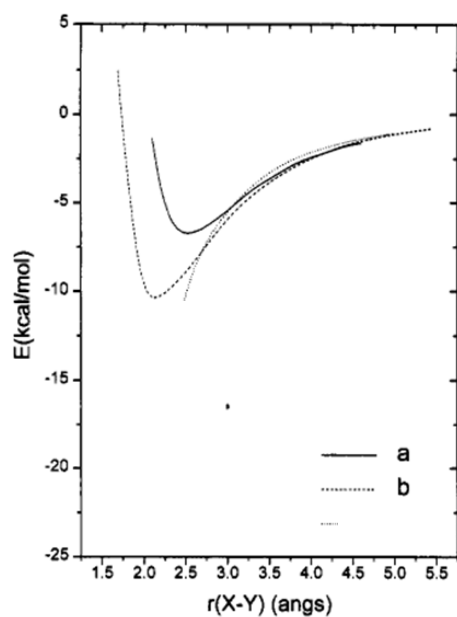


Figure 3.2 Potential energy curves of Na^+N_2 (a) and Li^+N_2 (b).¹⁹ $r(X-Y)$ is the distance between the center of the positive ion and the closer end of the N_2 molecule

3.2 Adsorption Equilibrium Modeling

Adsorption equilibrium models are highly important not only for PSA processes, but other applications as well. Collection of equilibrium data is tedious and time consuming; hence an accurate model avoids the need for excessive lab work. Numerous models for both single and multi-component adsorption currently exist in literature. Equilibrium modeling has been well studied and written about in numerous texts, specifically ones by Crittenden & Thomas, Ruthven et al., Suzuki, and Yang.⁷⁻¹⁰ This section provides a brief summary of equilibrium models relevant to this study starting with the most basic and then increasing in complexity.

3.2.1 *Henry's Law*

Equilibrium between a solid adsorbent and adsorbate molecules is determined from thermodynamics. The adsorbed layer(s) is considered a separate phase in a thermodynamic sense. At low adsorbate concentrations, the equilibrium relationship closely resembles a linear function, which is defined as Henry's Law:

$$n^* = K_H p \quad (3.3)$$

where n^* is the equilibrium amount adsorbed of component, K_H is the "Henry's Law" constant, and p is the partial pressure of adsorbate in the gas phase. An Arrhenius relationship is used for the temperature dependence of the Henry's law constant.

$$K_H = K_0 e^{-\Delta Q/RT} \quad (3.4)$$

In equation 3.4, ΔQ is the heat of adsorption, R is the ideal gas constant, K_0 is related to adsorption entropy change, and T is temperature. At low pressure as density approaches

zero, all adsorption systems must thermodynamically approach Henry's law with a finite slope at the origin. It is exact as pressure approaches zero and thermodynamically describes the slope at the origin.

3.2.2 *The Langmuir Isotherm*

The simplest and most commonly used adsorption model for microporous solids that includes a saturation capacity with a finite number of sites (each site can only accommodate one molecule) is the Langmuir isotherm. The Langmuir model assumes monolayer surface coverage of the adsorbate on the adsorbent surface.²² It also assumes the surface is energetically uniform and adsorbed molecules are isolated with no interaction forces between them. The Langmuir model has wide use for describing dynamic equilibrium of physical adsorption systems at low surface concentrations. Many systems show at least relative consistency with the Langmuir model. Furthermore, it reduces to Henry's Law at low concentrations, which is a requirement for thermodynamic consistency in any physical adsorption system. This allows it to at least serve as a starting point for design of PSA systems.⁸ Key assumptions of the Langmuir isotherm are as follows:

- 1) The heat of adsorption is constant and independent of coverage (due to assumption of isolated adsorbed molecules with no lateral interactions)
- 2) Only one adsorbate molecule is located at a site
- 3) Localized adsorption (adsorbed molecules remain adsorbed until desorption occurs)
- 4) The solid possesses finite number of adsorption sites

Langmuir contended the rate of adsorbate gas molecules colliding with the adsorbent surface is proportional to the partial pressure of the gas, and the probability of adsorption occurring is proportional to the fraction of empty sites. Additionally, he asserted the desorption rate is directly proportional to the fraction of occupied sites. Finally, he contended that at dynamic equilibrium, the rates of adsorption and desorption are equal.⁷ For a single adsorbate system, the rate equation is represented as:

$$k_a p_i (1 - \theta) = k_d \theta \quad (3.5)$$

where p_i is the adsorbate gas pressure, θ is the fractional surface coverage, and k_a and k_d are rate constants for adsorption and desorption respectively. θ is the ratio n^*/n_s where n_s is the adsorption saturation capacity assuming only monolayer coverage. When k_a and k_d are combined together (since they cannot be experimentally determined individually), the Langmuir isotherm equation is represented as:

$$\theta = \frac{bp}{1 + bp} \quad (3.6)$$

where b is the ratio k_a/k_d (adsorption equilibrium constant). Equation 3.6 correctly approximates the asymptotic behavior that appears as sites fill up during adsorption for microporous systems. The adsorption equilibrium constant, b , is often found experimentally, and is directly related to the Henry's constant ($K_H = bn_s$). Both b and K_H decrease as temperature increases because adsorption is exothermic. Hence, isotherms at lower temperatures possess more curvature and appear higher than those at higher temperatures.

3.2.3 Dual Site Langmuir Model

An extension of Langmuir is the “dual-site Langmuir (DSL)” model, which accounts for an additional adsorption site not present in the Langmuir model.²³ With two adsorption “sites”, the DSL model has greater mathematical flexibility and can represent almost any pure component data. It represents zeolitic systems very well because the two sites capture the essence of the two types of interactions with the surface. One site represents the electrostatic interaction with exchangeable cations, while the other site represents the much smaller difference in the attraction of nitrogen and oxygen molecules to the zeolite structure due to dispersion forces. In essence, it is rationalized there is one site representing the electrostatic and induced electrostatic interactions with the exchangeable cations, and another site representing dispersion interactions with the zeolite structure. The DSL model for a pure component gas is expressed as:

$$n^* = \frac{n_s^b b P}{1 + b P} + \frac{n_s^d d P}{1 + d P} \quad (3.7)$$

where n_s^b and b are the saturation capacity and equilibrium constant respectively for the exchangeable ion sites while n_s^d and d are the same parameters due to the dispersion interaction effect. It is assumed b is greater than d because exchangeable ions have higher affinity for adsorbate molecules than the neutral zeolite structure. If the saturation capacity of each gas molecule is assumed equal for each site, the DSL multicomponent model is represented as:

$$n_i^* = \frac{n_s^b b_i P y_i}{1 + \sum_j b_j P y_j} + \frac{n_s^d d_i P y_i}{1 + \sum_j d_j P y_j} \quad (3.8)$$

The equilibrium constants assume the usual Arrhenius temperature dependencies:

$$b_i = b_i^0 e^{Q_i^{(b)}/RT} \quad (3.9)$$

$$d_i = d_i^0 e^{Q_i^{(d)}/RT} \quad (3.10)$$

where b_i^0 and d_i^0 are the two pre-exponential constants for gas i , and $Q_i^{(b)}$ and $Q_i^{(d)}$ are the heat of adsorption of gas i on the two sites (or vertical interaction energy). Mathias et al. have demonstrated the accuracy of the DSL model for nitrogen/oxygen mixtures and zeolite 5A.²³ LiLSX is similar enough to zeolite 5A to justify using DSL to describe binary equilibrium for this dissertation.

3.3 Adsorption Column Dynamics

The ultimate separation efficiency is determined by adsorption equilibrium, which takes infinite time to achieve. Yet processes operate within a finite time frame. Adsorption kinetics determines the approach to equilibrium at any location in a column at a given time. This section reviews how adsorption kinetics affects column dynamics. An abundance of literature exists that provides far greater detail on this subject, specifically ones written by, Yang, Motoyuki, and Ruthven.^{9, 10, 24}

3.3.1 Adsorption Rate

An axially dispersed plug flow model is used in PSA modeling as the material balance for each component in a packed adsorption column.

$$D_L \frac{\partial^2 c_i}{\partial z^2} + \frac{\partial}{\partial z}(u c_i) + \frac{\partial c_i}{\partial t} + \left(\frac{\rho_b}{\varepsilon_b}\right) \frac{\partial n_i}{\partial t} = 0 \quad (3.11)$$

The four terms in the model describe the following phenomena in order: 1) axial dispersion 2) convective flow 3) gas phase accumulation 4) adsorption rate (i.e. solid phase accumulation). The adsorption rate is often described using a linear driving force (LDF) model expressed as:²⁵

$$\frac{\partial n_i}{\partial t} = k_i(n_i^* - n_i) \quad (3.12)$$

where n_i^* is the equilibrium value of component i in the adsorbed phase at a given fluid phase concentration, and n_i is the adsorbed phase concentration of component i , both averaged over an adsorbent particle. The mass transfer coefficient (MTC), k_i , of a spherical particle is typically approximated as:²⁴

$$\frac{1}{k_i} = \frac{Kr_p}{3k_f} + \frac{Kr_p^2}{15\varepsilon_p D_{pi}} + \frac{r_c^2}{15D_{ci}} \quad (3.13)$$

where k_f is the film transfer coefficient, r_p and r_c are the particle and crystal radius respectively, D_p and D_c are the macropore and micropore diffusivity of component i respectively, ε_p is the particle macroporosity, and K is the dimensionless equilibrium constant related to the Henry constant, K_H , by $K = K_H RT \rho_p$. The three terms on the right side of the equation account for resistance to mass transfer in the film, macropore and micropore respectively. Equation 3.13 is defined from a flux equivalency through the three resistances in series and is exact for linear isotherms in the Henry's law region. While only strictly applicable to linear isotherms, it is a useful approximation for non-linear isotherms, especially to understand the relative importance of different resistances. If the macropore term is considered controlling, equation 3.13 simplifies to:

$$k_i = \frac{15\varepsilon_p D_{pi}}{K r_p^2} \quad (3.14)$$

The MTC for a zeolite adsorbent particle typically assumes macropore diffusional resistance as the limiting resistance.² Under this assumption, equation 3.14 is used to estimate k_i either using literature values to estimate D_p , or through a combination of breakthrough and numerical experiments.

3.3.2 Axial Dispersion

Axial dispersion acts to disperse the concentration wave in packed column operations, just like mass transfer resistances associated with the particle. At low gas velocity, it is caused by molecular diffusion, while at high gas velocities, it is caused by eddy turbulence. In PSA models, the combined effects of axial dispersion are approximated with the axial dispersion coefficient, D_L , often expressed as:²⁴

$$D_L = \gamma_1 D_m + \gamma_2 u d_p \quad (3.15)$$

where D_m is molecular gas diffusivity, u is interstitial velocity, d_p is particle diameter and γ_1 and γ_2 are constants. The first term is the molecular diffusion contribution to concentration gradient spreading and the second term is the eddy turbulence contribution. The constant γ_1 is the inverse of the bed tortuosity factor and 0.7 is a well-accepted estimation for columns of non-adsorbing particles.²⁴ The γ_2 constant is the inverse of the limiting Péclet number ($Pé_\infty$), which is the value $Pé$ ($u d_p / D_L$) approaches at high gas velocity. The common estimation of 0.5 comes from the observation that large particles

approach a maximum Pé number of two at high Reynolds numbers, common in large PSA applications.²⁶

3.3.3 Mass Transfer Zone

In an adsorption process, a feed mixture is introduced at one end of the column and product exits at the other end. As the adsorbate moves from the fluid phase into the adsorbed phase, a concentration wave forms in the column. The concentration wave, or MTZ, travels through the column and eventually reaches the opposite end, illustrated in Figure 3.3. As it exits the column, the adsorbate outlet concentration increases and eventually reaches the inlet concentration. The shape of the exit (“breakthrough”) curve is heavily dependent on the adsorption isotherm shape and whether equilibrium is favorable or unfavorable. Figure 3.4 illustrates how to determine adsorption isotherm favorability. If favorable, the concentration wave is compressive or self-sharpening (Figure 3.5), since the high adsorbate concentration front travels faster than the low adsorbate concentration front because of a material balance in the MTZ. The limit of this wave is a shock wave or a step discontinuity, which cannot occur in reality because adsorption is not instantaneous. A sharp wave front produces a small MTZ and indicates a high adsorption rate and separation efficiency. An unfavorable isotherm produces a dispersive wavefront, the opposite of a compressive front.⁹ This occurs during the desorption step of a PSA process and is illustrated in Figure 3.5. In realistic adsorption processes, mass and heat transfer limitations will spread the MTZ. Mass transfer limitations include diffusional and axial dispersion, as previously discussed. Since adsorption is exothermic and finite heat transfer resistances exist in any packed column,

the adsorbent temperature will vary across the MTZ, which also causes additional spreading.

Breakthrough experiments are often used to determine the adsorption rate in an adsorbent. This test involves inducing a step change in the inlet concentration to a packed column and monitoring the column exit concentration over time. Eventually the MTZ “breaks through” and forms a breakthrough curve as it exits the column, illustrated in Figure 3.6. In essence, a breakthrough curve is mirror image of the MTZ in the column. The shaded region between point *b* and point *c* represent the unused portion of the column. If mass and heat transfer resistances are small and the isotherm is favorable, the breakthrough curve is steep and a sharp MTZ leads to a small length of unused column.

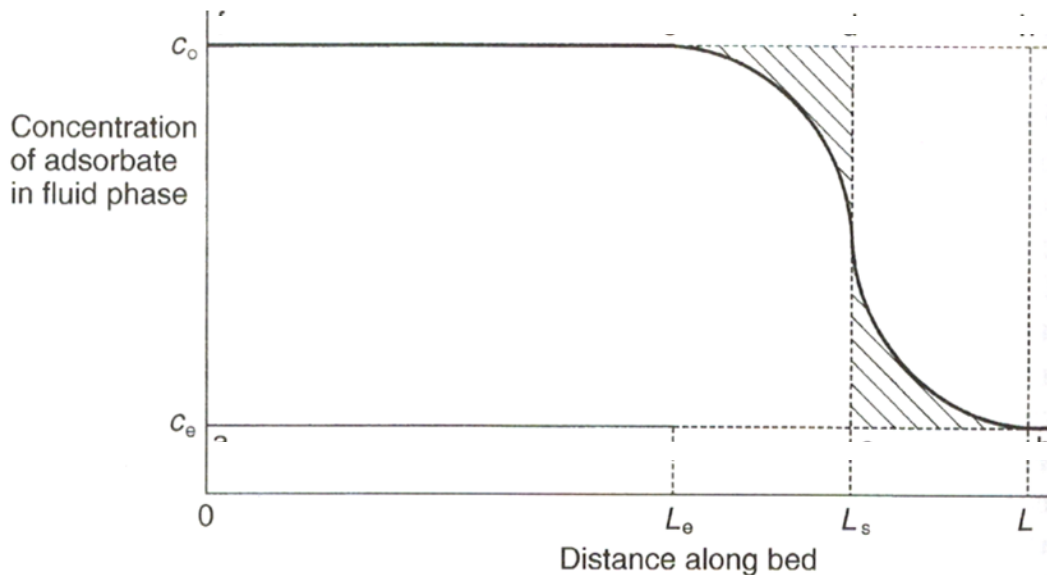


Figure 3.3 Mass transfer zone inside a column. c_0 is the inlet concentration, c_e is the exit concentration, and L is the column length⁷

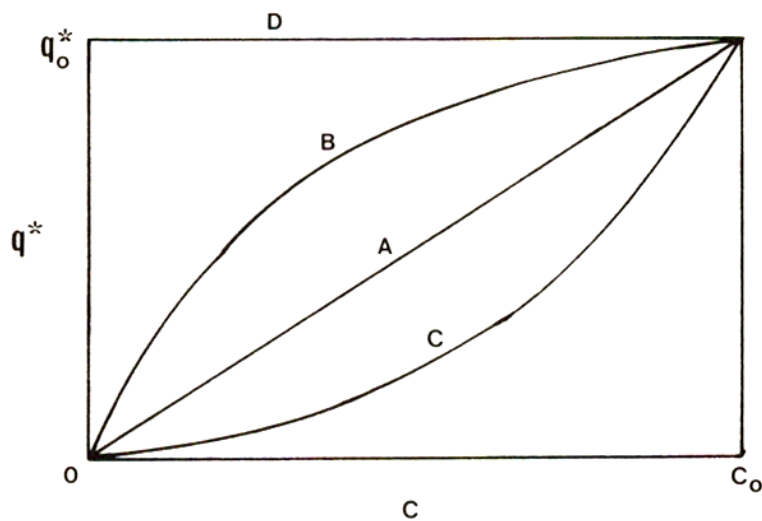


Figure 3.4 Shapes of isotherms in determining the sharpness of concentration wavefronts: (A) linear; (B) favorable; (C); unfavorable; (D) irreversible. $q^* =$ equilibrium amount adsorbed and $C =$ concentration of adsorbate in the gas phase⁹

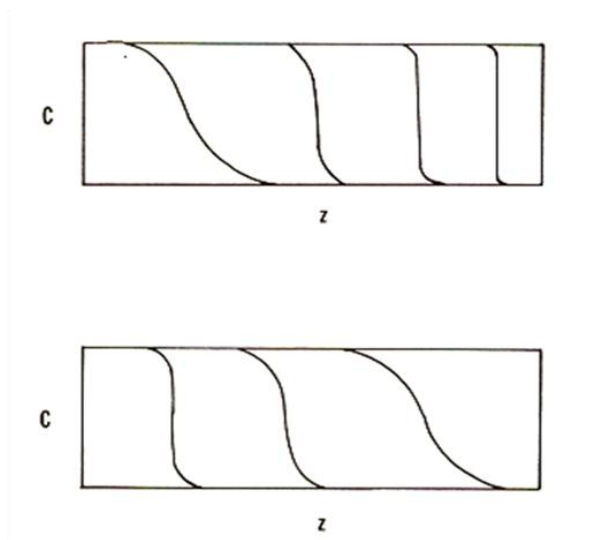


Figure 3.5 Self-sharpening wavefront (top) and dispersive wavefront (bottom). c is adsorbate concentration in the gas phase and z is distance from the column entrance⁸

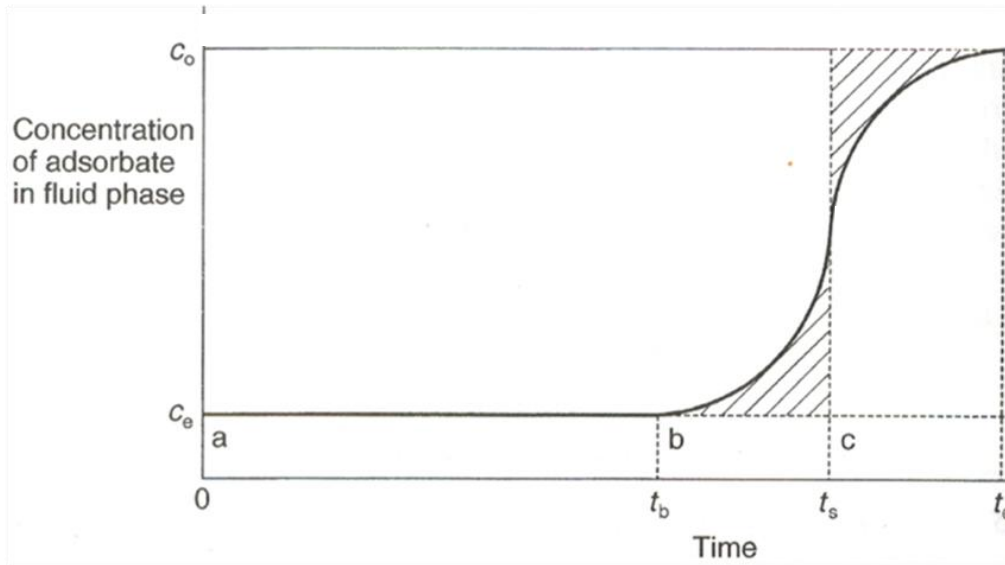


Figure 3.6 Column breakthrough curve. c_0 is the inlet concentration, c_e is the exit concentration, t_b represents the time breakthrough occurs, t_s is the time stoichiometric center reaches the end of the column, t_e is the end of the MTZ ⁷

CHAPTER IV

CHALLENGES OF SMALL SCALE PSA

This chapter demonstrates the key differences between PSA on a large and small scale. It also provides background on the current state of the literature in this research area and discusses the challenges in understanding the limitations of small scale processes. Finally, it highlights current knowledge gaps in literature to demonstrate how this dissertation fits into the field of PSA.

4.1 Effect of Particle Size Reduction in Small Scale PSA

Decreasing adsorbent particle size in packed columns is known to increase axial dispersion effects.²⁶ However, the extent to which it affects the mass transfer rate in PSA processes remains uncertain. Knowledge of the limiting mass transfer resistance in a PSA process is important for process design. Furthermore, PSA simulation models rely on assumptions about mass transfer rate limitations for an adsorption rate approximation. Hence, improving simulation accuracy depends on properly estimating relevant mass transfer limitations in a PSA process.

4.1.1 Current Assumptions

Large diameter zeolite particles (> 2 mm) are well known to exhibit significant mass transfer resistance in their macropores.^{2, 27} Since it represents the dominant resistance in columns packed with these particles, a mass transfer rate controlled by macropore diffusional resistance is typically assumed. Other resistances external to the particle such as axial dispersion and film transfer resistance are usually considered small or negligible. These assumptions generally provide a reasonable estimation of mass transfer limitations for simulations involving large zeolite particles.

Current small scale PSA processes often operate with small particles (~ 0.3 mm to 0.7 mm in diameter) to permit rapid cycling. Smaller particles provide both a higher surface area for diffusional flux into the particle and a shorter diffusional path inside the particle. Decreasing macropore diffusional resistance through particle size reduction increases the influence of other factors affecting the mass transfer rate, particularly effects external to the particle. While this notion is generally accepted in literature, it remains unclear at what particle size these external factors become significant. Zhong et al.²⁸ used a simulation study to determine the effect of LiLSX particle size on process performance. They found axial dispersion effects begin to dominate the mass transfer rate at a particle size < 1 mm for velocities often used in small scale PSA processes. However, the study was never confirmed experimentally. Alpay et al.²⁹ experimentally studied the effect of 5A particle size on a single bed air separation process and found an optimal particle size to maximize product purity. They also found axial dispersion effects were more significant for small particles than predicted by common correlations. Rao and Farooq³⁰ came to a similar conclusion about axial dispersion effects for their single

column small scale PSA process using very small 5A zeolite particles (63-75 μm in diameter). Other studies on packed columns of non-adsorbing particles further confirm that as particle size decreases, the influence of axial dispersion increases significantly.^{26,31}

Other resistances also require consideration when using small particles. While the contribution of a film resistance is typically insignificant for large zeolite particles, this assumption also requires confirmation for small particles. Furthermore, it was recently suggested an additional skin resistance plays a prominent role in the mass transfer rate with small LiLSX particles.³² Skin resistance is attributed to a crystal density increase at the particle surface, which limits diffusion in the outer portion of the particle. A skin may result from shaping methods used during particle manufacture. Further evaluation of the mass transfer rate in columns of these particles is needed to confirm if this applies to all LiLSX particles.

Axial dispersion effects may be overlooked when using a smaller particle size since particles in large scale adsorption processes rarely approach the size where they become significant. A rise in numerical and experimental studies utilizing small particles^{28, 33-38} increases the need to determine the controlling mass transfer resistance in these processes. It will also provide a better understanding of how to improve particle manufacturing methods. Recent advances in adsorbent production techniques target reducing the macropore resistance contribution. For large particles, pore diffusion has been demonstrated to improve significantly through a reduction in binder content using caustic digestion or by incorporating alternative binders.³⁹⁻⁴² However, these same methodologies may not have the same effect on a process where macropore diffusional resistance no longer controls the mass transfer rate.

4.1.2 MTC Estimation for Small Particles

The MTC for large particles is typically found using equation 3.14, first introduced in section 3.3.1.²⁴

$$k_i = \frac{15\varepsilon_p D_{pi}}{K r_p^2} \quad (3.14)$$

While equation 3.14 indicates a significant adsorption rate increase is possible for small particles, it fails to account for the effect of particle size on factors external to the particle. Axial dispersion is naturally not in the adsorption rate equation (equation 3.12) as its effect is explicitly included in the material balance in equation 3.11. However, its effect on column dynamics is similar to diffusional limitations in the particle since it acts to disperse the MTZ. For a linear isotherm, axial dispersion effects are approximately combined with resistances associated with the particle as described in equation 4.1, sometimes referred to as the linear addition approximation for a bimodal pore size distribution.²⁴

$$\frac{1}{k_{overall}} = \frac{K D_L}{u^2} \left(\frac{1 - \varepsilon_b}{\varepsilon_b} \right) + \left(\frac{K r_p^2}{15 \varepsilon_p D_{pi}} \right) + \left(\frac{K r_p}{3 k_f} \right) + \left(\frac{r_c^2}{15 D_{ci}} \right) \quad (4.1)$$

In equation 4.1, the first term on the right side of the equation accounts for the resistance equivalent of axial dispersion effects and is linearly added to macropore, film, and micropore resistance respectively. All four effects on MTZ stretching are clearly indicated, which makes it useful to compare resistances and their dependency on gas velocity (u). Micropore diffusional resistance is usually negligible compared to other contributions for type-1 adsorption in zeolites,^{2, 27} which was confirmed by Wu et al.³² for

LiLSX particles; hence, it was considered insignificant for the analysis in this study. When axial dispersion effects are described through an overall MTC in the adsorption rate term in equation 3.12, a plug flow model replaces the axially dispersed plug flow model in equation 3.11. The linear addition approximation is useful when the axial dispersion term is significant in comparison to the other terms in equation 4.1. It has been demonstrated to provide a suitable MTC estimate even for highly non-linear systems.^{24, 43}

For zeolites, the macropore resistance term in equation 4.1 is typically assumed to dominate $k_{overall}$. However, for small particles, it has been demonstrated the axial dispersion and pore diffusion rate constants in equation 4.1 become comparable.^{28, 44} Furthermore, Wu et al.³² measured $k_{overall}$ experimentally for nitrogen on ~0.5 mm in diameter LiLSX particles and found a much smaller $k_{overall}$ increase than expected based on particle size reduction. While the increase in $k_{overall}$ was high enough to provide the increase in productivity necessary for oxygen generation using small scale PSA, an additional resistance is clearly present that is not accounted for using traditional correlations. The macropore term only accounts for ~1.4% of the overall resistance at a pressure of 2 atm and temperature of 303.1 K, while axial dispersion (24.8%) and film resistance (11.4%) play much larger roles. The authors suggest the remainder of the resistance (62.3%) is due to a skin. However, as demonstrated in a later section, using a literature correlation that properly accounts for higher axial dispersion effects in columns of small particles also explains the difference.

4.1.3 Axial Dispersion Coefficient Estimation

No consensus exists in literature for describing axial dispersion effects in columns packed with small particles as estimates of the axial dispersion coefficient (D_L) vary depending on the correlation used. Some studies have continued to use a correlation common for large particles.^{34, 45-47} Others have incorporated an alternative correlation that increases axial dispersion effects for small particles.^{30, 38} It is currently unknown how the estimate of D_L affects simulation accuracy, which further contributes to a lack of understanding of its importance.

As discussed in section 3.3.2, equation 3.15 is typically used to estimate the axial dispersion coefficient, D_L , with γ_1 and γ_2 assumed as 0.7 and 0.5 respectively.

$$D_L = \gamma_1 D_m + \gamma_2 u d_p \quad (3.15)$$

While these estimates of γ_1 and γ_2 are suitable for columns of large particles, their applicability to columns of small particles is questionable. As early as 1968, Edwards and Richardson⁴⁸ demonstrated the $Pé_\infty$ for small particles (< 2 mm) was much lower than 2 ($Pé_\infty = 1/\gamma_2$), which requires γ_2 to be much higher than 0.5. Suzuki and Smith³¹ further confirmed this using small glass beads to determine the effect of particle size on dispersion. They found a clear change in $Pé_\infty$ as particle diameter decreased for small particles. Langer et al.²⁶ also found a similar relationship, illustrated in Figure 4.1. Although the reason $Pé_\infty$ is a function of particle size for small particles is not fully understood,²⁴ Moulijn and Van Swaaij⁴⁹ reason the difference is due to channeling within the column (rather than just near the wall). They postulate that small particles tend to

form agglomerates, which act as larger particles when the strong interaction forces between the particles overcome the forces of gravity and drag.

It has also been suggested the estimate of γ_1 in equation 3.15 is much larger (~ 50 for a rectangular isotherm) for strongly adsorbing particles. The proposed higher value accounts for direct transport through the particle due to an asymmetric concentration profile surrounding the particle at low gas velocity.⁵⁰ As a result, the amount of effective axial dispersion increases in the laminar and transitional flow regimes. While this apparently has an impact in liquid chromatography where the influence of surface diffusion is significant at low velocity,⁵¹ it has not been demonstrated to be applicable for gas adsorption systems. The value of ~ 0.7 for γ_1 currently remains the best estimate for such systems.

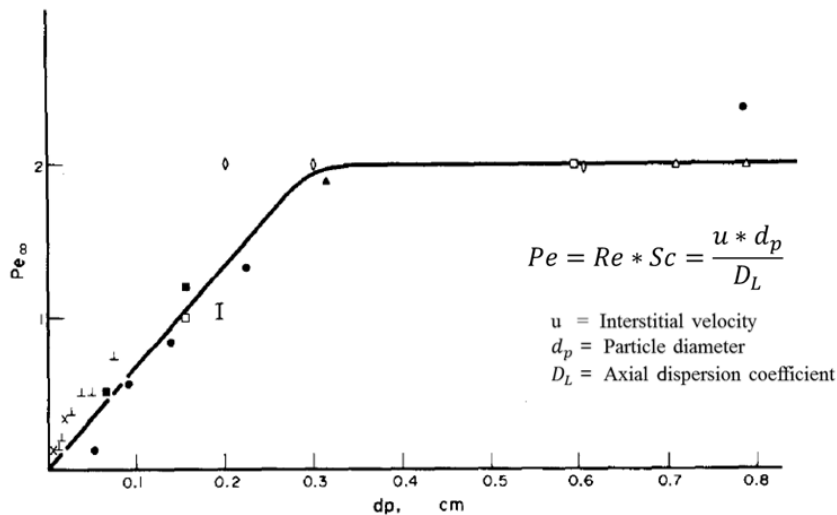


Figure 4.1 Limiting Peclet number vs. particle diameter for flow through packed beds²⁶

4.1.4 Impact of Higher Axial Dispersion Effects with Small Particles

The estimate of D_L is much higher for small particles than large particles if the estimate of γ_2 is much larger than 0.5. Since the traditional method of matching simulated breakthrough curves to experimental data relies on a reasonable estimate of D_L to determine D_p experimentally, an artificially low estimate of D_p is possible if D_L is not estimated correctly. Furthermore, a higher D_L increases the contribution of axial dispersion in equation 4.1 while the particle size decrease reduces the contribution of macropore diffusional resistance. Hence, a macropore resistance limited system may no longer be a suitable assumption.

To better understand how significant the effects of axial dispersion might be, a case study was used to compare different mass transfer rate assumptions using a 0.5 mm particle. In *case 1*, film resistance was considered negligible and D_L was approximated using equation 3.15 with γ_1 and γ_2 assumed as 0.7 and 0.5 respectively. In *case 2*, D_L was estimated with the same equation, but now the effect of film resistance was added according to equation 4.2.²⁴

$$Sh = \frac{k_f d_p}{D_m} = 2.0 + 1.1Sc^{1/3}Re^{0.6} \quad (4.2)$$

In *case 3*, film resistance was considered negligible and γ_2 was estimated using equation 4.3:²⁶

$$\frac{1}{\gamma_2} = 6.7d_p \quad (4.3)$$

where d_p is in cm. Finally, *case 4* used the same correlations as *case 3* to determine D_L , but now film resistance was included according to equation 4.2. In all cases, D_p for nitrogen was found from equation 4.4 using typical literature correlations for D_m and D_k .²⁴

$$D_p = \frac{1}{\tau_p} \left(\frac{1}{\frac{1}{D_m} + \frac{1}{D_k}} \right) \quad (4.4)$$

A pore tortuosity (τ_p) of 3 was assumed since studies on larger LiLSX particles have estimated it between 2 and 4.^{28, 39, 42} The dimensionless Henry's law coefficient (K) was found from previously determined DSL isotherm parameters⁵² assuming conditions of $T = 313$ K, $P = 267$ kPa, and a gas composition of 0.75/0.25 N_2/O_2 so the predictions are comparable to future experiments in this study. Table 4.1 summarizes the constants and correlations used in all four cases.

Figure 4.2 demonstrates the $k_{overall}$ varies significantly depending on the assumptions made. As velocity increases, the controlling mass transfer limitation switches from axial dispersion control to macropore diffusion control. This is illustrated by the approach of $k_{overall}$ in Figure 4.2 to the horizontal “macropore only” line. As the $k_{overall}$ approaches the horizontal line, the macropore term in equation 4.1 becomes controlling. When $k_{overall}$ is far from the horizontal line, axial dispersion effects are controlling. It is evident the inclusion of film resistance has a noticeable impact on $k_{overall}$ if axial dispersion effects are low (*Case 1 and 2*). However, a higher axial dispersion coefficient has a much greater effect on $k_{overall}$, especially at lower Reynolds numbers (*Case 3 and 4*) Small scale PSA processes often operate at low to moderate Reynolds

numbers where the difference between the predictions is the greatest. Additionally, breakthrough experiments using small particles are often conducted at low Reynolds numbers since the response time of gas analyzers make high velocity waves difficult to accurately measure. Since such a difference in $k_{overall}$ exists depending on the correlation used to estimate D_L , it is critical to determine which one is more appropriate for use in process simulators.

Table 4.1 Comparison of parameters used for estimates of $k_{overall}$ in Figure 4.2. Pressure = 267 kPa $d_p = 0.05$ cm, $D_p = 0.02$ cm²/s, $K=16.5$

	γ_1 of D_L	γ_2 of D_L	k_f
Case 1	0.7	0.5	∞
Case 2	0.7	0.5	Eq. 4.2
Case 3	0.7	3	∞
Case 4	0.7	3	Eq. 4.2

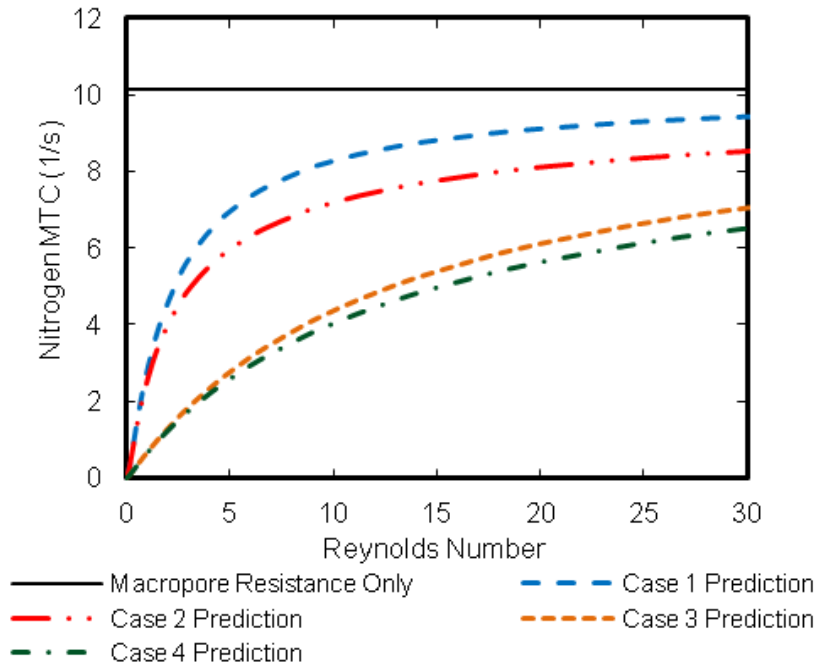


Figure 4.2 Comparison of predicted overall nitrogen MTC using constants and correlations according to Table 4.1. Overall gas pressure = 267 kPa, gas composition (N_2/O_2) = 75/25

4.2 Small Scale PSA

Small scale PSA is an advancement of PSA technology for the purpose of process size reduction. It is typically distinguished from traditional PSA by rapid cycling (< 30 seconds) of small adsorbent particles (< 1 mm). Larger scale PSA typically operates with cycle times on the order of minutes and a particle size > 1.5mm. Cycle time reduction requires an increase in gas velocity for a given amount of adsorbent. This raises several issues such as sorbent fluidization, increase in column pressure drop, and higher gas dispersion.¹² In addition, a higher gas velocity reduces contact time with the solid, necessitating smaller adsorbent particles (<1mm). For a finite adsorption rate, the result

is a stretched mass transfer zone (MTZ), which causes premature breakthrough and a reduction in product recovery. However, provided the productivity increase is greater compared to the loss in column working capacity, process size reduction is possible with higher cycling frequency.¹¹ This is ideal for certain applications like a POC. Small scale processes typically increase solid productivity with faster cycling. The tradeoff is a lower recovery, which leads to higher overall power consumption for a desired product flow rate.⁵³ Furthermore, it reduces the solid working capacity, which limits the achievable process productivity.⁴⁴

4.2.1 Evolution of Small Scale PSA

Small scale PSA originally was called rapid PSA (RPSA) and involved a single column process using very small particles and high gas velocities to create a large pressure gradient across the column.^{54, 55} This permitted a simple 2-step process with column self-purging and a continuous product flow rate at one end of the column, while swinging pressure on the other end. A small separation unit was possible by operating with a high cyclic frequency to reduce the amount of solid adsorbent. Parameters such as an optimal particle size and benefits of an additional delay step have been studied for the application of air separation.²⁹

POCs have recently renewed interest in small scale, fast cycling PSA, also often labeled RPSA. However, these systems operate with 4-step Skarstrom cycles, more similar to larger scale processes than the original RPSA definition given above. To facilitate a portable process unit, column length is much shorter (~10-20 cm) compared to the traditional RPSA concept (>100 cm). Even with short cycle times, pressure drop across columns of this length is not high enough to permit RPSA operation as it was

originally designed. These systems operate with distinct steps of constant pressure or pressure change in the column.

4.2.2 Limitations of Small Scale PSA

Experimental small scale PSA studies for POC applications often focus on how purge to feed ratio, product purity, and adsorbent type affect process performance.^{36, 56, 57} Other studies have numerically investigated the effect of rapid cycling on a specific PSA step.^{45, 46} Limitations of small scale systems have received less attention. One method of studying the limits of small scale PSA entails increasing cyclic frequency while keeping other process parameters (i.e. pressure ratio, product purity) constant. A cyclic frequency limit is represented by a minimum bed size factor (BSF) at a specific cycle time. Since BSF is inversely related to productivity, a minimum represents an adsorbent utilization limit and defines a lower limit on operating speed; hence the minimum size of an oxygen concentrator.

Several recent experimental studies^{35, 38} have observed an adsorption utilization limit for their small scale processes. While the exact cause of a minimum remains unclear, it has been suggested the combined effects of pressure drop, mass/heat transfer resistances, and non-isothermal operation eventually cause it to occur at a specific cycling rate.⁵⁸ A recent numerical study demonstrated how the cumulative effect of mass, heat, and momentum resistances affected process performance using a 5A zeolite to separate nitrogen and helium.⁴⁷ The study demonstrates non-isothermal operation and mass transfer resistances are the most significant contributions to a minimum BSF, while pressure drop and finite heat transfer resistance represent much smaller contributions.

However, the authors mention these conclusions will not necessarily apply to other systems since they depend on adsorption properties and process design. Another numerical study reached an alternative conclusion suggesting system dynamics (i.e. fastest achievable cycle) limited adsorption utilization in their process.³⁴

The limited experimental data studying limitations of small scale processes largely involve single column concepts.^{30, 35, 38, 59} While some advantage is gained from a single column setup with respect to equipment size, multiple column systems are much more power efficient. An additional column(s) permits a pressure equalization step, which significantly increases product recovery; hence reducing the power requirement and battery size for a given production rate. This study seeks to determine if a minimum BSF also exists for a dual bed small scale PSA process.

4.3 Possible Causes of a Minimum BSF

Increasing process speed reduces the solid inventory necessary for a desired product flow rate. While this decreases the BSF, the tradeoff is a loss in column working capacity. With increasing cyclic frequency, working capacity loss eventually overcomes the productivity gain of rapid cycling, causing the BSF to go through a minimum. While this minimum is generally attributed to non-idealities mentioned in the previous section (i.e. pressure drop, non-isothermal operation, mass transfer resistances), an advantage in process design will be gained if a specific cause is identified.

4.3.1 Pressure Drop

A common concern when using small particles is column pressure drop will reduce process performance. However, the extent of this performance decline is difficult

to quantify. While it has been recognized that the importance of pressure drop increases under faster cycling conditions,⁶⁰⁻⁶³ it has yet to be determined if column pressure drop impacts small scale PSA performance enough to justify considering it in process design. Pressure drop can reduce product recovery through the premature breakthrough of a stretched MTZ.^{60, 64} It may also reduce recovery through a higher purge step operating pressure, resulting in a larger loss in purge gas during this step.^{45, 65} The reason for a reduction in working capacity is more intuitive. Column pressure drop reduces the adsorption step nitrogen loading at the product end of the column. During the regeneration steps, the nitrogen unloading at the product end of the column is also reduced. Additionally, the pressure drop during regeneration steps is a larger fraction of absolute pressure; hence properties in the column vary more substantially from one end to the other during these steps.

The previously cited studies largely focus on pressure drop effects during a specific step of a PSA cycle and not on the cumulative effect on process performance. A better understanding on how column pressure drop affects overall process operation is needed to better design small scale PSA processes. Several computational studies have attempted to accomplish this. A recent study provided an individual and cumulative assessment of how various mass, heat, and momentum resistances affect product recovery and productivity of a PSA process separating a mixture of nitrogen and helium.⁴⁷ It demonstrated pressure drop had a small effect on recovery and productivity at cycle times under 4 seconds. Yang et al.⁶⁶ also used a simulated multi-bed PSA process to show pressure drop has only a small influence on the performance of a PSA process separating a H₂/CO mixture. While these computational efforts indicate pressure

drop has a limited effect on process performance, experimental confirmation of this notion is lacking.

4.3.2 Heat Transfer Limitations

Heat transfer is significant in PSA processes since adsorption is exothermic and desorption is endothermic. Various heat transfer resistances in the column increase or decrease the adsorbent temperature relative to isothermal conditions. Heat transfer from the gas phase to the column wall and from the column wall to the ambient environment may be important for small columns, but their effect is reduced greatly as column diameter increases. Hence, large scale columns typically operate adiabatically while small scale columns may approach isothermal operation. However, unless working with dilute concentrations and a low heat of adsorption, even small scale processes do not approach isothermal operation.²⁴ Heat transfer between the particle and flowing gas is quite fast according to typical Nusselt number correlations and is generally considered instantaneous.

4.3.3. Mass Transfer Limitations

Mass transfer limitations that would affect a minimum BSF have already been discussed in previous sections. The primary potential contributors are axial dispersion effects and mass transfer resistance in the macropores of the adsorbent. Other potential limitations include film and micropore diffusional resistance and the formation of a skin on the adsorbent particle.

4.3.4 BSF Model

Rezaei and Webley⁴⁴ previously developed a relationship between productivity and cycle time that accounts for various non-idealities:

$$\text{Productivity} = \frac{1}{\text{BSF}} = k'(WC_{ideal} - K\Delta P) \left(1 - \frac{L_{MTZ}}{L}\right) U \quad (4.5)$$

where K is an equilibrium constant (i.e. Henry constant for a linear system), ΔP is column pressure drop, WC_{ideal} is isothermal working capacity, L is column length, L_{MTZ} is the mass transfer zone (MTZ) length, and U is gas velocity. Although their application was comparing structured and non-structured adsorbents, the relationship also helps explain why a minimum BSF exists in small scale PSA as well. The expression relates working capacity to productivity (or BSF) and U through a proportionality constant k' . ΔP and L_{MTZ} both increase as a function of gas velocity ($U \propto 1/\text{cycle time}$) and reduce isothermal working capacity. Pressure drop reduces working capacity because the adsorbent at one end of the column no longer experiences the same swing in pressure as the other end. A longer MTZ increases the unused column length, which also limits available working capacity.

Equation 4.5 exhibits a minimum BSF as gas velocity increases. The velocity and absolute value of the minimum BSF depends on the extent to which pressure drop and MTZ spreading contribute to working capacity reduction. At the limit of isothermal operation and local equilibrium, the MTZ length is not a function of velocity and pressure drop determines the velocity and depth of the minimum BSF. When mass and heat transfer limitations are significant, the MTZ length is a function of velocity and a minimum may develop even if pressure drop is negligible.

4.4 Study Aims and Experimental Plan Overview

4.4.1 Study Aims

It is evident from the literature discussed earlier that axial dispersion effects are more significant for the particle size used in small scale PSA processes. However, there are no current studies that demonstrate how much this affects the adsorption rate of small LiLSX particles. Since the adsorption rate significantly affects process performance, properly estimating it for process simulators is critical. The first aim of this study is to fill this knowledge gap in literature. Understanding the impact of axial dispersion effects on small scale PSA process design will also help fulfill the other aims in this study.

While small scale PSA processes operate in a similar fashion to larger scale processes, several key differences exist including a much smaller particle size, shorter column length, and a faster cycling rate. These differences increase the complexity of understanding the limits of small scale PSA processes. While single column studies have demonstrated a minimum BSF exists, it has never been demonstrated for a dual-column process. Furthermore, a true understanding of why the minimum occurs is still lacking. The second main aim of the study is to increase understanding in this area by measuring a minimum BSF for a two-column process. The final aim of the study is then to determine what causes a minimum BSF. Through a better understanding of small scale PSA process limitations, it is hoped the design of these processes may be improved in the future.

4.4.2 Overview of Experimental Plan

To fulfill the aims of this study, three primary studies on two different experimental systems were conducted. Axial dispersion effects are best evaluated using a breakthrough system, explained later in Chapter 5, rather than an experimental PSA system. This study is hereafter referred to as the “breakthrough study”. Equation 4.5 indicates that pressure drop is a potential limitation on adsorbent utilization; hence, an experimental study was designed to better understand the effect it has on PSA performance. A small scale PSA process was used to measure process performance at different levels of pressure drop. This study is referred to hereafter as the “pressure drop study”. Finally, in order to understand what causes a minimum BSF, it needed to be measured experimentally. The final study focuses on experimentally measuring a minimum BSF using the same two column, small scale PSA process as the pressure drop study. This study is referred to hereafter as the “minimum BSF study”.

CHAPTER V

MATERIALS AND METHODS

This chapter introduces the type of zeolite, instruments, and devices utilized to conduct the experiments for this dissertation. Data collection methods for breakthrough and PSA experiments are also discussed in detail along with the conditions of the experiments. Finally, the dynamic PSA model used in this dissertation to support and analyze data is introduced.

5.1 Type of Zeolite

The zeolite in this dissertation was a LiLSX zeolite with a Si/Al ratio near 1.0, a high Li^+ exchange, and manufactured to increase the adsorption rate, specifically through a particle size ~ 0.5 mm in diameter and a proprietary clay binder.

5.2 Isotherms

Process work requires knowledge of the adsorbent equilibrium properties. Equilibrium data was collected volumetrically by another graduate student in our lab (Qian Qian Zhou) at three different temperatures for both pure oxygen and nitrogen. The data along with the DSL fits are shown in Figure 5.1 and 5.2. The DSL parameters regressed from the data are shown in Table 5.1.

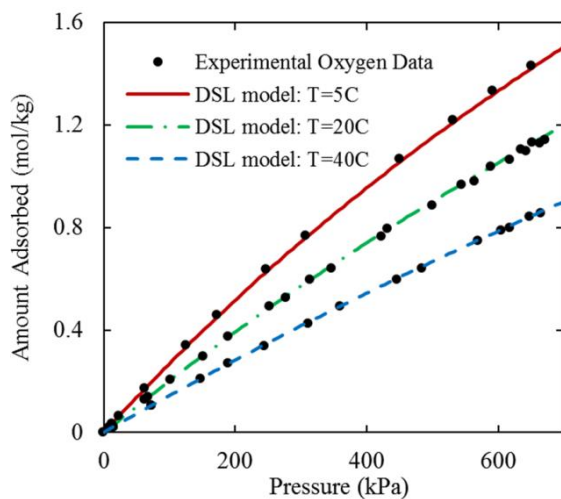


Figure 5.1. Oxygen isotherms for LiLSX zeolite.⁶⁷

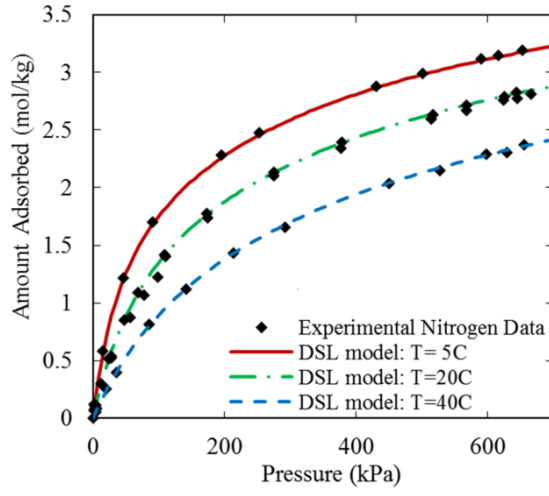


Figure 5.2. Nitrogen isotherms for LiLSX zeolite.⁶⁷

Table 5.1 Nitrogen and oxygen DSL parameters for LiLSX particles used in simulations.⁶⁷

	Nitrogen	Oxygen
$n_{s,1}$ (mol/kg)	2.025	1.426
$b_0 \times 10^{-6}$ (1/kPa)	0.124	0.158
Q_b/R (K)	3365	2373
$n_{s,2}$ (mol/kg)	2.402	6.177
$d_0 \times 10^{-6}$ (1/kPa)	0.513	3.386
Q_d/R (K)	2263	1211

5.3 Column Packing and Activation

Any adsorption system requires a careful column packing to ensure the amount of zeolite in the column is accurately known. Future process design calculations are highly dependent on these values since the amount of processed gas is dependent on adsorption capacity. The packing procedure was similar for all columns in this dissertation.

Initially, a column was packed with a known amount of zeolite prior to activation. Activation involves heating the adsorbent to eliminate contaminants such as water and carbon dioxide that would reduce the selectivity and capacity. Column activation was performed in a furnace under vacuum and low helium flow. The temperature was increased 1 °C every minute until the temperature reached 120 °C. The furnace was then held at this temperature for an hour before again increasing 1 °C every minute until the temperature reached 345 °C, at which the temperature was held for at least seven hours. The column in the furnace was then pressurized with helium to atmospheric pressure and allowed to cool to room temperature. Lastly, the column was weighed to determine the amount of contaminants lost during activation so a “dry” zeolite content could be determined before installation into the PSA or breakthrough system. The weight of the left over helium gas in the column was neglected in this calculation.

5.4 Breakthrough Study

5.4.1 Breakthrough system

Measuring the MTZ length and kinetic parameters of the LiLSX adsorbent was completed using a breakthrough column. The breakthrough system used in this

dissertation is shown in Figure 5.3. It is a simple apparatus with a column filled with spherical particles of LiLSX. The column diameter was chosen to keep the column to particle diameter ratio above the commonly accepted threshold of 20 to prevent wall effects.⁶⁸ Other relevant column specifications are listed in Table 5.2. Specifics related to instruments and operating details may be found elsewhere.⁶⁹

5.4.2 Breakthrough Measurements

Breakthrough experiments were conducted by another graduate student in our lab (Mihir Patel), however the data analysis was primarily done by the author of this dissertation. Pure nitrogen (99.999% purity) and oxygen (99.98% purity) was supplied by Matheson Gas Products. The outlet gas stream of the column was monitored by a Hiden Analytical process mass spectrometer with a response time ~ 300 ms, which detected the molecular ions of O_2 and N_2 . The column was initially saturated at room temperature with pure oxygen at 267 kPa before introducing a $\sim 75/25$ mixture of nitrogen and oxygen respectively at the same pressure. The pressure was chosen in the range of the adsorption step of typical vacuum PSA processes. Experiments were run until the outlet concentration reached the inlet concentration at a range of gas velocities within the limits of the system. The effect of external void volume after the column was determined to be negligible in the range of the experiments run. Further discussion on this topic is available in Appendix B.

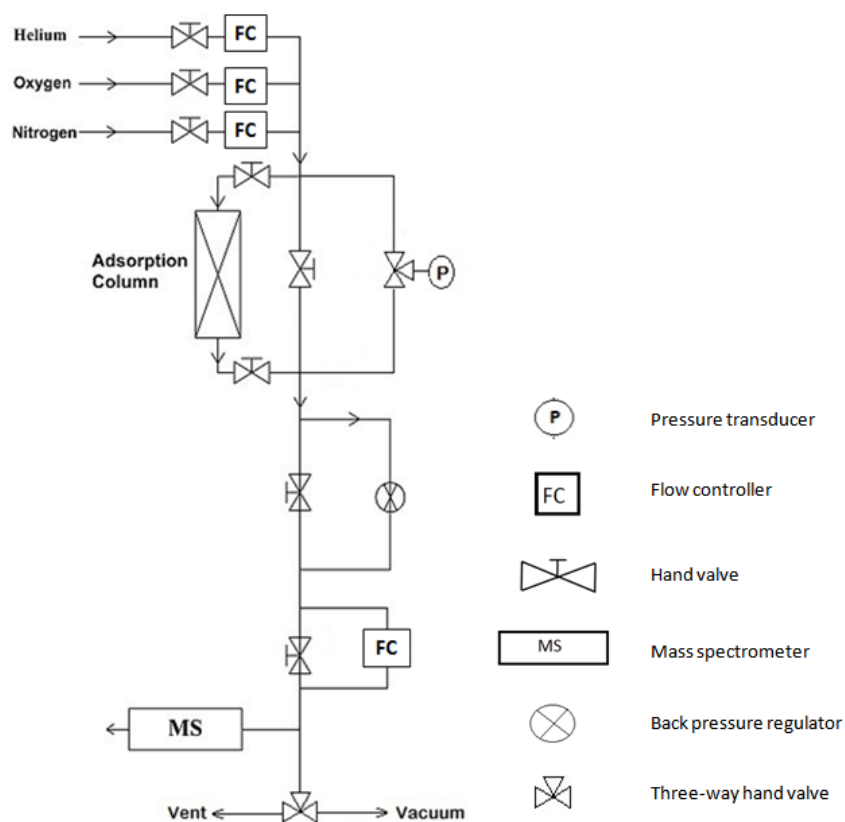


Figure 5.3 Breakthrough experimental setup. Note: adsorption column includes a thermocouple at the exit of the column for monitoring exit gas temperature

Table 5.2 Breakthrough column specifications

diameter	1.09 cm
length	15 cm
LiLSX zeolite	8.64 g
avg. spherical particle size	0.05 cm
bulk density	0.62 g/cm ³
ε_b	0.38
ε_p	0.35

Most breakthrough experiments in literature are performed by an adsorbable component displacing helium. Two reasons are usually cited for this choice: 1) the resulting data can be integrated to determine equilibrium information (as a point on an isotherm). Since we measured pure and binary equilibrium data for N_2/O_2 in a separate volumetric instrument, there was no need to measure equilibrium data with this apparatus; 2) From a kinetics stand point, which is the main reason for performing breakthrough experiments, helium is so small and light that it offers little resistance to N_2 diffusion in the pores, hence a “true” nitrogen mobility is measured experimentally. From a purely scientific point of view, this is correct; however we are trying to generate correlations for engineering use in process simulators where N_2 is displacing O_2 . If a process model is going to use only one MTC for N_2 (irrespective of what the other component is), experiments to determine the MTC should be closer to reality, which requires N_2 to displace O_2 . A similar procedure was used in a previous study on extruded mordenite pellets.⁷⁰ Using O_2 as the initial condition has an additional advantage of limiting the inevitable temperature increase in the column during breakthrough experiments. This is simply because of the heat removed through the desorption of O_2 .

5.4.3 *Constant Pattern*

Breakthrough analysis in this dissertation relies on the assumption of a constant pattern forming in the column during the experiment. A constant pattern forms for any favorable system, such as the one in this dissertation (N_2 -LiLSX). More detail on why this occurs is provided in section 3.3.3. A constant pattern arises when the concentration profile in the MTZ does not change as the MTZ travels through the column. It typically develops a short length into the column, sometimes referred to as the “entrance length”.

The column length was sufficiently long such that entrance length had a negligible impact on the breakthrough results.

5.4.4 MTC Calculation

In this study, breakthrough experiments were used to measure a MTC at a fixed pressure and room temperature while varying the velocity. Since axial dispersion and the film transfer coefficient both depend on velocity while intraparticle transport mechanisms (i.e. macropore/micropore diffusion and surface diffusion) do not, this provides a convenient method of determining the significance of diffusional limitations external to the particle. The overall MTC was estimated from experimental breakthrough experiments by integrating equation 3.12 between the limits defined as the MTZ.³² This gives equation 5.1:

$$\int_{n(t_{0.05})}^{n(t_{0.9})} \frac{dn_{N_2}}{n_{N_2}^* - n_{N_2}} = k_{overall}(t_{0.9} - t_{0.05}) \quad (5.1)$$

where $t_{0.9}$ and $t_{0.05}$ is the experimental time the dimensionless outlet nitrogen concentration, c/c_0 , reaches 0.9 and 0.05 respectively, c_0 is the inlet nitrogen concentration, n_{N_2} is the average adsorbed phase concentration of nitrogen over an adsorbent particle, and $n_{N_2}^*$ is the equilibrium value of the adsorbed phase concentration of nitrogen. Defining the MTZ in this manner is common practice since it is often difficult to detect where the MTZ exactly starts and stops, especially at higher gas velocities. It additionally avoids the long tail caused by deviation from isothermal operation due to temperature effects. Since the experiments were run at ambient conditions, some temperature rise in the column is inevitable due to the heat of

adsorption. For a nitrogen-LiLSX system, the thermal wave travels behind the concentration wave. This means that the heat effects primarily affect the tail end of the MTZ. A thermocouple placed at the exit of the column indicated that the temperature increased around 17 °C for the lower velocity runs, and 19 °C for the higher velocity runs. While the response time of the thermocouple was not fast enough to capture the true thermal wave, it does provide an estimate of the thermal gradient that exists across the MTZ. Since the increase in temperature was relatively constant, the heat effects do not change significantly for the range of gas velocities used in this study. To avoid including heat effects in the MTZ, 0.9 of the inlet concentration was used to define the end of the MTZ. This more reasonably approximates an isothermal MTZ defined between 0.05 and 0.95, which is the more common MTZ definition. The reasoning behind this is further described in the appendix. This does not affect the calculation in equation 5.1 because a non-isothermal model is used to determine n and n^* as described in the next paragraph. However, this change is important when the data is transformed to MTZ data to facilitate use of the van Deemter model (described in section 5.4.5) since that model does not account for heat effects in describing the amount of MTZ spreading.

A dynamic PSA model described in a later section (5.6) was adapted for breakthrough experiments and used to match a simulated breakthrough curve to an experimental curve. In brief, the model is a non-isothermal, non-isobaric model that accounts for equilibrium and the adsorption rate using the dual-site Langmuir and linear driving force (LDF) model respectively. The only change made to the model for this study was to use plug flow and account for D_L through the linear addition approximation rather than axially dispersed plug flow. The primary reason for using the model was to

improve the estimation of the integral in equation 5.1. While the nitrogen component of n^* and n may be found from an equilibrium model and experimental data, the number of points in the MTZ becomes limited as gas velocity increases. The simulated curve increases the amount of points in the MTZ to improve the accuracy of the integration. Furthermore, since the experiments were run near adiabatic conditions, thermal effects are better described through use of the model rather than attempting to measure them experimentally. An example of a typical breakthrough curve along with the model representation of the curve is presented in Figure 5.4. Since the model is non-isothermal, it is able to reasonably represent the experimental curve and account for the shift in equilibrium due to the temperature increase. The predicted rise in temperature in the outlet stream ranges from 20 °C at the lower gas velocity experiments to 23 °C at the higher gas velocity experiments. Both n and n^* were calculated from the exit molar flow rate, pressure, and temperature of the model. The variable n was found from a differential balance of the adsorbate as described by Wu et al.³² and in Appendix B. The variable n^* was determined from gas properties at the simulated column exit conditions at time t .

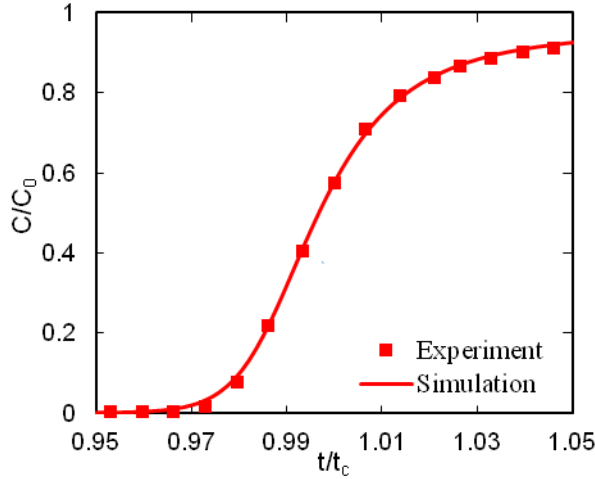


Figure 5.4 Comparison of experiment and simulation breakthrough curve at 267 kPa, room temperature and a inlet N₂/O₂ gas mixture of 0.75/0.25. The average superficial velocity across MTZ was 2.8 cm/s

5.4.5 *van Deemter Model*

While the linear addition approximation is useful for measuring an overall MTC, it is not a good model to estimate relevant mass transfer parameters such as τ_p and D_L using regression analysis. The van Deemter model provides a convenient method for distinguishing between axial dispersion effects and mass transfer resistances due to the particle. Although developed for linear chromatography, the van Deemter expression is often applicable as an engineering approximation for moderately non-linear systems.^{24, 71} The van Deemter model⁷² says the height equivalent to a theoretical plate (HETP) for a linear system is expressed as:

$$HETP = A + \frac{B}{u} + Cu \quad (5.2)$$

where $A = 2\gamma_2 r_p$ (eddy diffusivity term of the axial dispersion coefficient), $B = 2\gamma_1 D_m$ (molecular diffusivity term of the axial dispersion coefficient) and $C \approx 2\varepsilon_b / [(1 - \varepsilon_b)(Kk_i)]$ accounts for particle mass transfer resistance. Other variations of the model exist that include factors such as film resistance through a velocity dependency of the A term.^{73, 74} Differentiating between the effects of eddy turbulence and film diffusion is notoriously difficult since they both act to disperse the concentration wave in a similar manner.⁷⁴ Since significant film diffusion effects were not expected, it was beyond the scope of this study to use more complex models.

HETP was estimated from the height of a transfer unit (HTU) assuming $\text{HETP} \approx \text{HTU}$.⁷⁵ In linear chromatography, $\text{HTU} = L/\text{NTU}$ where NTU is the number of transfer units. However, for an adsorption column, HTU is found from the expression $\text{HTU} = \text{MTZ}/\text{NTU}$ where the calculation is performed across the defined limits of the MTZ and NTU is the integral of equation 5.1. While this approach is only strictly applicable to linear systems, it is a reasonable approximation for non-linear systems, provided it is not a strongly non-linear system. The MTZ length was found using the length of unused bed (LUB) approach.⁷¹ This approach is applicable for systems with a favorable isotherm that develop a constant profile within the column. With this method, the MTZ length is approximated from breakthrough experiments as:

$$L_{\text{MTZ}} = u_w \text{MTZ}_{\text{time}} \quad (5.3)$$

where u_w is the wave (constant profile) velocity. The wave velocity is determined using equation 5.4:

$$u_w = \frac{L}{t_c} \quad (5.4)$$

where L is the column length and t_c is the time the stoichiometric center exits the column.

MTZ_{time} and t_c were found based on the same 0.05 and 0.9 fraction of the inlet composition used in the MTC calculation.

5.5 PSA System

The apparatus used to conduct PSA experiments is a complex system with many valves so the user can produce and control a cyclic process. The system is made of 1/8 inch stainless steel tubing and fittings that connect various types of valves and flow controllers. It is highly instrumented so the physical changes occurring at different points in the process can be measured to provide information on process performance. The system is capable of measuring pressure, temperature, flow rate, and gas composition. The data is collected by a data acquisition system and systematically displayed on a computer screen.

5.5.1 PSA Flow Diagrams

The system is divided into three sections relative to the columns. Figure 5.5 shows a schematic of the exit manifold section of the system, Figure 5.6 shows a schematic of the feed section, and Figure 5.7 shows a schematic of the product section. Table 5.3 provides a key for the symbols found in the figures. The feed side of the columns is where feed gas enters and waste gas exits. The product end is where product gas exits the column and purge gas enters the column. The exit manifold lies in between the feed end and the product end. It contains a manifold of valves that control how gas exits the system.

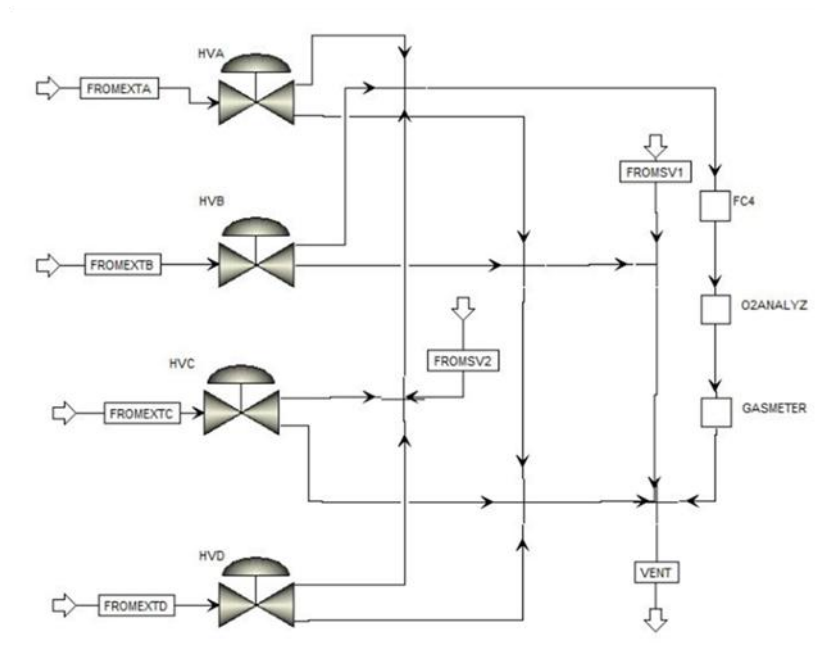


Figure 5.5 PSA middle exit manifold schematic

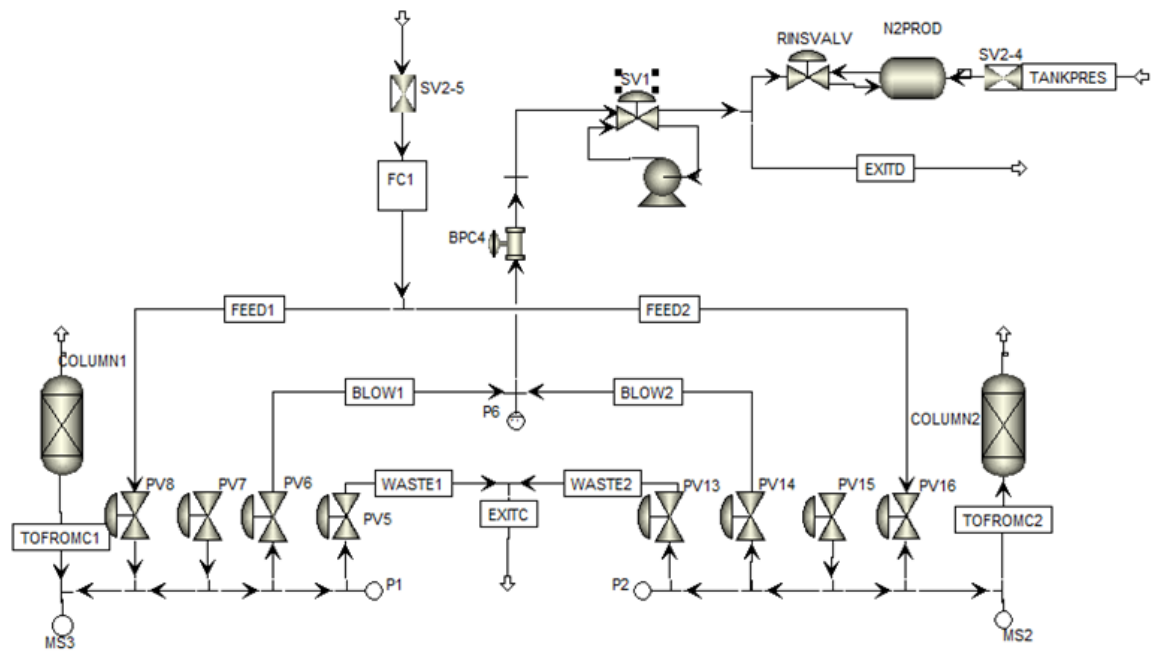


Figure 5.6 PSA system feed side schematic

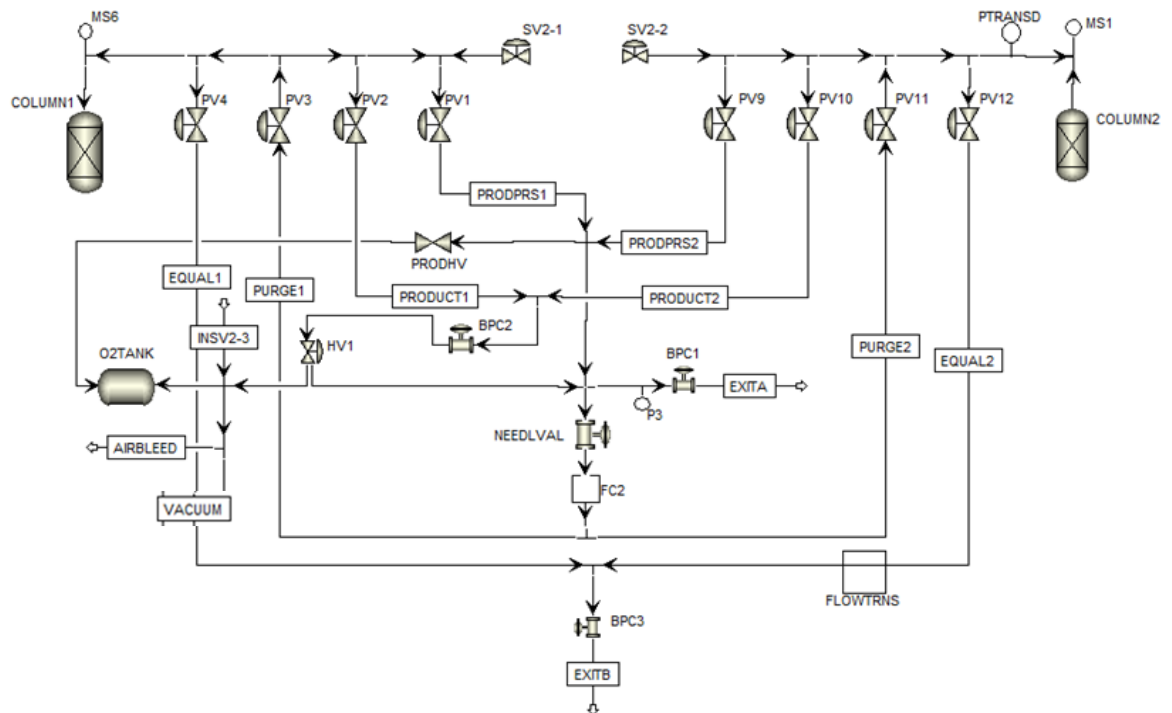




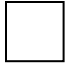






Figure 5.7 PSA product side schematic

Table 5.3 PSA schematic symbol description

Acronym	Symbol	Meaning
PV#		Pneumatic valve
COLUMN#		Adsorption column
BPC#, NEEDLVAL		Back pressure controller, needle valve
SV#-#		Switch valve: first number is physical valve on system, second number is the port number on the valve
FC#, FLOWTRANS		Flow controller/transducer
HV#		Hand valve
MS#, P#, PTRANS D		Mass spectrometer sample port, pressure transducer port, pressure transducer
PUMP		Vacuum pump
O2TANK		Oxygen product tank

5.5.2 PSA Instrumentation, Process Control, and Data Collection

There are three types of valves used in the system: hand valves, pneumatic valves, and switch valves. The hand and switch valves direct flow into the system manually. The pneumatic valves are switched on/off by solenoid coils that are either controlled manually or by an EZPLC programmable logic controller (PLC). The PLC provides automated control of the pneumatic valves through a programmed repeated sequence of events that open and close valves at specific intervals to create a cyclic PSA process. It is located on a controller switch board that contains sixteen manual switches. The switch position determines the controller switch board mode. The up position delegates control to the controller, the down position switches the valve on, and the middle position turns the valve off.

Two different pressure transducers placed at two separate points in the process collect pressure data. The first is an Omega Dyne transducer (PTRANS D on Figure 5.7), which has a very small dead volume (i.e. flush membrane transducer) and is used primarily to determine the column pressure. The other pressure transducer is a MKS Baratron Type 722A absolute pressure transducer that is connected to a switch valve (not pictured in the figures). The switch valve has seven ports and is connected to six different points in the process (P1-P6 on Figures 5.6 and 5.7) with one port left open to measure the atmospheric pressure. This provides flexibility to check pressure at different points in the apparatus. However, this pressure transducer has a significant amount of dead volume and is normally only used on the product end of the process as to not impose extra dead volume to the columns. Pressure is controlled by back pressure

controllers (BPC) placed at various points in the process. BPC1 was used to control the adsorption pressure and BPC4 was used to control the desorption pressure.

Flow rate in the system was measured by three MKS flow meters located at three separate points in the process. One is on the feed line (FC1 on Figure 5.6), another on the purge line (FC2 on Figure 5.7), and a third on the exit manifold (FC4 on Figure 5.5). There is an additional Omega FDMA-1600A Gas Flow Meter (FLOWTRNS on Figure 5.7) used to measure mass flow rate, pressure, and temperature for the equalization flow exclusively. Due to slow response time, all flow controllers were left open and used only as flow meters. Inlet flow was controlled through a needle valve after FC1. A needle valve (NEEDLVAL on Figure 5.7) was placed before FC2 to control purge flow into the columns.

Exit flow composition is measured by an AMI (Advanced Micro Instruments) Oxygen Analyzer (O2ANALYZ on Figure 5.5) located on the product end of the process within the exit manifold. There are also ports (MS1, MS2, MS3, MS6) at both ends of each column for capturing a small amount of gas to analyze in a mass spectrometer. These ports were only used if the mass spectrometer was required for fine tuning of a process.

Data collection from pressure transducers, flow controllers, and the oxygen analyzer was done with a National Instruments 7025E data acquisition system. The data was then displayed on a computer using Lab Windows software. The software was also used to record the data into a comma-separated-value file for further analysis.

5.5.3 *System Design*

Gas into the system can be supplied to either the feed side or product side of the system through a switch valve (SV2-5 or SV2-3 on Figure 5.6). Four types of gases are connected to a separate switch valve (not shown on figures) which controls the type of feed gas supplied to the system. The gas options are nitrogen, oxygen, helium, and dry air, which were all stored in compressed gas cylinders. A vacuum pump (Thomas WOB-L piston pump, model # 817CA22) was connected to the product end to allow for vacuum pressure in the columns during the purge/blowdown step. It was connected to a switch valve (SV1) that takes the pump offline if it was not used in the process. An industrial back pressure controller (BPC4) with pressure control above and below atmospheric pressure is located upstream of the pump and is responsible for controlling the purge/blowdown pressure. A product tank is connected on the product end of the system if product collection is needed for cycles involving product pressurization. Two hand valves (HV1 and HV2) control whether flow enters or bypasses the tank during the process. The pneumatic valves (PV1-16) that control the flow in and out of the adsorption columns are housed together in four valve blocks on both sides of each column.

On the feed side of the system (Figure 5.6) during a PSA process, feed gas enters during the feed/production step through SV2-5. It then flows through the line labeled Feed 1 and Feed 2 to PV8 and PV16 which lead to the adsorption columns. During the blowdown and purge steps, flow travels from the columns through PV6 and PV14 into the lines labeled Blow1 and Blow2, which lead to the vacuum pump and exit D. PV7 and PV15 were not used for this study and hence the lines leading to them were not displayed

in order to simplify the diagram (they are only used if a rinse step is included in the PSA cycle). Pressure on the feed side of the process is measured primarily at P6, which provided the pressure during the blowdown and purge steps. P1 and P2 are not advised to be used for an extended period of time because of the dead volume induced on the columns as was discussed earlier.

The product side of the system (Figure 5.7) is more complex. During normal operation, product flowed through a combination of PV1 and PV9 if the product tank was bypassed during process operation. PV3 and PV11 allow for purge flow into the columns. As previously mentioned, the needle valve located before FC2 controlled the flow to PV3 and PV11, while FC2 was only used to measure the flow rate to the columns. PV4 and PV12 were only used for processes with a pressure equalization step. BPC3 is located on this line connecting these valves, but remained closed during the entirety of the experiments. Pressure on the product side was measured in two places, immediately before column 2 with PTransd, or at P3.

The middle manifold section of the system is represented in Figure 5.5 and is where gas was analyzed prior to exiting the system. The manifold inlets correspond with the exit locations located in Figure 5.6 and 5.7. Gas entered the manifold either through exit A (product flow) from the product side or exit D (waste flow) from the feed side. Gas can enter through exit B and C, but for this study, only exit A and exit D were used. The manifold consists of four hand valves that direct the flow out of the system either through FC4 and the oxygen analyzer, or directly to the vent. The function of this manifold was for the calculation of a material balance for the process. It provided measurement of the flow rate and oxygen concentration out of the system before the

gases were vented to the atmosphere. The manifold had the flexibility to either allow one of the streams to be analyzed separately while the other was directed straight to the atmosphere, or allow both product and waste streams to be analyzed together.

5.5.4 *Material Balances*

Material balances are important for PSA processes to validate process performance. A general balance for any system with no chemical reaction is represented as:

$$\text{Input} - \text{Output} = \text{Accumulation} \quad (5.5)$$

To calculate material balances, the flow rate and composition of the entrance and exit streams were measured. The instantaneous molar flow rate, F , at different points in the process is useful for plotting a flow rate versus time chart. This visual representation of the data is useful for real time analysis and for determining CSS. However, for a process that involves constantly changing flow rates, a steady flow in and out of the process rarely occurs. When there is an absence of steady flow, material balances are conducted using a time averaged molar flow rate, \bar{F} , which for each flow meter was calculated as:

$$\bar{F} = \frac{\int_0^t F dt}{t} \quad (5.6)$$

where t is the time interval over which the average is taken. Using a multiple of cycle time for the time interval provides a better flow average. Material balance calculations are based on the amount of gas into and out of the process on a per cycle basis. The

amount of gas used for each step in the cycle was calculated by multiplying the average flow rate with the cycle time, expressed as:

$$\Delta N^{step} = \bar{F} * t_{ct} \quad (5.7)$$

where ΔN^{step} is the amount of gas used/produced during a specific step in the cycle and t_{ct} is the cycle time. Calculating the amount of gas per step in a cycle is a convenient way to conduct a material balance to validate process performance.

For a material balance on a PSA process, the input is the amount of gas in the feed stream, while the exit streams consist of the product stream and exit streams of the purge and blowdown step. For this study, the streams from the exit of the purge and blowdown steps are measured with the same flow meter, so this stream is collectively referred to as the waste stream. Thus the overall material balance for the cycle is calculated as:

$$\Delta N^F - \Delta N^P - \Delta N^W = \epsilon \quad (5.8)$$

Where ϵ is the material balance error, N^F is the amount of feed gas used, N^P is the amount of product gas produced, and N^W is the amount of waste gas generated, all on a per cycle basis. The individual component balances can then be solved by equations 5.9 and 5.10:

$$N^F y_{O_2}^F - N^P y_{O_2}^P - N^W y_{O_2}^W = \epsilon_{O_2} \quad (5.9)$$

$$N^F y_{N_2}^F - N^P y_{N_2}^P - N^W y_{N_2}^W = \epsilon_{N_2} \quad (5.10)$$

where y_i^F , y_i^P , and y_i^W are the mole fractions of either nitrogen or oxygen in the feed, product, and waste streams respectively. At CSS, values of ϵ must be zero; however for

experimental work this almost never occurs due to uncertainty in measurement and data collection. Nevertheless, it is important to minimize the amount of error and close material balances as closely as possible to validate process calculations. All material balances were closed within 5% for the data included in this study.

5.5.5 *Design Parameters*

When designing a cycle for a PSA process, several parameters are set based on the product purity desired and allowable power consumption for the process. They include purge to feed ratio, pressure ratio, and feed stream velocity (cycle time).

Product purity is the amount of oxygen in the product stream divided by the sum of all the components in the product stream. It can be represented as:

$$\% \text{ Oxygen Purity} = \frac{N_{O_2}}{\sum_{i=1}^j N_i} * 100 \quad (5.11)$$

where N is number of moles and j is the number of components in the product. For a PSA process, it is useful to express oxygen purity as a concentration averaged over both flow and time because the concentration exiting the process varies with both. This involves dividing a time average of the oxygen flow rate by a time average of the total flow rate. This may be represented as:

$$\text{Avg. \% Oxygen Purity} = \frac{\int_0^t F y_{O_2} dt}{\int_0^t F dt} * 100 \quad (5.12)$$

The purge/feed ratio controls product purity and the amount of product the process generates. The purge/feed ratio may be represented as:

$$\frac{\text{Moles } O_2 \text{ (Purge Step)}}{\text{Moles } O_2 \text{ (Feed Step)}} = \frac{N^U y_{O_2}^U}{N^F y_{O_2}^F} \quad (5.13)$$

It should be noted that in this study, the “Feed Step” is the combination of the feed pressurization and production steps. A higher P/F ratio means a greater amount of product gas is used in column regeneration, which further pushes back the MTZ towards the feed end of the columns. The minimum P/F ratio is the ratio that gives the desired product purity, but a further decrease in the ratio causes undesired product purity. In order to ensure the desired product purity is maintained, it is not advisable to operate at the minimum P/F ratio, but rather at a ratio slightly higher than the minimum.

Pressure ratio is set based on the power allowances for the process. It is defined as:

$$\text{Pressure ratio} = \frac{P_{High}}{P_{Low}} \quad (5.14)$$

For a PSA process, the blowdown/purge step occurs at atmospheric pressure and a pump is required to pressurize the columns to the desired adsorption pressure during the feed/production steps. For a VSA and combined PVSA processes, the blowdown/purge step occurs at vacuum pressure and the adsorption pressure is either atmospheric pressure for VSA cycles, or some pressure above atmospheric for PVSA cycles. Regardless of cycle type, increasing pressure ratio leads to higher recovery at the cost of additional power consumption. However, the gain in recovery is diminishing as pressure ratio increases; hence pressure ratio is normally chosen near the point where the gain in recovery no longer justifies the required power increase.

The last design parameter is cycle time, which was controlled by the individual step times set by the PLC. These step times may be changed, however, it was required that the combined time of the purge and blowdown steps equal the combined time of the feed pressurization and production steps.

5.5.6 Performance Parameters

Process performance is primarily evaluated through two different performance parameters. Recovery is the amount of desired component fed into the system that is available as product. In essence, it is related to the energy efficiency of a process. For air separation, it can be calculated based on the product stream or the waste stream. If it is based on the product stream, it is calculated from equation 5.15 using the amount of gas per cycle of the product and feed streams.

$$\% Recovery = \frac{\text{moles } O_2 \text{ (product)}}{\text{moles } O_2 \text{ (Feed)}} * 100 = \frac{N^P y_{O_2}^P}{N^F y_{O_2}^F} * 100 \quad (5.15)$$

For a cycle at CSS, recovery is inversely related to purity. An increase in product purity decreases recovery since a higher purity requires more purge gas, which leaves less gas available as product. Recovery is dependent on separation efficiency just like purity. Hence, it is possible to increase recovery with a more selective zeolite or inclusion of an additional step like pressure equalization that increases the regeneration efficiency.

The other performance parameter is BSF which is a measure of adsorbent utilization and process productivity, often expressed as:

$$BSF = \frac{\text{adsorbent mass}(lbs)}{\text{oxygen production}(\frac{tons}{day})} \quad (5.16)$$

BSF is related to column length, feed flow rate, and cycle time. It corresponds to the system size and hence the process capital costs. Adsorption rate also plays a significant role in the BSF as a faster adsorption rate allows for smaller columns, shorter cycle times, and higher product flow rates.

Another parameter useful in evaluating a PSA process is working capacity, which represents the amount of adsorbate that adsorbs/desorbs per cycle. This capacity is found from the difference in the amount of gas at the end of the feed and purge step, which corresponds to the “cleanest” and “dirtiest” conditions of the solid adsorbent. Figure 5.8 visually demonstrates what working capacity represents on an isotherm plot. At the end of the feed step, the column temperature has risen (since adsorption is exothermic), which changes the isotherm that determines adsorption equilibrium. Conversely, at the end of the purge step, temperature in the column has decreased (since desorption is endothermic), which again changes the isotherm that determines adsorption equilibrium. While this is a useful metric, it is very difficult to measure zeolite temperature in the columns to see this transpiring. That is why an average temperature isotherm is generated to estimate the working capacity. One of the advantages of process simulators is that they are able to calculate working capacity directly since they can create an adsorption profile across the column.

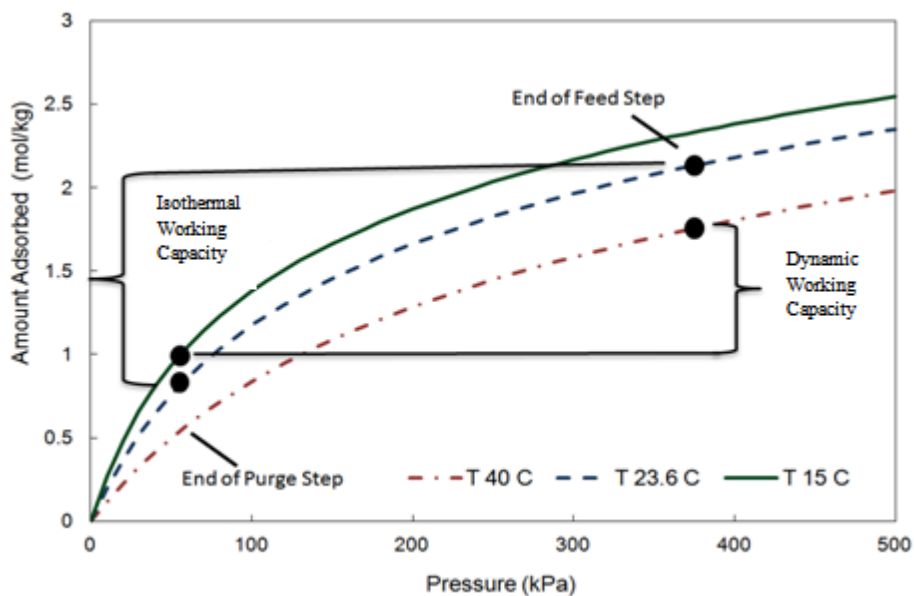


Figure 5.8. Comparison of isothermal working capacity and dynamic working capacity in a PSA process

5.5.7 Pressure Drop Study

The first PSA experimental study was conducted to better understand how pressure drop across the column affects process performance. For this study, column pressure drop was manipulated by changing both the total flow rate and column diameter. Column length was chosen in the range of typical small scale processes designed for air separation. Short, wide columns with a small, but measurable pressure drop under rapid cycling conditions were designed for the first set of experiments in this study. Longer columns with the same volume, but half the cross sectional area were designed for the next set of experiments. The length was adjusted to maintain the same amount of zeolite as the first column set. With an equivalent amount of adsorbing solid, a comparison was possible between cycles operating with similar cycle times and flow rates, but at different

velocities, hence changing the amount of column pressure drop. Further column details are provided in Table 5.4. The cycle type was a traditional feed pressurization cycle with an additional product end equalization step. The cycle steps included: 1) feed pressurization 2) production 3) co-equalization 4) blowdown 5) purge 6) counter-equalization. For Tables 5.5 and 5.6, the time of steps 1 and 2 are combined and called the “Feed press./Production” step. The switch from pressurization to production (traditional feed step) is automatically controlled by a set back pressure controller.

PSA experiments were designed to study the effect of cycle time and column pressure drop on process performance. To accomplish this, all other process parameters (e.g. pressure ratio, purge/feed ratio) were held constant as cycle time was decreased. Experimental conditions for each cycle are detailed in Tables 5.5 and 5.6. It should be noted the synthetic air used in the experiments does not contain argon, water, or carbon dioxide, making pure oxygen product possible. In comparison, the maximum attainable oxygen purity of an ambient air fed system is around 96% since LiLSX zeolites cannot separate oxygen and argon. With synthetic air, an average oxygen purity of 96% was chosen as the purity requirement because it approximately corresponds to an oxygen purity of 92-93% with ambient air, commonly used for personal oxygen concentrators.. The P/F ratio was selected based on these purity requirements. Equalization times were chosen by pressure measurements on the two columns. Overall and individual material balances for a cycle were closed within 5%. All data was taken after CSS. CSS was assumed when the column pressure at the end of each step, inlet/exit flowrates, and oxygen purity varied less than 1% for 15-20 cycles. The pressure ratios were selected in the range of a typical small scale air separation process. The cited pressure ratios

correspond to feed end measurements. The pressure ratio on the product end of the column is lower when pressure drop is significant. The superficial production step velocities cited in Table 5.5 and 5.6 are at the production step pressure. Cycle times were decreased until the apparatus could no longer maintain the desired pressure ratio at the feed end of the process (combination of flow, valve CV, and pressure limitations).

Table 5.4 Experimental column specifications for pressure drop study

	Short columns	Long columns
Column diameter (cm)	1.09	0.77
Column length (cm)	9.8	19.6
Amount of adsorbent per column (g)	5.7	5.7

Table 5.5 Cycle specifications for short column cycles in pressure drop study

	Production step superficial velocity (cm/s)	Feed Press./Production (s)	Blowdown (s)	Purge (s)	Eq. (s)	Total cycle time (s)
Cycle 1	7.5	6.75	4.75	2	0.5	14.5
Cycle 2	10.9	4.3	3.3	1	0.5	9.6
Cycle 3	15.8	2.9	1.9	1	0.5	6.8
Cycle 4	28.8	1.4	1.1	0.3	0.5	3.8

Pressure ratio 4.5, P/F ratio 0.4, product purity: 96% oxygen , production step pressure ~195 kPa, synthetic air

Table 5.6 Cycle specifications for long column cycles in pressure drop study

	Production step superficial velocity (cm/s)	Feed Press./Production (s)	Blowdown (s)	Purge (s)	Eq. (s)	Total cycle time (s)
Cycle 5	11.6	7.2	5	2.2	0.3	15
Cycle 6	16.6	4.7	3.5	1.2	0.3	10
Cycle 7	22.9	3.2	2.2	1	0.3	7
Cycle 8	39.7	1.7	1	0.7	0.3	4
Cycles 5-8: Pressure ratio 2.5, P/F ratio 0.6, product purity: 96% oxygen , production step pressure ~195 kPa, synthetic air						
Cycle 9	20.7	4.5	3.5	1	0.5	10
Cycle 10	29.8	3	2	1	0.5	7
Cycle 11	48.1	1.5	1	0.5	0.5	4
Cycle 12	52.6	1.3	1	0.3	0.5	3.6
Cycles 9-12: Pressure ratio 4.5, P/F ratio 0.4, product purity: 96% oxygen , production step pressure ~195 kPa, synthetic air						

5.5.8 Minimum BSF Study

The next experimental PSA study was conducted to determine if a minimum BSF occurs in the system. The main difference between these experiments and the pressure drop study is that the process was simplified to a 4-step cycle in order to avoid the complications of an equalization step on process performance. While a significant advantage is gained through an equalization step, it adds additional uncertainty into the analysis since it is difficult to measure. Considering the goal of this study was measuring and explaining the existence of a minimum BSF, not maximizing performance, an equalization step was not necessary. The cycle steps include: 1) feed pressurization 2) production 3) counter-current blowdown 4) counter-current purge.

Cyclic steady state (CSS) was achieved over a range of cycle times permitted by our system. Process parameters such as product purity, purge/feed ratio, and pressure ratio were kept constant at each cycle time. The experimental procedure was exactly the same as the pressure drop study and the same product purity requirement was used. The column dimensions used in this study were very similar to the pressure drop study (Table 5.7). Cycle details are further shown in Tables 5.8-5.12.

Table 5.7 Experimental column specifications for minimum BSF study

	Short columns	Long columns
Column diameter (cm)	1.09	0.77
Column length (cm)	10.2	19.6
Amount of adsorbent per column (g)	5.3	5.7

Table 5.8 Cycle specifications for long column cycles with pressure ratio 3.5 in minimum BSF study.

	Production step superficial velocity (cm/s)	Feed Press./Production (s)	Blowdown (s)	Purge (s)	Total cycle time (s)
Cycle 1	45.1	3	2.5	0.5	6
Cycle 2	69.8	1.95	1.62	0.33	3.9
Cycle 3	81.1	1.65	1.35	0.3	3.3
Cycle 4	82.4	1.6	1.3	0.3	3.2
Cycle 5	44.0	3	2.5	0.5	6
Cycle 6	62.6	2.1	1.75	0.35	4.2
Cycle 7	78.4	1.68	1.4	0.28	3.36
Cycle 8	84.8	1.56	1.3	0.26	3.12
Cycle 9	50.1	2.64	2.2	0.44	5.28

P/F ratio 0.45, product purity: 96% oxygen , production step pressure ~195 kPa, synthetic air

Table 5.9 Cycle specifications for long column cycles with pressure ratio 3 in minimum BSF study

	Production step superficial velocity (cm/s)	Feed Press./Production (s)	Blowdown (s)	Purge (s)	Total cycle time (s)
Cycle 10	39.7	3.1	2.5	0.6	6.2
Cycle 11	80.4	1.55	1.25	0.3	3.1
Cycle 12	93.1	1.36	1.1	0.26	2.72
Cycle 13	85.6	1.46	1.18	0.28	2.92
Cycle 14	50.0	2.45	2	0.45	4.9
Cycle 15	63.0	1.96	1.6	0.36	3.92

P/F ratio 0.47, product purity: 96% oxygen , production step pressure ~195 kPa, synthetic air

Table 5.10 Cycle specifications for long column cycles with pressure ratio 2.5 in minimum BSF study

	Production step superficial velocity (cm/s)	Feed Press./Production (s)	Blowdown (s)	Purge (s)	Total cycle time (s)
Cycle 16	34.5	3.2	2.5	0.7	6.4
Cycle 17	42.1	2.65	2	0.65	5.3
Cycle 18	70.3	1.6	1.25	0.35	3.2
Cycle 19	89.4	1.3	1	0.3	2.6
Cycle 20	78.8	1.45	1.1	0.35	2.9
Cycle 21	89.5	1.3	1	0.3	2.6
Cycle 22	48.9	2.2	1.75	0.45	4.4
Cycle 23	58.0	1.9	1.5	0.4	3.8

P/F ratio 0.5, product purity: 96% oxygen , production step pressure ~195 kPa, synthetic air

Table 5.11 Cycle specifications for short column cycles with pressure ratio 3.5 in minimum BSF study

	Production step superficial velocity (cm/s)	Feed Press./Production (s)	Blowdown (s)	Purge (s)	Total cycle time (s)
Cycle 24	22.6	3	2.5	0.5	6
Cycle 25	40.7	1.8	1.5	0.3	3.6
Cycle 26	49.3	1.55	1.25	0.3	3.1
Cycle 27	45.4	1.65	1.35	0.3	3.3
Cycle 28	28.7	2.42	2.02	0.4	4.84
Cycle 29	33.5	2.1	1.75	0.35	4.2
Cycle 30	16.4	4.2	3.5	0.7	8.4
Cycle 31	37.9	1.95	1.62	0.33	3.9
Cycle 32	42.6	1.75	1.45	0.3	3.5
Cycle 33	47.8	1.6	1.3	0.3	3.2

P/F ratio 0.45, product purity: 96% oxygen , production step pressure ~195 kPa, synthetic air

Table 5.12 Cycle specifications for short column cycles with pressure ratio 3 in minimum BSF study

	Production step superficial velocity (cm/s)	Feed Press./Production (s)	Blowdown (s)	Purge (s)	Total cycle time (s)
Cycle 34	20.0	3.2	2.6	0.6	6.4
Cycle 35	19.6	3.2	2.7	0.5	6.4
Cycle 36	36.8	1.85	1.5	0.35	3.7
Cycle 37	44.3	1.6	1.3	0.3	3.2
Cycle 38	49.5	1.47	1.2	0.27	2.94
Cycle 39	28.5	2.32	1.9	0.42	4.64
Cycle 40	14.1	4.64	3.8	0.84	9.28

P/F ratio 0.47, product purity: 96% oxygen , production step pressure ~195 kPa, synthetic air

5.6 PSA Model Framework

The primary aim of this work was experimental in nature. However, in order to better illustrate the effects of pressure drop and more accurately measure the MTZ, an in-house simulator developed by Dr. Sridhar Ungarala was used to provide further information not available from experimental data, particularly column profiles. Only a brief description of the more relevant aspects of the model is presented here, the complete model is provided in Appendix A. The model is non-isothermal and assumes axially dispersed plug flow with ideal gas behavior and negligible radial concentration and temperature gradients. Pressure drop is included through the Ergun equation.

5.6.1 Mass Balance

The column component mass balances are represented by the axially dispersed plug flow model introduced in section 3.3.1:

$$\frac{\partial C_i}{\partial t} = D_L \frac{\partial^2 C_i}{\partial z^2} - \frac{\partial}{\partial z}(u C_i) - \frac{\rho_b}{\varepsilon_b} \frac{\partial n_i}{\partial t} \quad (3.11)$$

The adsorption rate was described with a linear driving force (LDF) model described in section 3.3.1.²⁴

$$\frac{\partial n_i}{\partial t} = k_i(n_i^* - n_i) \quad (3.12)$$

The LDF model simplifies the mass transfer rate to permit faster computation time, which explains its popularity in literature. The LDF approximation should provide reasonable accuracy for the system used. Higher accuracy models exist, but their complexity increases computation time significantly, often without a substantial difference in accuracy.²⁴ The MTC, k_i , is typically approximated through literature data or breakthrough experiments by assuming the resistance to macropore diffusion in the adsorbent particle as the limiting resistance.²

5.6.2 Equilibrium Model

Adsorption equilibrium was formulated by the dual-site Langmuir (DSL) model. Mathias et al.²³ have demonstrated the accuracy of the DSL model for both pure component gases and nitrogen/oxygen mixtures using zeolite 5A. A LiLSX zeolite is similar enough to zeolite 5A to justify using the DSL model to predict mixture

equilibrium in the PSA model. For simulation studies, the parameters were used according to equation 3.8, previously described in section 3.2.3.

$$n_i^* = \frac{n_{s,1} b_i P y_i}{1 + \sum_j b_j P y_j} + \frac{n_{s,2} d_i P y_i}{1 + \sum_j d_j P y_j} \quad (3.8)$$

The DSL parameters used in the model may be found in Table 5.1.

5.6.3 Momentum Balance

Column pressure drop was modeled using the Ergun equation (equation 5.17). It has been found to provide a sufficient approximation of pressure drop in packed adsorbing columns.⁷⁶

$$-\frac{\partial P}{\partial z} = \frac{150 \mu_g (1 - \varepsilon_b)^2 u}{\varepsilon_b^3 d_p^2} + \frac{1.75 \rho_g (1 - \varepsilon_b) u^2}{\varepsilon_b^2 d_p} \quad (5.17)$$

5.6.4 Energy Balance

The model also considers three energy balances for the gas, solid particle, and column wall with natural convection to room temperature air. All parameters were estimated from well-established correlations from literature. Details are provided in Appendix A.

CHAPTER VI

RESULTS AND DISCUSSION

This chapter first presents the MTCs found from breakthrough experiments and demonstrates that axial dispersion is much more important for small particles compared to large particles. It next experimentally demonstrates how pressure drop affects small scale PSA performance with support from a brief simulation study. Finally, a minimum BSF was measured and an explanation for why it is occurring is explored.

6.1 Axial Dispersion Effects in Small Scale PSA

To demonstrate the significance of axial dispersion in columns of small particles, an experimental study was performed to measure the overall MTC as a function of gas velocity at constant pressure and temperature. The experiments were conducted according to the procedure outlined in section 5.4.2. The data is evaluated with the linear addition approximation (equation 4.1) to provide a suitable method to combine the effects of axial dispersion and particle mass transfer resistance, as computationally done for Figure 4.2. The measured breakthrough curves were also converted to MTZ length data

to determine the relevant mass transfer parameters for the particles used in this study. Finally the extracted kinetic data was used to better understand what the rate limiting mechanism is for columns packed with small LiLSX particles.

6.1.1 Experimental MTC Measurement

In Chapter 4 a case study was used to demonstrate how the overall MTC (equation 4.1) was affected by the estimation of axial dispersion effects. *Case 1* and *Case 2* estimate $k_{overall}$ using assumptions applied to large particles to determine D_L , while *Case 3* and *Case 4* used assumptions more applicable to small particles. Figure 6.1 directly overlays the results of the breakthrough study on the results of the case study in Figure 4.2 to determine the case that best describes the data. It is immediately clear the experimental MTC is not constant, but increases with Reynolds number as expected based on the predictions. It is also clear that either the *case 3* or *case 4* prediction most closely matches experimental data. These cases reflect higher axial dispersion effects through a higher estimate of D_L compared to the *case 1* or *case 2* prediction. Results from a similar study with the same particle size are also represented in Figure 6.1.³² In that study, the focus was to determine the effect of temperature and pressure on the MTC, which limits the amount of data that can be compared to this study. The higher reported MTC is a linear addition model prediction using similar correlations as the *case 2* prediction and the lower value is an experimentally measured MTC. The predicted values and experimental data are different between the two studies primarily because of the small variation in pressure (267 kPa for this study vs. 200 kPa for Wu et al.), inlet gas composition, and isotherm parameters used. However, both studies are consistent in that

the *case 2* prediction is ~ 3.6 times greater than the experimental data at a Reynolds number ~ 1.6 .

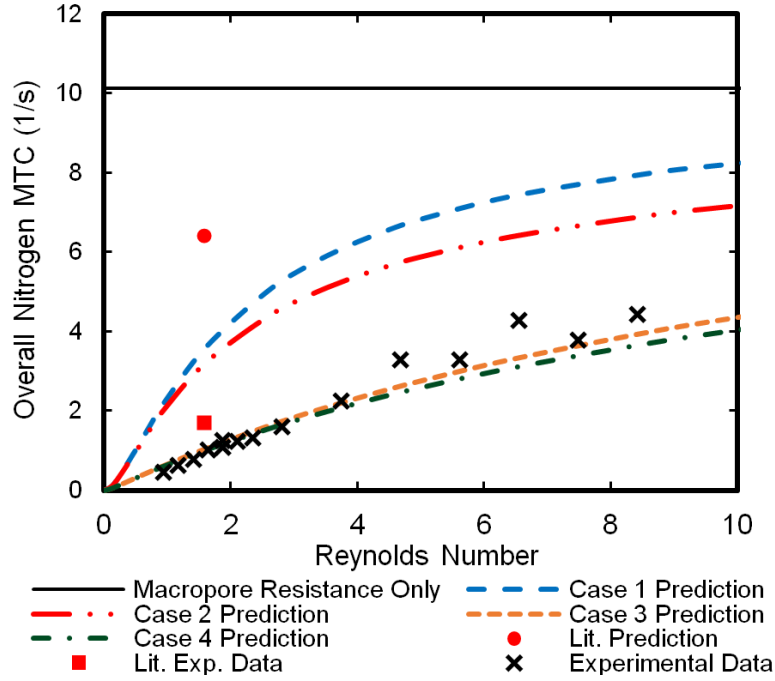


Figure 6.1. Experimental data vs. correlation predictions of the nitrogen overall MTC using $\tau_p = 3$, $\gamma_2 = 3$ and $\gamma_1 = 0.7$. Reynolds number of experimental data points is based on average velocity across MTZ. Overall pressure is 267 kPa for this study and 200 kPa for the literature study. Both studies have a particle size ~ 0.5 mm. Uncertainty for experimental data $\sim \pm 5\%$

The results of this study support the notion that axial dispersion effects contribute significantly to the overall MTC of small particles. More importantly, the results suggest the γ_2 estimate required to determine D_L in equation 3.15 is an order of magnitude higher than the value of 0.5 used for larger particles. The value of 0.5 results in a large overestimation of the MTC (*case 1* and *case 2*), which will predict a sharper MTZ than what is measured experimentally (example provided in Appendix B). The results also indicate that despite its limitations, the linear addition approximation provides a reasonable estimation for how the MTC varies with gas velocity when proper literature correlations for pore diffusion, film transfer, and axial dispersion are used.

6.1.2 Mass Transfer Parameter Estimation

The van Deemter model (equation 5.2) was next used to determine relevant mass transfer parameters useful for process simulations, namely τ_p and the γ_2 coefficient to estimate D_L . The MTZ length for each experimental run was converted to HETP as described in section 5.4.5 and plotted against the average superficial velocity across the MTZ as demonstrated in Figure 6.2. A least squared fit of the data was completed using the van Deemter model to determine values for the A , B and C constants in the model. From the constants, the γ_1 and γ_2 coefficients of equation 3.15 and τ_p of equation 4.4 were found assuming a particle size of 0.5 mm. Table 6.1 lists the calculated values along with the standard error associated with each value and a comparison to reported literature values or correlations.

Despite the limitations of this approach, the rate parameters are reasonable when compared to available literature data or correlations. The value for γ_1 used to

estimate D_L is higher than the usual value of 0.7. More data at lower gas velocities is necessary to confirm this value as demonstrated by the large standard error. However, the γ_I estimation was not of great concern in this study, as it only has a small effect on the MTC estimation and is primarily important at very low gas velocities not applicable to PSA systems. More importantly, the results confirm γ_2 is an order of magnitude higher than the often used 0.5 value. The experimental value of 3.2 is similar to what was predicted by the literature correlation in equation 4.3 for the particle size used in this study. Finally, the estimate of τ_p for nitrogen is consistent with most X-type zeolites and studies of larger LiLSX particles cited in section 4.1.4. Since these particles have been manufactured to be rate enhanced for small scale processes, it is not surprising the value is on the lower end of what has been previously reported in literature for larger particles.

Figure 6.3 uses the parameters for γ_2 and τ_p found from the van Deemter analysis to reconstruct the predictions from the earlier case study. The literature value of 0.7 was used to estimate γ_1 since the data collected did not reach a low enough velocity to achieve a reliable estimate using the van Deemter analysis. It is evident from the figure that the experimental data is still best described by either the *case 3* or *case 4* prediction. Furthermore, these predictions are now closer to the experimental values than those in the original case study.

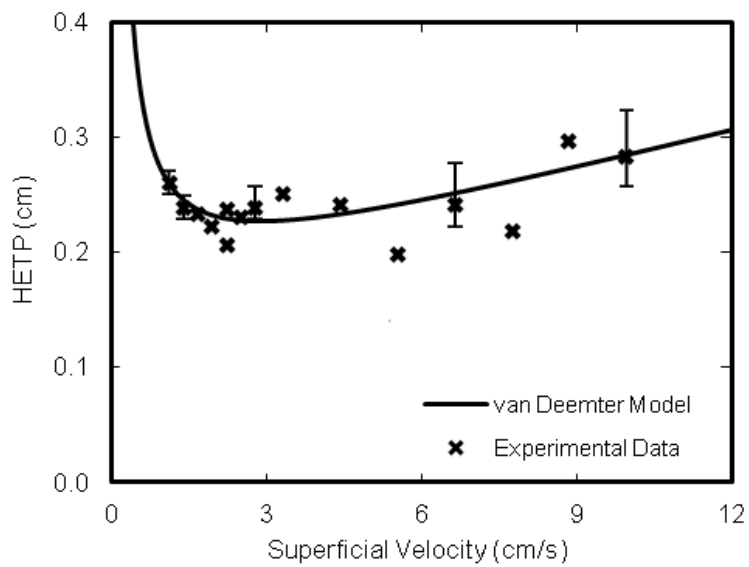


Figure 6.2. HETP vs. superficial velocity from experimental breakthrough experiments.

Superficial velocity is based on average velocity across MTZ. Superficial velocity = $u\varepsilon_b$

Table 6.1. Comparison of van Deemter constants determined from experimental data and previously cited literature values. i = nitrogen

	This study	Standard error	Literature
γ_1	2.3	± 1.1	0.7
γ_2	3.2	± 0.6	3
$\tau = D_m/D_{pi}$	1.9	± 0.5	2-4

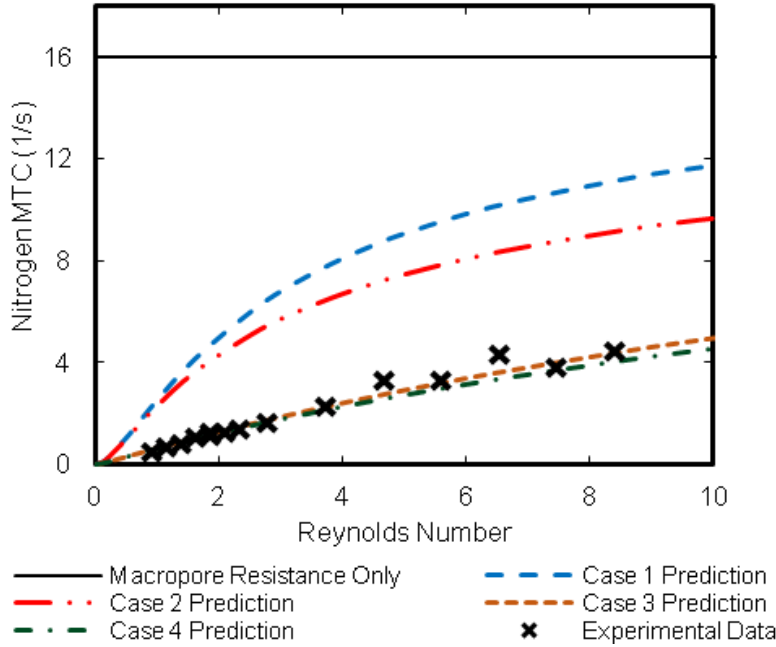


Figure 6.3 Experimental overall MTC plotted against overall nitrogen MTC predictions with $\tau_p = 1.9$, $\gamma_2 = 3.2$ and $\gamma_1 = 0.7$. Reynolds number is based on average Reynolds number across MTZ

6.1.3 Rate Limiting Contribution

Table 6.2 lists the individual contributions in equation 4.1 using the experimental parameters from Table 6.1 for γ_2 and τ_p . The table also compares the same contributions for a larger (2 mm) particle using the same τ_p and equation 4.3 to determine γ_2 . The table is designed to demonstrate how the rate limiting contribution changes for the particle size used in small scale PSA at a Reynolds number applicable to process work. The limiting contribution for the larger particle is clearly the macropore contribution as it represents 67.7% of the total resistance. For the smaller particle, the contributions from dispersion and macropore diffusion are about the same, which

demonstrates that both are important to model a PSA process accurately. For breakthrough experiments, where even lower Reynolds numbers are used, the dispersion term is predominant for the smaller particle.

Figure 6.4 further demonstrates the significance of axial dispersion effects for small particles when determining the overall MTC experimentally. In the figure, MTC predictions for the two different particle sizes are compared. It is clear the MTC predictions for the large particle do not vary significantly, which indicates the D_L estimate does not greatly impact the overall MTC estimation. Furthermore, macropore diffusion is the limiting resistance except at very low Reynolds numbers where the MTC varies significantly because of axial dispersion effects. This is not the case for small particles as the MTC is a much stronger function of Reynolds number. The switch from axial dispersion control to macropore diffusion control is much more gradual compared to larger particles.

Recognizing the mass transfer rate is significantly impacted by axial dispersion effects increases the importance of properly accounting for it in process models with small particles. Simulation accuracy may be significantly affected by using the wrong correlation to approximate D_L . A mass transfer rate controlled by axial dispersion effects additionally influences typical particle production methods aimed at reducing macropore resistance. These methods will have a more limited impact on process performance since pore diffusion is no longer the only limiting mass transfer mechanism.

Table 6.2 Comparison of equation 4.1 contributions for a nitrogen overall MTC at a Reynolds number of 20 and two different particle sizes. Constants used: $\tau_p=1.9$, $\gamma_1=0.7$ and $\gamma_2 = 3.2$ (small particle) $\gamma_2 = 0.75$ (large particle). Mass transfer resistance is proportional to $1/k_i$

Particle size (cm)	k_{disp} (1/s)	k_{macro} (1/s)	k_{film} (1/s)	$k_{overall}$ (1/s)	% of total resistance (disp)	% of total resistance (macro)	% of total resistance (film)
0.05	14.4	16.0	74.5	6.9	48	43	9
0.2	3.8	1.0	4.7	0.68	18	68	15

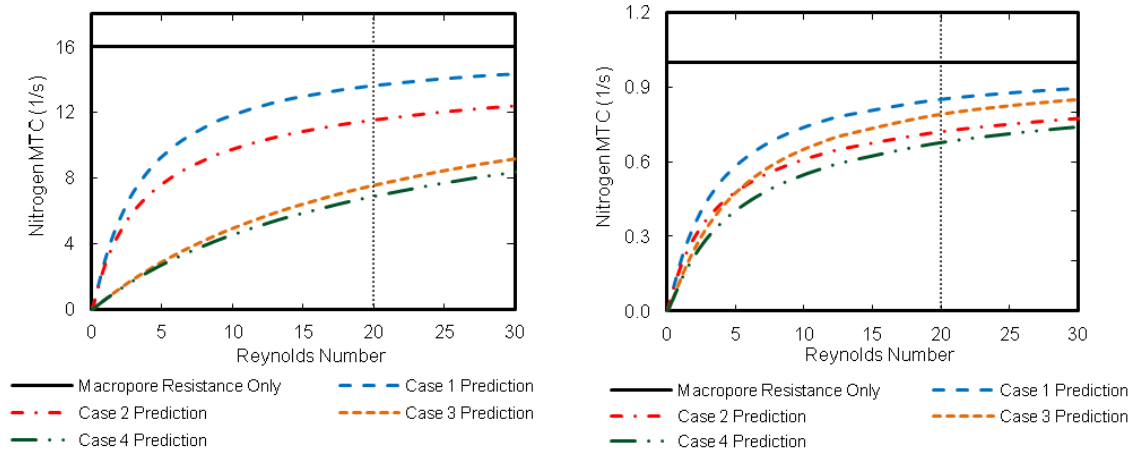


Figure 6.4. Comparison of $k_{overall}$ predictions for a) 0.5 mm particle (left) and b) 2 mm particle (right). $\tau_p = 1.9$ and $\gamma_1 = 0.7$ for all predictions for both particle sizes. $\gamma_2 = 0.5$ for both *case 1 and 2* predictions for both particle sizes. For *case 3 and 4*, $\gamma_2 = 3.2$ for 0.5 mm particle and $\gamma_2 = 0.75$ for 2 mm particle

6.1.4 Skin Resistance

Skin resistance has also been cited as a possible reason for a lower than expected MTC based on typical correlations.³² A skin, or change in density/porosity/composition of a particle near the external surface, is the consequence of some particle manufacturing methods. In particular, extrusion is a popular method for particle formation, which inevitably results in a skin on the particles. The SEM images in Figure 6.5 provide a visual example of a skin formed through extrusion in our lab using a material similar to LiLSX and a common binder. However, the current state of the art for manufacturing spherical particles on an industrial scale does not involve extrusion. Particles are rather formed by the addition of water to a mixture of zeolite and binder in a rotating drum.^{42, 77} While this does not completely eliminate the existence of a skin, it significantly reduces skin formation since there are no high stress flow of the extrusion mixture. SEM images of a spherical particle used in this study are included in Figure 6.6. No noticeable difference in density is visible at the particle surface where a skin would form. It has been suggested a skin resistance accounts for up to 65% of the total resistance for LiLSX particles.³² If skin resistance was this significant, it would be visible in an SEM image like in Figure 6.5. While an SEM image cannot eliminate the possibility of a skin resistance, it does justify considering the contribution negligible as suggested by our experimental results. A further indication skin resistance is not significant is that it would primarily affect the estimation of τ_p and would not be a function of gas velocity. However, the results of this study clearly show the MTC varies significantly with velocity and the estimation of τ_p , hence D_p , is reasonable.

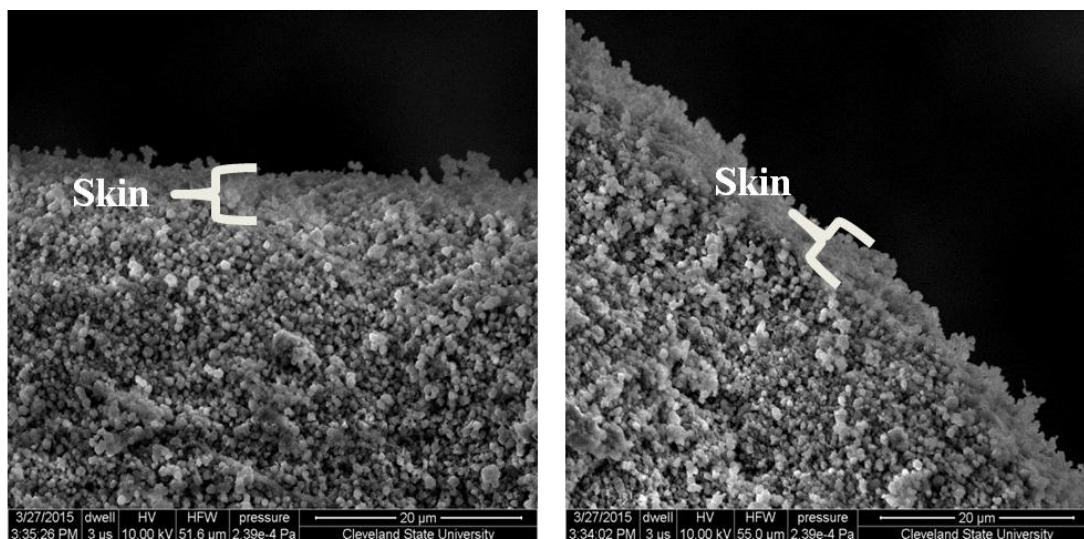


Figure 6.5 SEM images of an extruded particle edge

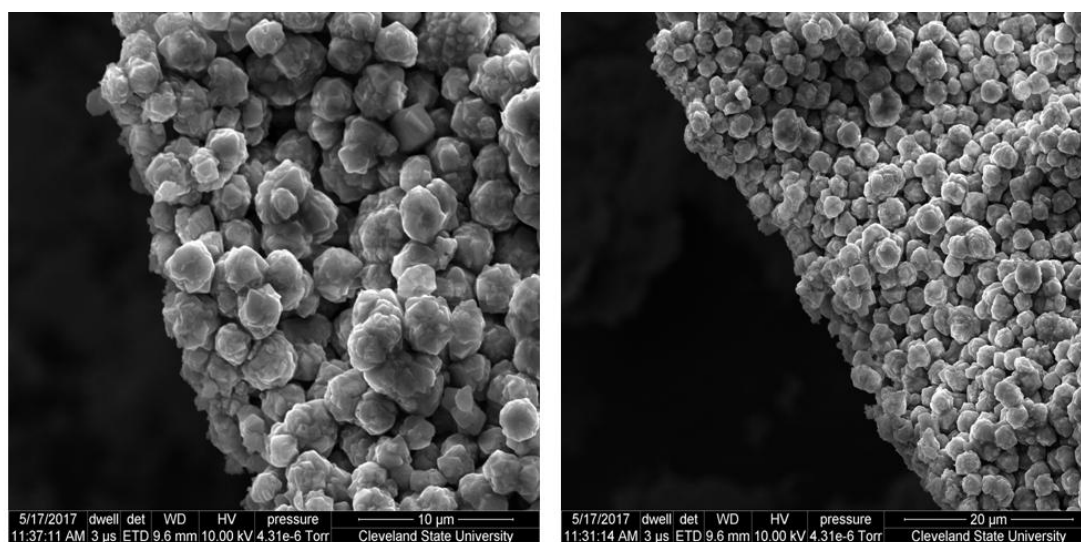


Figure 6.6 SEM images of LiLSX particle used in this study. Particle was cut in half prior to imaging

6.2. Role of Pressure Drop in Small Scale PSA

Pressure drop is a potential process limitation for small scale PSA that is not well understood. Hence, the purpose of first set of PSA experiments is to demonstrate how pressure drop affects small scale PSA performance. Pressure drop across the column was manipulated by changing column dimensions such that the cross sectional area between the columns sets varied by a factor of two while the amount of adsorbent remained constant, as outlined in section 5.5.7. This permitted a comparison between the process performance of two different sets of columns with a column pressure drop per unit column length that varied by a factor of two (or total pressure drop across the column that varied by a factor of four). The results were then compared to simulated cycles to further explain the experimental results.

6.2.1 *Experimental Results*

Pressure drop measurements for the experimental portion of this study were restricted to the constant high pressure production step due to experimental limitations. As expected, the cycles of the longer columns exhibited about twice the pressure drop per centimeter of column length as the cycles of the shorter columns at the same pressure ratio. Column pressure drop during the production step was generally consistent with Ergun equation predictions within 10%. The highest recorded pressure drop during the production step only approached 1 kPa/cm during the fastest cycle of the longer columns (pressure at column exit was 10% less than the inlet). For small scale air separation applications, the column length used in this study is similar to what is used in industry for a POC.

The expectation based on previously cited studies was column pressure drop would negatively affect the recovery and BSF of the longer column cycles more than those of the shorter columns. Figure 6.7 demonstrates this was not the case for oxygen recovery by plotting it as a function of production step superficial velocity. In Figure 6.7, two comparisons are made. One is between cycles of the short and long columns at an equivalent pressure ratio. The other is between cycles with different pressure ratios using the longer set of columns. Despite differences in pressure drop between the long and short columns, the slope of the recovery decline is comparable. If pressure drop was affecting product recovery, the decline of the recovery for the longer columns would be faster. Furthermore, the lower pressure ratio cycles for the longer columns exhibit a similar recovery decline as the higher pressure ratio cycles. Pressure drop effects increase with a higher pressure ratio. The results indicate for a pressure ratio increase from 2.5 to 4.5, the effects are minimal. Figure 6.8 compares the BSF of the long and short columns at the same pressure ratio as a function of production step velocity. The figure illustrates that cycles operating with a similar cycle time have almost the same BSF. If column pressure drop was affecting the recovery and working capacity of the process, then the BSF of cycles operating with a similar cycle time was expected to differ more.

Perhaps the most interesting aspect of these results is that they suggest for a given pressure ratio and similar cycle time, operating with a long, thin column design provides the same BSF with a higher oxygen recovery than a short, wide column design. This was not an expected result if pressure drop was playing a large role in process performance since the long, thin column design has a much greater amount of pressure drop. Clearly,

this suggests alternative factors play larger roles in determining process performance other than pressure drop.

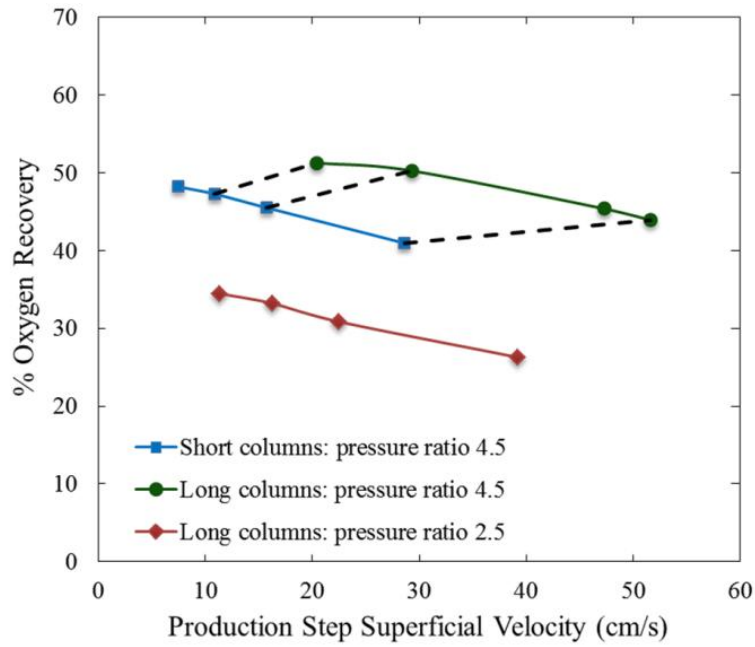


Figure 6.7 Comparison of oxygen recovery decline with increasing production step superficial velocity. Data shown involves columns with different dimensions and cycles with different pressure ratios (lines are drawn to guide the eye). Dashed lines connect cycles of similar cycle time

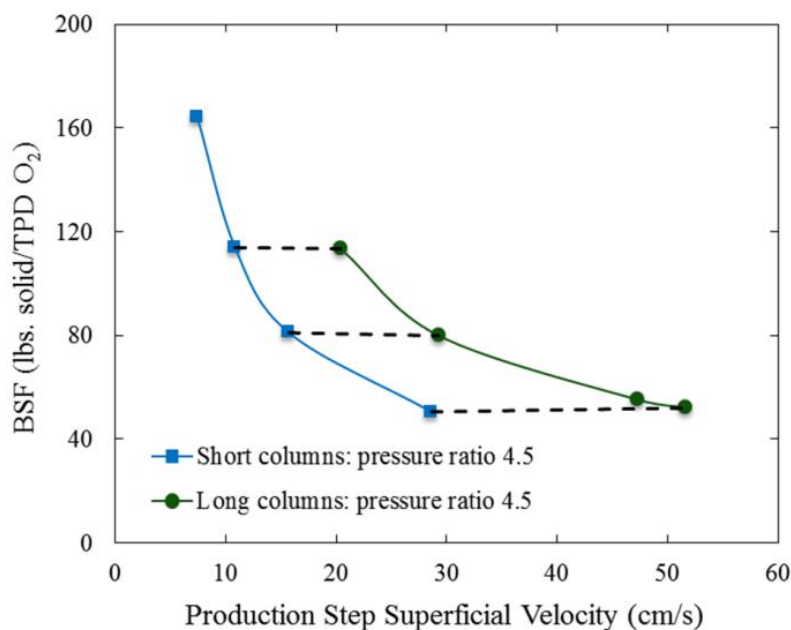


Figure 6.8 Comparison of BSF with increasing production step superficial velocity for columns of different dimensions (Lines are drawn to guide the eye). Dashed lines connect cycles of similar cycle time. (TPD = tons per day)

6.2.2 Simulation Results

The dynamic response model was briefly reviewed in section 5.6 and is fully described in the appendix. CSS was determined when the oxygen purity, recovery, and BSF were within 0.5% for at least 15 cycles. Simulated and experimental values for two cases (Cycles #3 and #10 of the pressure drop study) are summarized in Table 6.3. The simulator provides process performance parameters comparable to experimental results. Simulated concentration and loading profiles are therefore considered reasonable approximations of experimental profiles. Figure 6.9 compares the gas composition against column length at the end of the high pressure production step. The figure demonstrates the concentration profiles are nearly identical even though the longer

columns have twice the pressure drop per unit column length as the shorter columns. This indicates column pressure drop is not affecting the high pressure concentration profile. Figure 6.10 compares the concentration profiles between the two cycles at the end of the purge step. The profiles are once again nearly the same despite the higher pressure drop of the longer columns. As with the production step, column pressure drop has little impact on the low pressure concentration profile.

Table 6.3 Comparison of experimental and simulation results at similar cycle times and different column dimensions. (TPD = tons per day)

	Short columns: cycle #3		Long columns: cycle #10	
	experiment	simulation	experiment	simulation
Cycle time (s)	6.8	6.83	7	7.08
Product purity (% oxygen)	96	96.2	96	96
Oxygen recovery (%)	45.5	45.5	50.3	50.2
BSF (lbs. solid/TPD O ₂)	81	83.6	80	76.7
Production step pressure drop (kPa/cm)	0.19	0.16	0.29	0.34
Total pressure drop as % of production step pressure	0.95	0.80	2.9	3.4
Purge step pressure drop (kPa/cm)	-	0.28	-	0.54
Total pressure drop as % of purge step pressure	-	6.4	-	24.6

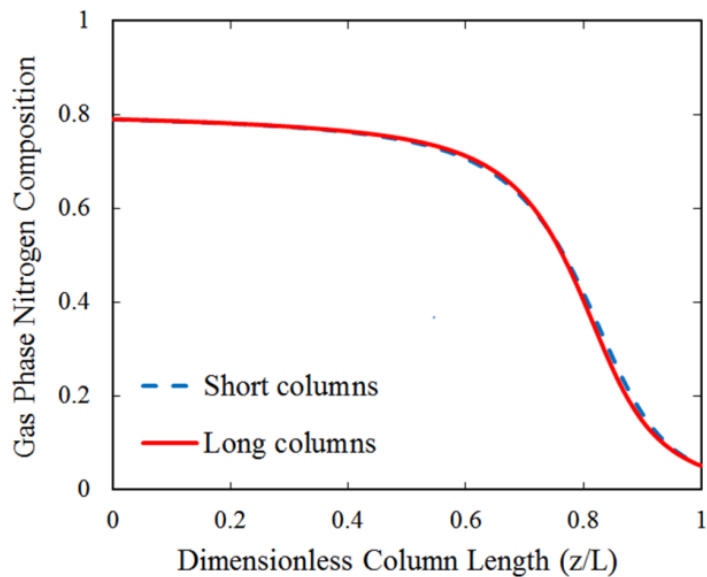


Figure 6.9 Comparison of gas phase nitrogen composition at the end of the production step for the short columns (cycle #3) and long columns (cycle #10)

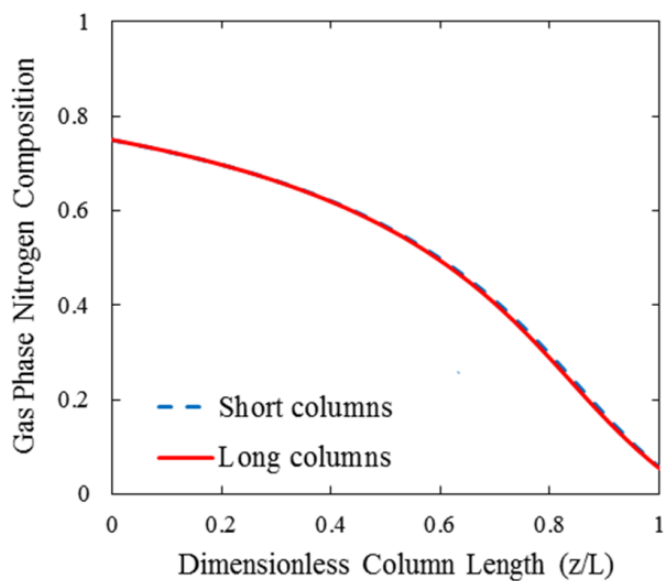


Figure 6.10 Comparison of gas phase nitrogen composition at the end of the purge step for the short columns (cycle #3) and long columns (cycle #10)

The nitrogen solid loading profiles (Figure 6.11) at the high pressure production step and low pressure purge step indicate only slight differences between the two cycles. The variation in loading at the end of the production step is primarily related to heat transfer due to the difference in column diameter. For the low pressure purge step, the difference in nitrogen loading at the feed end ($z = 0$) of the column is also adequately explained by thermal effects. However, the difference in nitrogen loading at the product end of the column is best explained by pressure drop effects since the loading of the longer columns is greater than the shorter columns in this section. The difference due to pressure drop is not significant and its impact is reduced because it affects the side of the column undergoing the least amount of nitrogen loading/unloading. The solid nitrogen working capacity was determined from the difference in solid nitrogen loading at the end of the production and purge steps. In Figure 6.11, this amounts to the difference of the area under the curves between the production and purge steps. Both columns had an average working capacity around 0.495 mol/kg. If thermal effects were not as considerable, the working capacity of the longer column would be less than the shorter columns due to pressure drop. However, this difference would be relatively small since the overall pressure drop across the column is not significant.

Since the P/F ratio was maintained between the two cycles, the amount of gas used during the purge step was nearly the same. As previously mentioned, the loading profile after the purge step does indicate pressure drop reduces the amount of nitrogen desorbed on the product end of the longer columns. A greater amount of gas would be needed to achieve a similar desorption duty as the shorter columns. However, even though the pressure drop per unit length increased by a factor of two (total pressure drop

increased by a factor of 4), the difference in the amount desorbed from the solid was only about 2% of the solid nitrogen working capacity. For columns with less pressure drop, the difference would be even more insignificant.

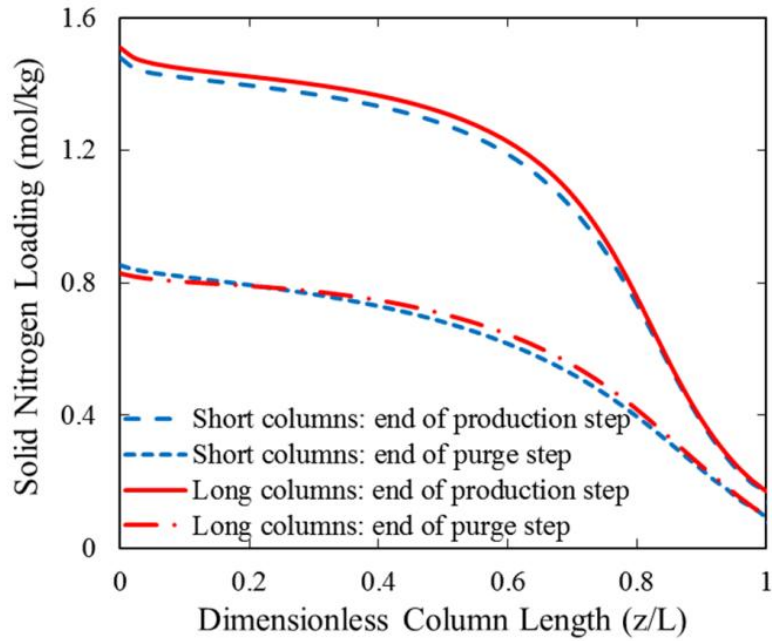


Figure 6.11 Comparison of solid nitrogen loading at the end of the production and purge steps for the short columns (cycle #3) and long columns (cycle #10)

The purpose of the next comparison was to determine the effect of increasing column pressure drop due to a higher cyclic frequency. For this comparison, the performance of cycles #3 (slower cycle time) and #4 (faster cycle time) are compared to experimental results in Table 6.4. The increase in pressure drop per unit column length is comparable to the previous cycle comparison, except in this case, the rise in pressure drop is due to an increase in cycle speed rather than a change in column diameter.

Table 6.4. Comparison of experimental and simulation results at different cycle times using short, wide columns. (TPD = tons per day)

	Slow cycle: cycle #3		Fast cycle: cycle #4	
	experiment	simulation	experiment	simulation
Cycle time (s)	6.8	6.83	3.8	3.8
Avg. product purity (% oxygen)	96	96.2	96	96.1
Oxygen recovery (%)	45.5	45.5	41.0	42.7
BSF (lbs. solid/TPD O ₂)	81	83.6	51	53.3
Production step pressure drop (kPa/cm)	0.19	0.16	0.39	0.31
Total pressure drop as % of production step pressure	0.95	0.80	2.0	1.6
Purge step pressure drop (kPa/cm)	-	0.28	-	0.45
Total pressure drop as % of purge step pressure	-	6.4	-	10.3

Figures 6.12 and 6.13 once again illustrate how the gas phase composition varies over the column length at the end of the production and purge steps. After the production step, there is a noticeable difference in the profiles as the faster cycle exhibits a greater amount of MTZ spreading. This is at least partially responsible for the reduction in recovery with increasing cycle speed. After the purge step, Figure 6.13 illustrates the concentration profiles have nearly the same shape. Although there is a noticeable vertical shift between the profiles, there is no apparent impact on the solid loading profile after the purge step as indicated by Figure 6.14. As with the previous comparison, the P/F ratio was held constant for the two cycles, thus the amount of purge gas used was again about the same.

The columns achieving nearly identical loading profiles after the purge step seems to contrast the previous simulation comparison. However, Figure 6.14 also shows less nitrogen was adsorbed at the end of the production step for the faster cycle, which means less desorption is required to achieve the same loading profile after the purge step. Thus, even though the purge step of the faster cycle is less efficient due to column pressure drop, the loading profiles after the purge step remain similar. The reduction in nitrogen loading during the production step is likely the result of a combination of mass and heat transfer resistances. At the feed end of the column where most of the adsorption/desorption occurs, the difference in working capacity is caused by a resistance to heat transfer. At the product end of the column, the difference in loading is the result of a resistance to mass transfer. In the middle of the column, it is a combination of both resistances.

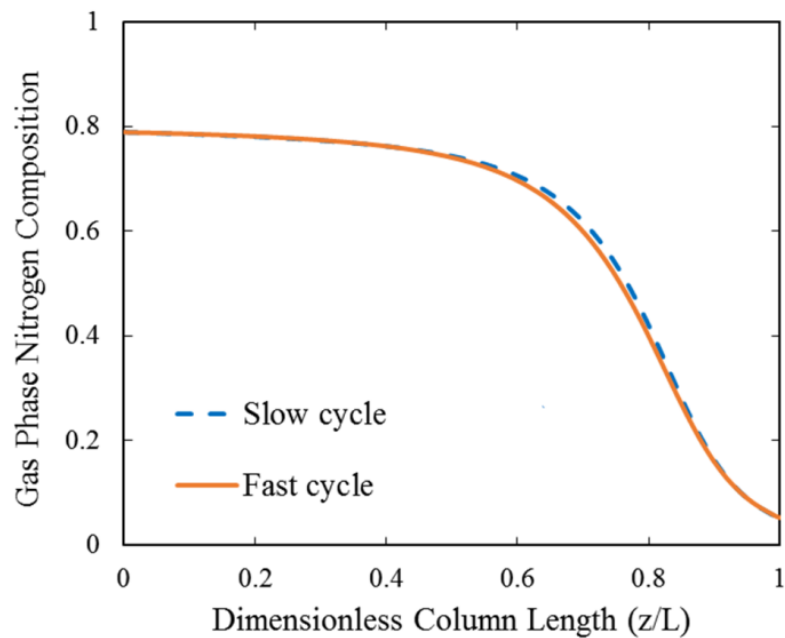


Figure 6.12 Comparison of gas phase nitrogen composition at the end of the production step for the slow cycle (cycle #3) and fast cycle (cycle #4)

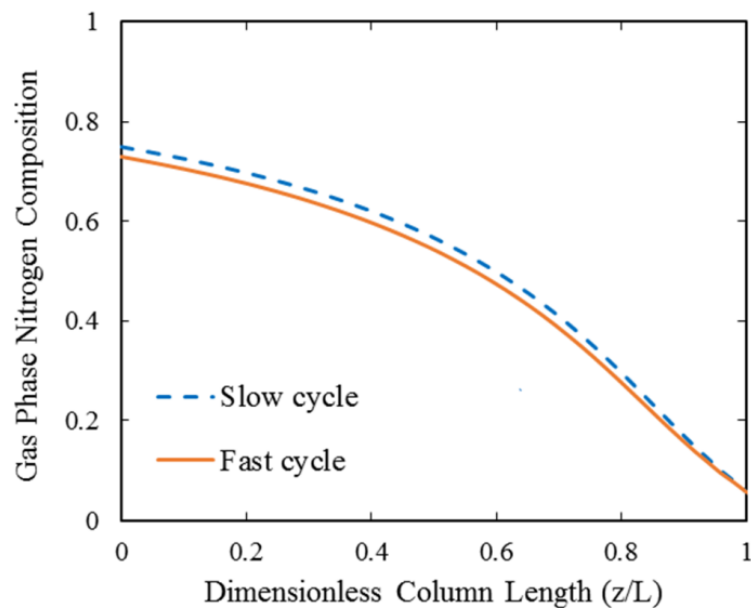


Figure 6.13 Comparison of gas phase nitrogen composition at the end of the purge step for the slow cycle (cycle #3) and fast cycle (cycle #4)

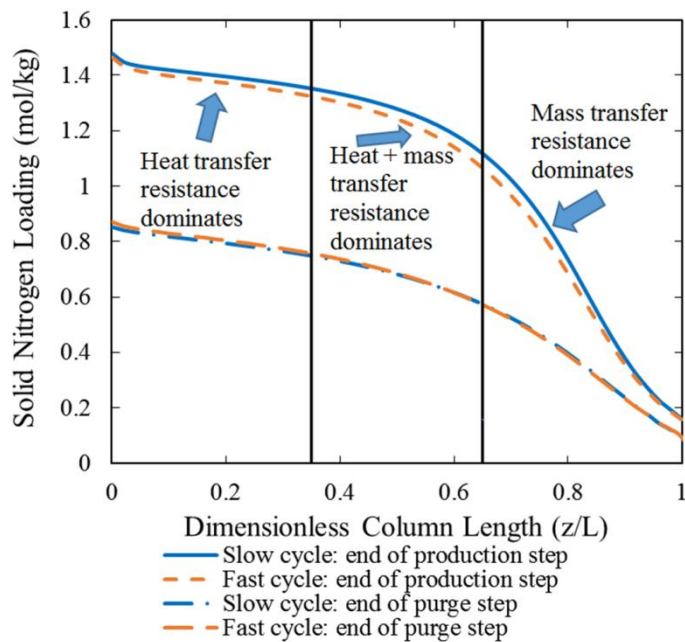


Figure 6.14 Comparison of solid nitrogen loading at the end of the production and purge steps for the slow cycle (cycle #3) and fast cycle (cycle #4)

The previous conclusion is reasonably inferred by a combination of the previous simulation comparison and Figure 6.15. The previous simulation comparison indicated column pressure drop had a negligible impact on working capacity. Since a similar increase in column pressure drop per length of column exists in this comparison, the effect of pressure drop on working capacity is considered insignificant. Mass and heat transfer resistances are the remaining primary contributors to the working capacity reduction. Figure 6.15 shows the solid temperature profile along the length of the column. At the feed end, the temperature difference reasonably accounts for a majority of the difference in nitrogen loading between the two cycles. In the middle of the column, the temperature profiles converge while the difference in nitrogen loading

between the cycles diverges. This indicates mass and heat transfer resistances both contribute to the difference in loading in this region. At the product end of the column, the solid temperature of the faster cycle is nearly the same as the slower cycle. Clearly, the difference in loading at this end of the column is primarily due to mass transfer resistances.

The simulation results therefore suggest the largest variation in the concentration and loading profiles as cycle speed increases occurs during the production step. This leads to the conclusion that for this study, mass and heat transfer resistances during the production step are critical to the recovery and BSF of the process. It also confirms the experimental results, which suggested column pressure drop was not a significant source of process performance decline as cycling frequency increases.

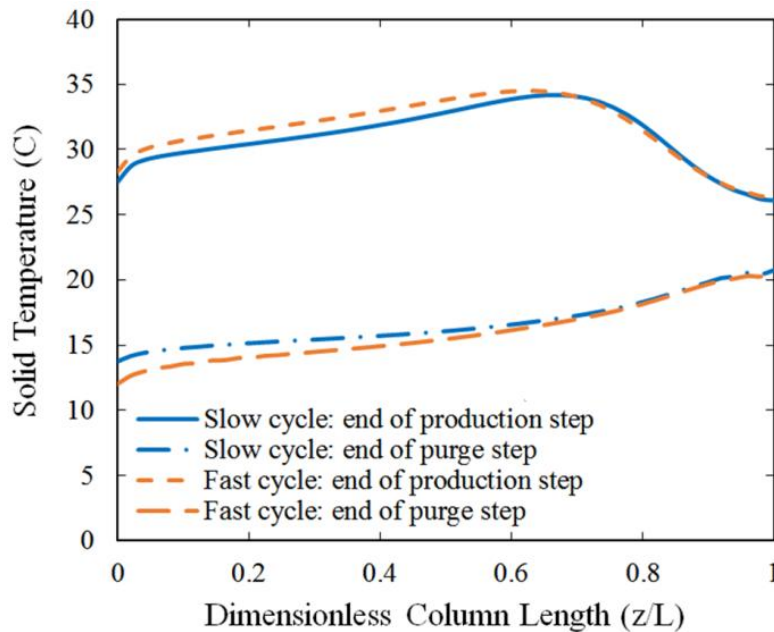


Figure 6.15. Comparison of solid temperature profiles at the end of the production and purge steps

6.3. Adsorbent Utilization Limit in Small Scale PSA

An adsorbent utilization limit (minimum BSF) represents another important limitation of small scale PSA that is not well understood, especially for a two column process. While some single column studies have indicated it exists,^{30,35,38,59} it has never been demonstrated for a dual-column process. Hence, it is valuable to determine if a minimum also occurs for a dual-column process, and more importantly what causes it. The purpose of the last set of experiments was to measure a minimum BSF for a small scale dual-column PSA process so that the cause of it may be better understood. The experimental system and column size is the same as the pressure drop study, as outlined in Chapter 5. The primary difference between the two studies is the removal of the equalization step to simplify the analysis.

6.3.1 *Measurement of a Minimum BSF*

Figure 6.16 illustrates that oxygen recovery for both sets of columns declines with faster cycling, which is consistent with the results from the pressure drop study. At each pressure ratio, the decline is linear with cycle time until ~ 3.8 seconds, where the slope of the decline increases. Figure 6.17 shows a minimum BSF around the same cycle time for each pressure ratio, which demonstrates that the cycle time of a minimum BSF is not a strong function of pressure ratio in our experimental range. Previous experimental results for single column processes are mixed on whether pressure ratio affects the cycle time a minimum BSF develops. One study showed pressure ratio affects the cycle time a minimum BSF develops. One study showed pressure ratio affects the cycle time of a minimum BSF (although no trend was found),⁷⁸ while another shows it does not.³⁸ The minimum BSF developing at the same cycle time for both column sets confirms the

pressure drop study that showed pressure drop had an insignificant impact on process performance. System limitations only permitted measurement of a minimum at two pressure ratios for the short, wide column set.

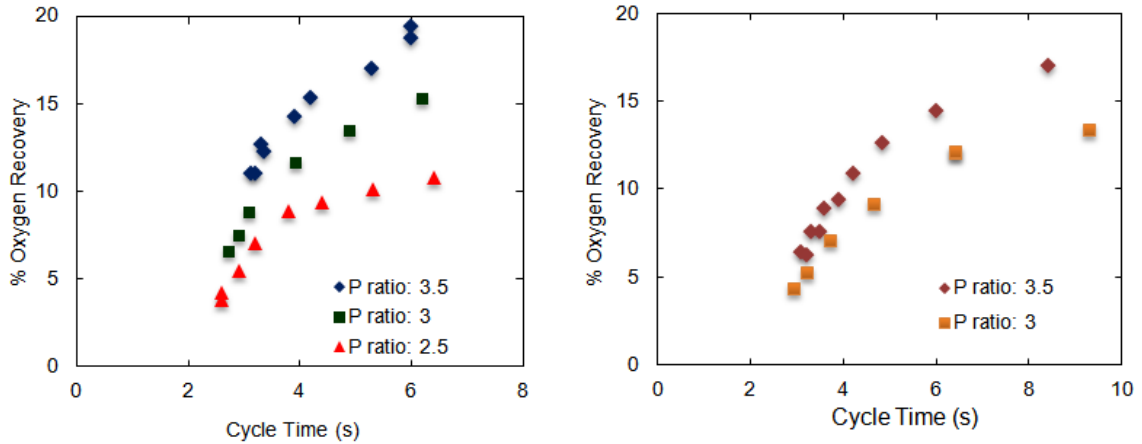


Figure 6.16 Oxygen recovery results for long, thin columns (left) and short, wide columns (right)

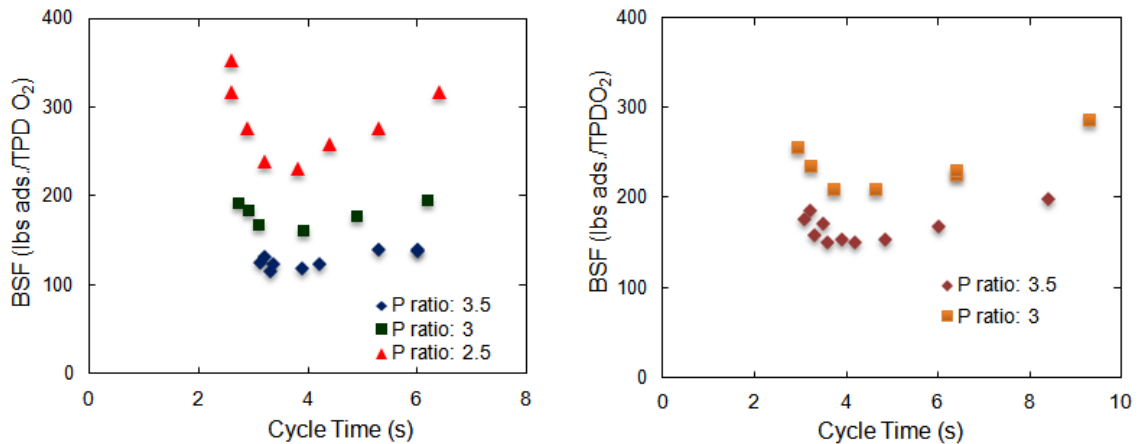


Figure 6.17 BSF results for long, thin columns (left) and short, wide columns (right)

Experimental results were next used in equation 4.5 to evaluate its usefulness in understanding the existence of a minimum BSF. To use equation 4.5, the empirical constant, k' , was found using the following assumptions: 1) Gas velocity was estimated from the conditions of the high pressure production step for each experiment 2) WC_{ideal} was estimated from isotherm data at 20 °C, 195 kPa, and a nitrogen/oxygen composition of 79/21⁵² 3) Pressure drop was estimated using the Ergun equation⁷⁶ using the velocity of the high pressure productions step 4) K was determined through the expression $K=WC_{ideal}/(P_H-P_L)$ where P_H and P_L are the high and low pressure during the PSA process respectively 5) L_{MTZ} was estimated using the van Deemter model (equation 5.2); hence, for practical PSA operation, the MTZ length is a linear function of gas velocity with the slope determined by mass transfer resistance in the particle. For columns with large particles, the eddy diffusion contribution (“A” term) is often relatively insignificant compared to the particle resistance contribution (“C” term) and is sometimes ignored. However, this term is significant for the particle size used in small scale PSA as demonstrated in section 6.1. The particle resistance contribution is primarily controlled by macropore diffusion since it represents the greatest mass transfer limitation for large X-type zeolite particles.^{2, 24} While more complex models exist to estimate MTZ spreading,^{51, 73, 74} they all have the same basic form and the van Deemter model was demonstrated earlier to provide a suitable estimation. HETP was converted to MTZ by assuming $HETP \approx HTU$ ⁷⁵ and $L_{MTZ} = NTU*HTU$. The parameters in Table 6.1 were used in the van Deemter model to determine HTU using the average velocity across the MTZ; NTU was estimated ~ 4.5 from the results of the breakthrough experiments.

k' was found for each experiment using the above assumptions and plotted against velocity in Figure 6.18. Although k' is supposed to be constant, it clearly varies linearly with velocity for both column sets. According to the regression analysis listed in Tables 6.5 and 6.6, the slope does not vary appreciably with pressure ratio; however, the y-intercept is a function of pressure ratio. The regression analysis shows excellent correlation of the data for each pressure ratio. k' varying with velocity is not surprising since L_{MTZ} is found by estimating NTU from breakthrough experiments, which operate with a completely regenerated column. Air separation via PSA operates with partial regeneration, which decreases the driving force during adsorption relative to a fully regenerated column and increases NTU. To account for this difference, k' evidently must vary with velocity. It is not clear if other factors also play a role in the variation of k' with velocity.

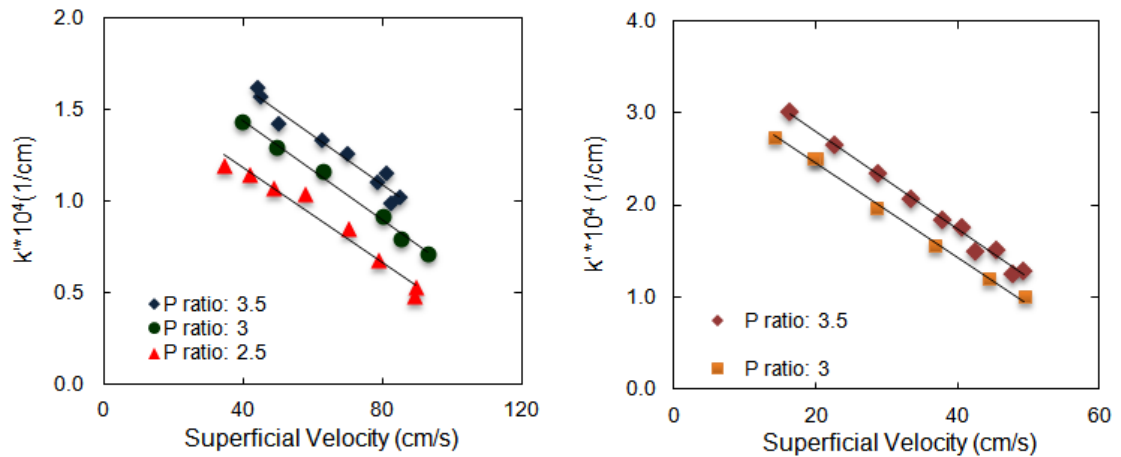


Figure 6.18 k' plotted against superficial velocity of high pressure feed step for long, thin columns (left) and short, wide columns (right). Adsorption pressure = 195 kPa, desorption

Table 6.5 Slope (m) and intercept (b) of k' vs. superficial velocity in Figure 6.18 for long columns. Std. error and R^2 are from linear regression analysis

	$m \cdot 10^6 \text{ (s/cm}^2\text{)}$	Std. error $\cdot 10^6$	$b \cdot 10^4 \text{ (1/cm)}$	Std. error $\cdot 10^4$	R^2
Pressure ratio 2.5	-1.3	0.1	1.71	0.066	0.967
Pressure ratio 3	-1.4	0.1	1.98	0.04	0.993
Pressure ratio 3.5	-1.4	0.1	2.17	0.073	0.958

Table 6.6 Slope (m) and intercept (b) of k' vs. superficial velocity in Figure 6.18 for short columns. Std. error and R^2 are from linear regression analysis

	$m \cdot 10^6 \text{ (s/cm}^2\text{)}$	Std. error $\cdot 10^6$	$b \cdot 10^4 \text{ (1/cm)}$	Std. error $\cdot 10^4$	R^2
Pressure ratio 3	-5.1	0.1	3.48	0.049	0.991
Pressure ratio 3.5	-5.3	0.2	3.87	0.066	0.996

Figure 6.19 plots BSF against the production step velocity of every experiment. At each pressure ratio, the plotted line represents the BSF from equation 4.5 using the relationship between k' and velocity from Tables 6.5 and 6.6. It is clear from Figure 6.19 that the minimum BSF shifts to a higher velocity as pressure ratio increases. This trend is more pronounced for the long, thin column set.

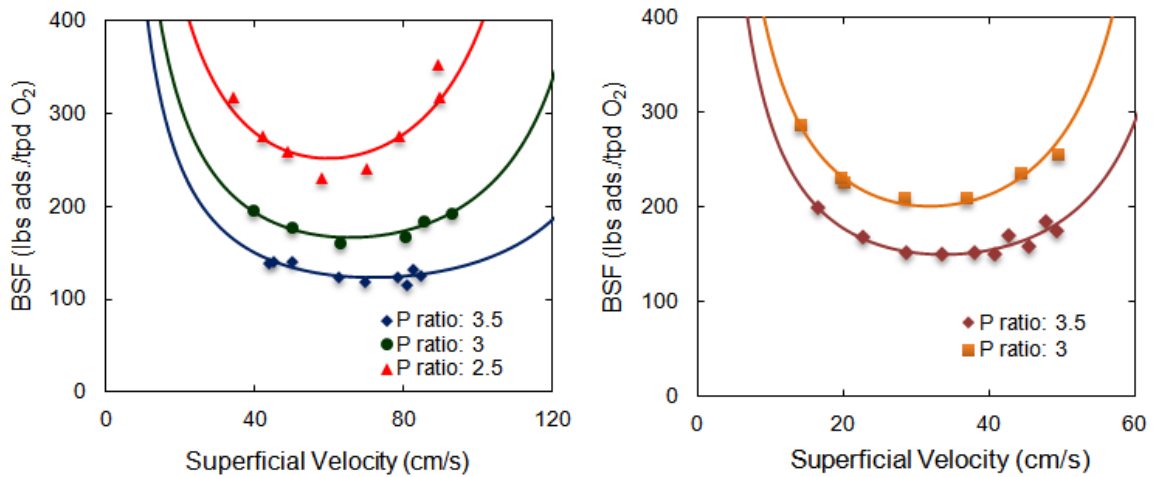


Figure 6.19 BSF plotted against superficial velocity of high pressure feed step for long columns. Ads. Pressure = 195 kPa, desorption pressure adjusted to achieve pressure ratios listed. Solid line represents equation 4.5 predictions using experimentally determined k'

6.3.2 *What Causes a Minimum BSF?*

Understanding what is causing the minimum to occur in our process would be useful for future small scale PSA design. The primary potential contributors according to equation 4.5 are pressure drop and MTZ spreading. Pressure drop was determined to only have a very negligible impact on process performance through the study in section 6.2. Figure 6.20 further confirms this using equation 4.5. The dashed line plots equation 4.5 with pressure drop = 0 and the solid line plots equation 4.5 with pressure drop predicted by the Ergun equation. There is no difference between the dashed line and solid line until a gas velocity ~ 30 cm/s where a small deviation appears. However, the minimum BSF is nearly identical in both cases, which indicates the pressure drop term in equation 4.5 only minimally affects the minimum BSF.

Since the pressure drop contribution is so small, equation 4.5 indicates that the MTZ length increasing with velocity is responsible for a minimum BSF. While mass and heat transfer limitations increase the MTZ length, not all of them are a function of velocity. Heat transfer resistances increase adsorbent temperature relative to isothermal conditions, which stretches the MTZ. However, as cycle time decreases under rapid cycling conditions, the time for heat transfer is reduced and the column approaches adiabatic operation. When this occurs, the adsorbent temperature swing becomes nearly constant. Hence, as gas velocity increases at the adiabatic limit, further MTZ spreading due to heat effects is expected to be minimal. For very short cycle times (such as those in this study), it is reasonable to assume the adiabatic limit is reached (or is very close to being reached) and heat effects do not additionally spread the MTZ with increasing velocity.

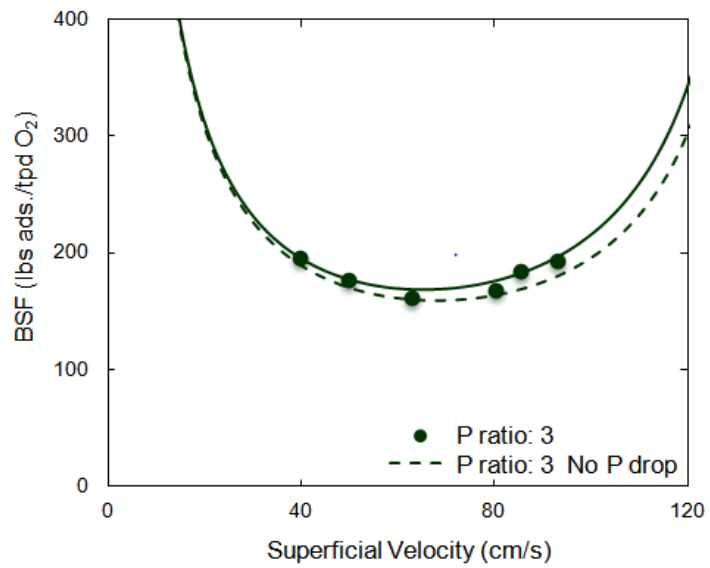


Figure 6.20 BSF plotted against superficial velocity of high pressure feed step for long columns. Ads. Pressure = 195 kPa, desorption pressure adjusted to achieve pressure ratio listed. Solid line represents equation 4.5 predictions using experimentally determined k' . Dashed line represents Equation 4.5 prediction with $\Delta P = 0$

The van Deemter model (section 5.4.5) indicates the two dominant mass transfer limitations that spread the MTZ in the range of our experiments are eddy diffusion axial dispersion effects (“A” term) and mass transfer resistance in the particle (“C” term). Axial dispersion effects due to eddy diffusion have previously been demonstrated to be significant for the particle size used in small scale processes.^{26, 28, 31} However, according to the van Deemter model, the axial dispersion contribution to MTZ spreading is constant as cycle time decreases, similar to the contribution of heat effects under adiabatic conditions. This is not the case for the “C” term in the van Deemter model, dominated by macropore diffusional resistance, whose contribution to MTZ spreading does increase with velocity. Earlier, it was demonstrated a transition from axial dispersion control to macropore diffusion control exists for small LiLSX particles as gas velocity increases. This transition occurs because the contribution to MTZ spreading from eddy diffusion axial dispersion effects are not a function of gas velocity while the contribution from macropore resistance does depend on velocity. As velocity increases (especially in the range of fast PSA experiments), the axial dispersion contribution to the MTZ becomes less important relative to the macropore diffusion contribution. Since the macropore diffusional resistance contribution to MTZ spreading is the only limitation causing additional MTZ spreading in the experimental range of this study, it is reasonable to conclude the existence of a minimum BSF is primarily due to macropore resistance.

CHAPTER VII

CONCLUSIONS

The conclusions of this dissertation are only for small scale processes with short columns (10-30 cm in length) and particles similar in size to this study (0.5 mm). Columns of much longer length or use of much smaller particles might invalidate these conclusions as this may significantly increase the effect of pressure drop at similar cycle times as this work.

7.1. On the Effects of Axial Dispersion in Small Scale PSA

While axial dispersion is known to increase with small adsorbent particles, it is largely not considered significant for columns packed with small LiLSX particles. The results of this study suggest this is no longer a good assumption as the overall mass transfer rate in the column is significantly impacted by axial dispersion effects. The implication of this observation for LiLSX particles is twofold in nature. First, the success

of typical methods to improve pore diffusion characteristics will be greatly limited since macropore diffusion is no longer the only rate limiting mechanism. The other is the estimation of axial dispersion effects in process modeling and breakthrough curve analysis is critical for accurate model predictions and mass transfer rate parameter estimations.

The results of this study further suggest measuring axial dispersion effects using breakthrough curve analysis to determine an overall MTC can provide an accurate estimation of axial dispersion effects. Literature correlations²⁶ which correctly account for the increase in axial dispersion for small particles also provide a reasonable estimation. Not using one of these methods to describe axial dispersion effects either leads to erroneous rate parameter estimation from breakthrough curves or overestimating the MTC in process simulations.

7.2. On the Role of Pressure Drop in Small Scale PSA

While considering the effect of column pressure drop on a specific step of a PSA cycle can be informative, it is difficult to determine the influence of individual steps on the overall process performance. By studying the cumulative effect of column pressure drop on process performance, it was determined its impact is minimal as cycling speed increases. The results instead suggest mass and heat transfer resistances have a much greater influence and limit operation performance before any significant impact of column pressure drop. Several contributing factors are thought to be responsible for this observation. The primary factor is the overall column pressure drop is small due to the short column length often used in small scale PSA processes designed for a POC. The

other is that the end of the column most affected by column pressure drop (product end) is the least loaded/unloaded with nitrogen, which somewhat mitigates the effect of pressure drop on the column working capacity. This study includes and goes slightly beyond the flow regime where Darcy's law is valid. Thus, these conclusions are only appropriate for this flow regime using similar size particles ($d_p \sim 0.5$ mm). This regime is often where small scale PSA processes using these particles operate. It should be noted that cycles using much smaller particles, such as those described by Galbraith et al⁷⁹ ($d_p \sim 0.15$ mm), may have high enough pressure drop to invalidate these conclusions.

Column pressure drop is sometimes cited as a concern when using small particles and small scale PSA. However, the experimental results suggest that within our experimental range, a long, thin column design achieved a similar BSF with a higher oxygen recovery than a short, wide column design. Since the long, thin column design operated with roughly double the pressure drop per unit column length, pressure drop clearly had little effect on process performance. Therefore, pressure drop concerns do not seem justified for small scale air separation processes that operate in a flow regime and with a column length and particle size similar to this study. While it should not be ignored, especially for modeling purposes, its effect on process performance is negligible compared to other more likely explanations, such as mass and heat transfer resistances.

7.3. On the Existence of a Minimum BSF

This study experimentally demonstrates a minimum BSF exists for a two column, small scale PSA process. The cycle time a minimum BSF occurred was not found to be a strong function of pressure ratio. The experimental data was further used to demonstrate the usefulness of an available literature BSF model.⁴⁴ It was found that the data was well

correlated using the model. Regression of the data was used to determine an empirical parameter that permitted the model to be used to predict process performance.

It was finally proposed that macropore diffusional resistance was primarily responsible for the existence of a minimum BSF in this dissertation as it was the only mass/heat transfer limitation spreading the MTZ as a function of velocity in the range of our experiments. While heat and axial dispersion effects are important, its contribution to MTZ spreading is not a function of gas velocity in the experimental range of this work; hence they cannot cause a minimum BSF to occur. These conclusions are likely to apply to other small scale processes with a similar column length.

7.4. Summary of Intellectual Contributions

This dissertation experimentally demonstrates for the first time the significance of axial dispersion effects for small LiLSX particles, especially for breakthrough experiments. This is important because these particles are popular for POCs. The current consensus in literature is that macropore resistance dominates the mass transfer rate, however, this study clearly demonstrates this is no longer a sufficient assumption for small particle breakthrough experiments where kinetic effects are evaluated.

Limitations of small scale PSA processes was the other focus of this dissertation. While small scale PSA processes have much in common with larger PSA processes, several key distinctions (e.g. rapid cycling and much smaller particles) make understanding process limitations difficult. One potential limitation, pressure drop, was explored further because its effects on overall process performance for small scale systems has never been experimentally demonstrated. It was found not to have a significant effect on process performance, which provides a wider design range for the

column dimensions. This is important to POC design because packaging all the components into a portable process is tricky, and greater flexibility in column dimensions is always desirable.

Another potential limitation, adsorbent utilization was also studied. A limit on adsorbent utilization (minimum BSF) is important because it represents the limit on the size and speed of a POC. There is no consensus currently on why a minimum BSF occurs. A minimum BSF was experimentally found for a two-column small scale PSA process for the first time in this study. The reason a minimum BSF occurred in this work was proposed to be due to macropore diffusional resistance.

7.5. Future Work

The primary recommendation for future work is to vary particle size for each of the studies in this dissertation. Currently in literature for small LiLSX particles, a nitrogen MTC has been measured as a function of temperature, pressure, and velocity (this study). Understanding how the MTC varies as a function of particle size is the last variable needed to develop a generalized correlation for LiLSX particles. Shrinking particle size may also increase pressure drop enough such that it impacts the minimum BSF. Furthermore, running a small scale process with a different particle size would help confirm that macropore diffusional resistance causes the minimum BSF. Other possible future work includes measuring a minimum BSF with larger diameter columns (more representative of industrial small scale systems) and demonstrating how the estimation of the axial dispersion coefficient affects process simulation results.

REFERENCES

1. Oxygen Therapy Market Size & Share, Industry Report, 2024.
<https://www.grandviewresearch.com/industry-analysis/oxygen-therapy-market> (accessed 1/19/2018).
2. Ruthven, D. M.; Xu, Z., Diffusion of oxygen and nitrogen in 5A zeolite crystals and commercial 5A pellets. *Chemical engineering science* **1993**, 48 (18), 3307-3312.
3. Masters, A. F.; Maschmeyer, T., Zeolites—From curiosity to cornerstone. *Microporous and Mesoporous Materials* **2011**, 142 (2), 423-438.
4. Weitkamp, J., Zeolites and catalysis. *Solid State Ionics* **2000**, 131 (1), 175-188.
5. Chica, A., Zeolites: promised materials for the sustainable production of hydrogen. *ISRN Chemical Engineering* **2013**, 2013.
6. Sherman, J. D., Synthetic zeolites and other microporous oxide molecular sieves. *Proceedings of the National Academy of Sciences* **1999**, 96 (7), 3471-3478.
7. Thomas, W. J.; Crittenden, B. D., *Adsorption technology and design*. Butterworth-Heinemann: 1998.

8. Ruthven, F.; Farooq, S., Knaebel, *Pressure Swing Adsorption*. VCH Publishers, New York: 1994.
9. Yang, R. T., *Gas separation by adsorption processes*. Butterworth-Heinemann: 2013.
10. Motoyuki, S., *Adsorption engineering*. Elsevier, Sci. Pub **1990**, 5-61.
11. Grande, C., Advances in Pressure Swing Adsorption for Gas Separation. *ISRN Chemical Engineering* **2012**, 2012, 13.
12. Sircar, S., Pressure Swing Adsorption. *Industrial & Engineering Chemistry Research* **2002**, 41 (6), 1389-1392.
13. Skarstrom, C. W., Method and apparatus for fractionating gaseous mixtures by adsorption. US Patent 2,944,627. 1960.
14. Daniel, D.; De, M. P. G., Process for separating a binary gaseous mixture by adsorption. US Patent 3,155,468. 1964.
15. Pressure equalization depressuring in heatless adsorption. US Patent 3,142,547A. 1964.

16. Chatburn, R. L.; Williams, T. J., Performance comparison of 4 portable oxygen concentrators. *Respiratory care* **2010**, 55 (4), 433-442.
17. Koretsky, M. D., *Engineering and chemical thermodynamics*. Wiley Hoboken, NJ: 2004; Vol. 2.
18. Prausnitz, J. M.; Lichtenthaler, R. N.; de Azevedo, E. G., *Molecular thermodynamics of fluid-phase equilibria*. Pearson Education: 1998.
19. Papai, I.; Goursot, A.; Fajula, F.; Plee, D.; Weber, J., Modeling of N₂ and O₂ adsorption in zeolites. *The Journal of Physical Chemistry* **1995**, 99 (34), 12925-12932.
20. McKee, D. W., Separation of an oxygen-nitrogen mixture. US Patent 3,140,933 1964.
21. Chao, C. C., Process for separating nitrogen from mixtures thereof with less polar substances. US Patent 4,859,217. 1989.
22. Langmuir, I., The adsorption of gases on plane surfaces of glass, mica and platinum. *Journal of the American Chemical society* **1918**, 40 (9), 1361-1403.

23. Mathias, P. M.; Kumar, R.; Moyer, J. D.; Schork, J. M.; Srinivasan, S. R.; Auvil, S. R.; Talu, O., Correlation of Multicomponent Gas Adsorption by the Dual-Site Langmuir Model. Application to Nitrogen/Oxygen Adsorption on 5A-Zeolite. *Industrial & Engineering Chemistry Research* **1996**, *35* (7), 2477-2483.
24. Ruthven, D. M., *Principles of adsorption and adsorption processes*. John Wiley & Sons: 1984.
25. Glueckauf, E., Theory of chromatography. Part 10.—Formulæ for diffusion into spheres and their application to chromatography. *Transactions of the Faraday Society* **1955**, *51*, 1540-1551.
26. Langer, G.; Roethe, A.; Roethe, K. P.; Gelbin, D., Heat and Mass-Transfer in Packed Beds 3. Axial Mass Dispersion. *International Journal of Heat and Mass Transfer* **1978**, *21* (6), 751-759.
27. Haq, N.; Ruthven, D. M., A chromatographic study of sorption and diffusion in 5A zeolite. *Journal of colloid and interface science* **1986**, *112* (1), 164-169.
28. Zhong, G.; Rankin, P. J.; Ackley, M. W. High frequency PSA process for gas separation. US Patent 7,828,878. November 2010.

29. Alpay, E.; Kenney, C. N.; Scott, D. M., Adsorbent particle size effects in the separation of air by rapid pressure swing adsorption. *Chemical Engineering Science* **1994**, 49 (18), 3059-3075.
30. Rao, V. R.; Farooq, S., Experimental Study of a Pulsed-Pressure-Swing-Adsorption Process with Very Small 5A Zeolite Particles for Oxygen Enrichment. *Industrial & Engineering Chemistry Research* **2014**, 53 (33), 13157-13170.
31. Suzuki, M.; Smith, J. M., Axial dispersion in beds of small particles. *The Chemical Engineering Journal* **1972**, 3, 256-264.
32. Wu, C.-W.; Kothare, M. V.; Sircar, S., Column Dynamic Study of Mass Transfer of Pure N₂ and O₂ into Small Particles of Pelletized LiLSX Zeolite. *Industrial & Engineering Chemistry Research* **2014**, 53 (45), 17806-17810.
33. Chai, S. W.; Kothare, M. V.; Sircar, S., Rapid Pressure Swing Adsorption for Reduction of Bed Size Factor of a Medical Oxygen Concentrator. *Industrial & Engineering Chemistry Research* **2011**, 50 (14), 8703-8710.
34. Rao, V. R.; Farooq, S.; Krantz, W. B., Design of a two-step pulsed pressure-swing adsorption-based oxygen concentrator. *AIChE Journal* **2010**, 56 (2), 354-370.

35. Rao, V. R.; Kothare, M. V.; Sircar, S., Novel design and performance of a medical oxygen concentrator using a rapid pressure swing adsorption concept. *AIChE Journal* **2014**, *60* (9), 3330-3335.
36. Santos, J. C.; Portugal, A. F.; Magalhães, F. D.; Mendes, A., Simulation and Optimization of Small Oxygen Pressure Swing Adsorption Units. *Industrial & Engineering Chemistry Research* **2004**, *43* (26), 8328-8338.
37. Santos, J. C.; Portugal, A. F.; Magalhães, F. D.; Mendes, A., Optimization of Medical PSA Units for Oxygen Production. *Industrial & Engineering Chemistry Research* **2006**, *45* (3), 1085-1096.
38. Zhu, X.; Liu, Y.; Yang, X.; Liu, W., Study of a novel rapid vacuum pressure swing adsorption process with intermediate gas pressurization for producing oxygen. *Adsorption* **2017**, *23* (1), 175-184.
39. Ackley, M. W.; Barrett, P. A.; Stephenson, N. A.; Kikkinides, E. S., High rate compositions. US Patent 9,533,280 B2. 2017.
40. Ackley, M. W.; Smolarek, J.; Leavitt, F. W. Pressure swing adsorption gas separation method, using adsorbents with high intrinsic diffusivity and low pressure ratios. 14 January 2003.

41. Weston, K.; Jaussaud, D.; Chiang, R. L. Lithium exchanged zeolite X adsorbent blends. US Patent 7,300,899 B2. 2007.
42. Zheng, J.; Barrett, P. A.; Pontonio, S. J.; Stephenson, N. A.; Chandra, P.; Kechagia, P., High-rate and high-density gas separation adsorbents and manufacturing method. *Adsorption* **2014**, *20* (1), 147-156.
43. Garg, D. R.; Ruthven, D. M., Performance of molecular sieve adsorption columns: combined effects of mass transfer and longitudinal diffusion. *Chemical Engineering Science* **1975**, *30* (9), 1192-1194.
44. Rezaei, F.; Webley, P., Optimum structured adsorbents for gas separation processes. *Chemical Engineering Science* **2009**, *64* (24), 5182-5191.
45. Chai, S. W.; Kothare, M. V.; Sircar, S., Numerical study of nitrogen desorption by rapid oxygen purge for a medical oxygen concentrator. *Adsorption* **2012**, *18* (2), 87-102.
46. Rao, V. R.; Kothare, M. V.; Sircar, S., Numerical simulation of rapid pressurization and depressurization of a zeolite column using nitrogen. *Adsorption* **2014**, *20* (1), 53-60.
47. Vemula, R. R.; Kothare, M. V.; Sircar, S., Anatomy of a rapid pressure swing adsorption process performance. *AIChE Journal* **2015**, *61* (6), 2008-2015.

48. Edwards, M. F.; Richardson, J. F., Gas dispersion in packed beds. *Chemical Engineering Science* **1968**, 23 (2), 109-123.
49. Moulijn, J. A.; Van Swaaij, W. P. M., The correlation of axial dispersion data for beds of small particles. *Chemical Engineering Science* **1976**, 31 (9), 845-847.
50. Wakao, N.; Kaguei, S.; Nagai, H., Effective diffusion coefficients for fluid species reacting with first order kinetics in packed bed reactors and discussion on evaluation of catalyst effectiveness factors. *Chemical Engineering Science* **1978**, 33 (2), 183-187.
51. Gritti, F.; Guiochon, G., General HETP equation for the study of mass-transfer mechanisms in RPLC. *Analytical chemistry* **2006**, 78 (15), 5329-5347.
52. Moran, A.; Talu, O., Role of Pressure Drop on Rapid Pressure Swing Adsorption Performance. *Industrial & Engineering Chemistry Research* **2017**, 56 (19), 5715-5723.
53. Chai, S. W.; Kothare, M. V.; Sircar, S., Rapid Pressure Swing Adsorption for Reduction of Bed Size Factor. *Industrial & Engineering Chemistry Research* **2011**, 50, 8703-8710.

54. Turnock, P. H.; Kadlec, R. H., Separation of nitrogen and methane via periodic adsorption. *AIChE Journal* **1971**, *17* (2), 335-342.
55. Jones, R. L.; Keller, G. E., Pressure swing parametric pumping—a new adsorption process. *J. Separ. Proc. Technol* **1981**, *2* (3), 17.
56. Jee, J.-G.; Lee, J.-S.; Lee, C.-H., Air Separation by a Small-Scale Two-Bed Medical O₂ Pressure Swing Adsorption. *Industrial & Engineering Chemistry Research* **2001**, *40* (16), 3647-3658.
57. Rama Rao, V.; Wu, C. W.; Kothare, M. V.; Sircar, S., Comparative performances of two commercial samples of LiLSX zeolite for production of 90% oxygen from air by a novel rapid pressure swing adsorption system. *Separation Science and Technology* **2015**, *50* (10), 1447-1452.
58. Chai, S. W.; Kothare, M. V.; Sircar, S., Rapid Pressure Swing Adsorption for Reduction of Bed Size Factor of a Medical Oxygen Concentrator. *Industrial & Engineering Chemistry Research* **2011**, *50* (14), 8703-8710.
59. Todd, R. S.; Webley, P. A., Mass-transfer models for rapid pressure swing adsorption simulation. *AIChE Journal* **2006**, *52* (9), 3126-3145.

60. Buzanowski, M. A.; Yang, R. T.; Haas, O. W., Direct observation of the effects of bed pressure drop on adsorption and desorption dynamics. *Chemical Engineering Science* **1989**, *44* (10), 2392-2394.
61. Lu, Z. P.; Loureiro, J. M.; Rodrigues, A. E.; LeVan, M. D., Pressurization and blowdown of adsorption beds—II. Effect of the momentum and equilibrium relations on isothermal operation. *Chemical engineering science* **1993**, *48* (9), 1699-1707.
62. Sundaram, N.; Wankat, P. C., Pressure drop effects in the pressurization and blowdown steps of pressure swing adsorption. *Chemical Engineering Science* **1988**, *43* (1), 123-129.
63. Hart, J.; Battrum, M. J.; Thomas, W. J., Axial pressure gradients during the pressurization and depressurization steps of a PSA gas separation cycle. *Gas Separation & Purification* **1990**, *4* (2), 97-102.
64. Kikkinides, E. S.; Yang, R. T., Effects of bed pressure drop on isothermal and adiabatic adsorber dynamics. *Chemical Engineering Science* **1993**, *48* (9), 1545-1555.
65. Sircar, S.; Golden, T. C., Isothermal and Isobaric Desorption of Carbon Dioxide by Purge. *Industrial & Engineering Chemistry Research* **1995**, *34* (8), 2881-2888.

66. Yang, J.; Park, M.-W.; Chang, J.-W.; Ko, S.-M.; Lee, C.-H., Effects of pressure drop in a PSA process. *Korean Journal of Chemical Engineering* **1998**, *15* (2), 211-216.
67. Zhou, Q., *Pure Component Adsorption of Methane, Ethylene, Propylene and Carbon Dioxide in Silicalite*. Masters Thesis. **2013**.
68. Delgado, J. M. P. Q., A critical review of dispersion in packed beds. *Heat and Mass Transfer* **2006**, *42* (4), 279-310.
69. Patel, M. S., *Evaluation of Mass Transfer Rate in Column of Small LiLSX Particles*. Masters Thesis. **2017**.
70. Kumar, R.; Sircar, S., Skin resistance for adsorbate mass transfer into extruded adsorbent pellets. *Chemical engineering science* **1986**, *41* (9), 2215-2223.
71. Wankat, P. C., *Large-Scale Adsorption and Chromatography (Volumes 1-2)*. **1986**.
72. van Deemter, J. J.; Zuiderweg, F. J.; Klinkenberg, A., Longitudinal diffusion and resistance to mass transfer as causes of nonideality in chromatography. *Chemical Engineering Science* **1956**, *5* (6), 271-289.

73. Knox, J. H., Band dispersion in chromatography—a universal expression for the contribution from the mobile zone. *Journal of Chromatography A* **2002**, 960 (1), 7-18.
74. Knox, J. H., Band dispersion in chromatography—a new view of A-term dispersion. *Journal of Chromatography A* **1999**, 831 (1), 3-15.
75. Cussler, E. L., *Diffusion: mass transfer in fluid systems*. Cambridge university press: 2009.
76. Todd, R. S.; Webley, P. A., Pressure Drop in a Packed Bed under Nonadsorbing and Adsorbing Conditions. *Industrial & Engineering Chemistry Research* **2005**, 44 (18), 7234-7241.
77. Ackley, M. W.; Leavitt, F. W. Rate-enhanced gas separation. US Patent 6,500,234. 2002.
78. Vemula, R. R.; Kothare, M. V.; Sircar, S., Performance of a medical oxygen concentrator using rapid pressure swing adsorption process: effect of feed air pressure. *AIChE Journal* **2016**, 62 (4), 1212-1215.
79. Galbraith, S. D.; McGowan, K. J.; Baldauff, E. A.; Galbraith, E.; Walker, D. K.; LaCount, R. B., Ultra rapid cycle portable oxygen concentrator. U.S. Patent 8,894,751. 2014.

APPENDIX A

PSA MODEL

A.1. Simulation model description

The model is derived under the assumptions of ideal gas behavior, negligible radial concentration and temperature gradients, and axially dispersed plug flow. MATLAB R2014a was used to solve the system of equations presented in this section. The Crank-Nicholson finite differencing method was used to solve the equation through a time and space discretization of the column. Pressure equalization steps are modeled using the same time and space discretization method used for other pressure changing steps in the process.

A.2. Mass balance

The column material balance is represented by the axial dispersed plug flow model:

$$\frac{\partial C_i}{\partial t} = D_L \frac{\partial^2 C_i}{\partial z^2} - \frac{\partial}{\partial z} (u C_i) - \frac{\rho_b}{\varepsilon_b} \frac{\partial n_i}{\partial t} \quad (\text{A1})$$

Axial dispersion is found using a model developed by Wakao and Funazkri¹:

$$D_L = \gamma_1 D_m + \gamma_2 u d_p \quad (\text{A2})$$

where D_m is the molecular diffusivity, u is the interstitial velocity, d_p is the particle diameter, and γ_1 and γ_2 are constants typically assumed to be 0.7 and 0.5 respectively.²

The adsorption rate was described with a linear driving force (LDF) model described as:²

$$\frac{\partial n_i}{\partial t} = k_i (n_i^* - n_i) \quad (\text{A3})$$

LDF coefficients were found from performing breakthrough experiments on the same material in a separate breakthrough apparatus.

A.3. Equilibrium model

Adsorption equilibrium was formulated by the dual-site Langmuir (DSL) model.³ The pure component amount adsorbed, n_i^* , was represented by equation A4 where the equilibrium constants show an Arrhenius relationship to temperature involving adsorption energy and entropy, as expressed by:

$$n_i^* = \frac{n_{s,1} b P}{1 + b P} + \frac{n_{s,2} d P}{1 + d P} \quad (\text{A4})$$

$$b = b_0 \exp\left(\frac{Q_b}{RT}\right) \quad (\text{A5})$$

$$d = d_0 \exp\left(\frac{Q_d}{RT}\right) \quad (\text{A6})$$

For simulation studies, the parameters in Table A1 were used according to equation A7 for binary equilibrium.

$$n_i^* = \frac{n_{s,1} b_i P y_i}{1 + \sum_j b_j P y_j} + \frac{n_{s,2} d_i P y_i}{1 + \sum_j d_j P y_j} \quad (\text{A7})$$

Table A1. Nitrogen and oxygen DSL parameters for LiLSX particles used in simulations.

	Nitrogen	Oxygen
$n_{s,1}$ (mol/kg)	2.025	1.426
$b_0 \times 10^{-6}$ (1/kPa)	0.124	0.158
Q_b/R (K)	3365	2373
$n_{s,2}$ (mol/kg)	2.402	6.177
$d_0 \times 10^{-6}$ (1/kPa)	0.513	3.386
Q_d/R (K)	2263	1211

A.4. Energy balance

The energy balance is broken down into three separate differential equations. The first is described by equation A8 and represents the energy balance of the gas phase.

$$c_{v,g}\varepsilon_b \frac{\partial}{\partial t}(C_T T_g) = k_g \varepsilon_b \frac{\partial^2 T_g}{\partial z^2} - c_{p,g}\varepsilon_b \frac{\partial}{\partial z}(u C_T T_g) - \frac{6(1-\varepsilon_b)h_s}{d_p}(T_g - T_s) - \frac{4h_w}{d_{b,i}}(T_g - T_w) \quad (A8)$$

Equation A9 describes the solid phase energy balance:

$$\rho_b c_{v,a} \frac{\partial}{\partial t} \sum_i^{nc} n_i T_s + \rho_b c_{p,s} \frac{\partial T_s}{\partial t} = (1-\varepsilon_b)k_s \frac{\partial^2 T_s}{\partial z^2} - \rho_b \sum_i^{nc} Q_i \frac{\partial n_i}{\partial t} + \frac{6(1-\varepsilon_b)h_s}{d_p}(T_g - T_s) \quad (A9)$$

where Q_i is found by:

$$Q_i = \frac{Q_b n_{s,1} b_i + Q_d n_{s,2} d_i}{n_{s,1} b_i + n_{s,2} d_i} \quad (A10)$$

The gas solid heat transfer coefficient (h_s) is found from equation A11.

$$h_s = \frac{k_g}{d_p} \left(2 + 1.1 Pr^{\left(\frac{1}{3}\right)} Re^{0.6} \right) \quad (A11)$$

The last energy balance equation is for the column wall and is described as:

$$(\lambda_w^2 - 1) \left(\rho_w c_{p,w} \frac{\partial T_w}{\partial t} - k_w \frac{\partial^2 T_w}{\partial z^2} \right) = \frac{4h_w}{d_{b,i}}(T_g - T_w) - \frac{4h_{ext}}{d_{b,o}}(T_w - T_{amb}) \quad (A12)$$

The gas-wall heat transfer coefficient (h_w) is found from equation A13.

$$h_w = \frac{k_g}{d_p} (12.5 + 0.048 Re) \quad (A13)$$

The external heat transfer coefficient (h_{ext}) was found by using natural convection from the surface of the column.

A.5. Momentum balance

Column pressure drop was modeled using the Ergun equation.⁴

$$-\frac{\partial P}{\partial z} = \frac{150\mu_g (1 - \varepsilon_b)^2 u}{\varepsilon_b^3 d_p^2} + \frac{1.75\rho_g (1 - \varepsilon_b) u^2}{\varepsilon_b^2 d_p} \quad (A14)$$

A.6. Boundary conditions

The mass balance boundary condition for steps with an inlet gas flow is described in equation A15:

$$D_L \left. \frac{\partial C_i}{\partial z} \right|_{z=0} = -u|_{z=0} (C_i|_{z=0^-} - C_i|_{z=0}) \quad (A15)$$

where $z = 0$ is the end of the column where gas is entering and the velocity is set by equation A16 depending on the step.

$$u|_{z=0} = u_{in} \quad (A16)$$

For steps with an outlet gas flow, the boundary condition described by equation A17:

$$\left. \frac{\partial C_i}{\partial z} \right|_{z=L} = 0 \quad (A17)$$

where $z=L$ is the end of the column where the gas is exiting. For constant pressure steps, the total gas concentration at the inlet of the column is fixed. For varying pressure steps, the gas velocity is fixed at the outlet of the column.

The energy balance boundary condition for steps with an inlet gas flow is described in equation A18:

$$k_g \left. \frac{\partial T_g}{\partial z} \right|_{z=0} = -(c_{p,g} + R) C_T u \Big|_{z=0} \left(T_g \Big|_{z=0^-} - T_g \Big|_{z=0} \right) \quad (\text{A18})$$

where $z = 0$ is the end of the column where gas is entering. For steps with an outlet gas flow, the boundary condition is described by equation A19:

$$\left. \frac{\partial T_g}{\partial z} \right|_{z=L} = \left. \frac{\partial T_s}{\partial z} \right|_{z=L} = 0 \quad (\text{A19})$$

where $z=L$ is the end of the column where gas is exiting.

A.7. Model parameters

Table A2. Model parameters used for simulations.

Parameter	Value used in model
d_p (cm)	0.05
ρ_b (g/cm ³)	0.58
ρ_w (g/cm ³)	7.74
ε_b	0.35
ε_p	0.65
$c_{p,w}$ (J/kg-K)	490
$c_{p,s}$ (J/kg-K)	830
k_w (W/m-K)	16
k_s (W/m-K)	1.3
T_{amb} (K)	296.15

APPENDIX B

BREAKTHROUGH EXPERIMENTS

B.1. Tabulated data

Table B1. Results of breakthrough experiments. Inlet conditions: pressure = 267 kPa, ambient temperature, N₂/O₂ gas composition 75/25. Note: superficial velocity and Reynolds number based on average value across MTZ

Trial #	Superficial velocity (cm/s)	Reynolds number	MTC (1/s)	MTZ length (cm)
1	1.1	0.9	0.48	1.06
2	1.4	1.2	0.64	1.02
3	1.7	1.4	0.80	0.96
4	1.9	1.6	1.03	1.01
5	2.2	1.9	1.10	1.03
6	2.2	1.9	1.25	0.97
7	2.5	2.1	1.24	0.93
8	2.8	2.3	1.33	0.92
9	3.3	2.8	1.61	1.00
10	4.4	3.7	2.27	1.07
11	5.5	4.7	3.29	0.98
12	6.6	5.6	3.29	1.10
13	7.7	6.5	4.28	1.10
14	8.9	7.5	3.79	1.27
15	10.0	8.4	4.45	1.26

B.2. Examples of breakthrough profiles

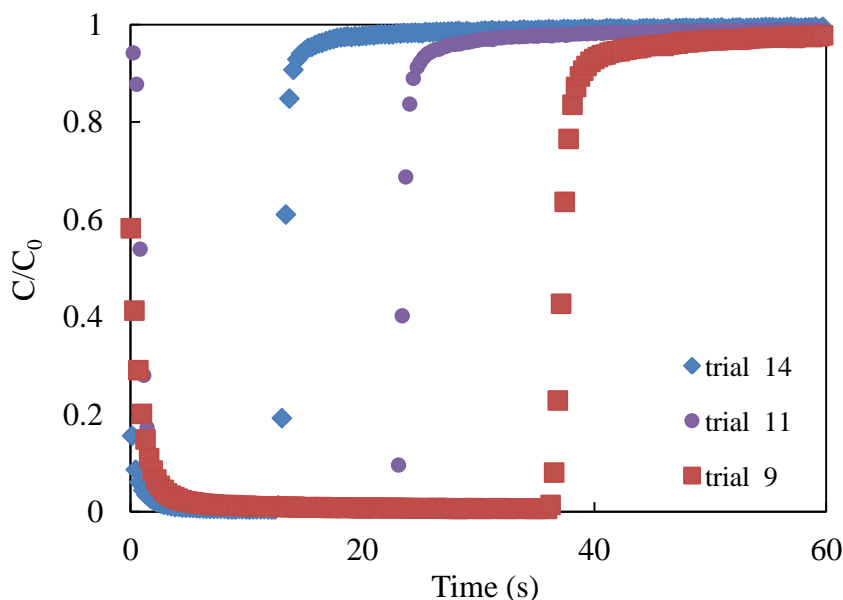


Figure B1. Breakthrough profiles representative of the velocity range covered in the study. Experiments are at inlet conditions described in Table S1. Average Reynolds number across MTZ: trial 14 = 7.5, trial 11 = 4.7, and trial 9 = 2.8

B.3. Heat effects

Figure B2 illustrates the heat effects present in our system. At the exact same conditions as the matched experimental curve, the model was run under isothermal and adiabatic conditions. It is clear that the matched experiment is very near adiabatic conditions. This figure also illustrates how the 0.9 cutoff was determined for defining the MTZ zone. For an isothermal MTZ, 0.95 is the more common cutoff. However, since the adiabatic response is stretched compared to the isothermal one, the location is matched. In other words, a 0.9 cut-off for the adiabatic case provides a reasonable estimate for a 0.95 cut-off on the isothermal curve. Since heat effects are relatively constant in the range of experiments, the difference between the experimental and isothermal curve should also be relatively constant, which justifies using the 0.9

approximation for all the experiments. This approximation is not valid in the gas velocity range below our experimental velocities where heat transfer with the environment is more significant.

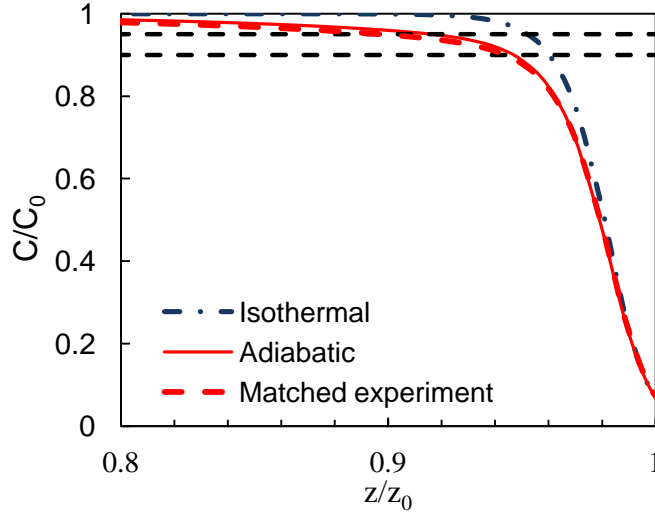


Figure B2. Example of how heat transfer affects experimental results. Matched experiment is run #11. Dashed lines represent 0.95 and 0.9 cutoffs

B.4. Model framework

The amount adsorbed (n_{N_2}) in Equation 5.1 of the main text is found based on the assumption of a constant pattern forming in the column. The constant pattern velocity defined by u_w can be expressed as:⁵

$$u_w = \left(\frac{\partial z}{\partial t} \right)_M = - \left(\frac{\partial M}{\partial t} \right)_z * \left(\frac{\partial z}{\partial M} \right)_t \quad (\text{B1})$$

where M can be molar flux, gas composition, amount adsorbed or temperature. If $N_i = \rho_b n_i + \varepsilon_b C_i$, Equation 3.11 of the main text can be written as Equation B2 assuming plug flow. A differential mass balance at z and t gives:⁵

$$\left(\frac{\partial N_i}{\partial t}\right)_z = -\varepsilon_b \left(\frac{\partial(uC_i)}{\partial z}\right)_t \quad (\text{B2})$$

Equation B1 and B2 are combined to give:

$$u_w = \varepsilon_b \left(\frac{\partial uC_i}{\partial N_i}\right)_z \quad (\text{B3})$$

Assuming the concentration and amount adsorbed ($C_{i,f}$ and $n_{i,f}$) ahead of the MTZ equal zero, Equation B3 can be integrated to get the following relationship inside the MTZ:

$$N_i = \varepsilon_b \frac{uC_i}{u_w} \quad (\text{B4})$$

u_w was found experimentally from Equation 5.4 in main text and the term uC_i can be measured experimentally at the exit (which was numerically found using the simulated exit breakthrough profile that was matched to the experimental curve). The n_i^* in Equation 5.1 is the equilibrium value corresponding to exit gas conditions at that instant. An example of integrand is shown in Figure B3 for one of the runs.

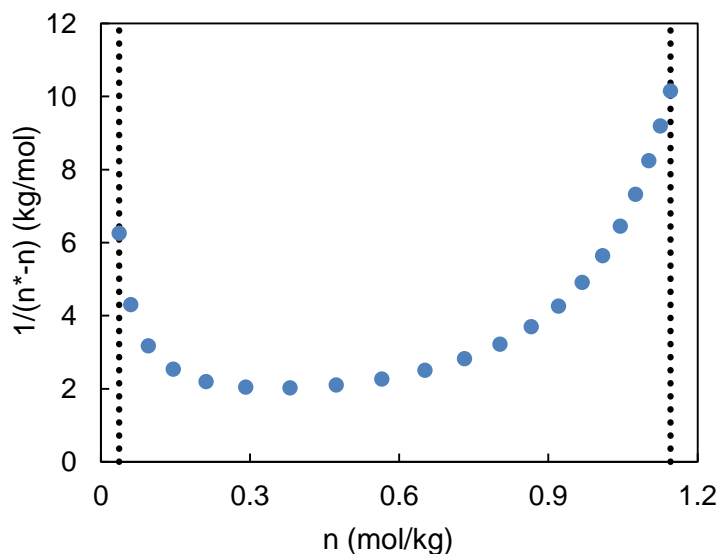


Figure B3. Plot of nitrogen integrand for trial 8 between limits of MTZ ($C/C_0 = 0.05$ and $C/C_0 = 0.9$)

B.5. Void volume analysis

External void volume is known to affect chromatography results and breakthrough column analysis.^{6,7} However, this primarily affects low gas velocity experiments with a dilute feed composition. As has been demonstrated by Rajendran et al.,⁷ it is necessary to correct for the external void volume effects under these conditions. However, they also demonstrate that this correction loses significance for a concentrated feed at high gas velocities, which are the conditions used in this study. Furthermore, the residence time in the void volume for our experimental system was estimated to be over a magnitude lower than the residence time of the MTZ in the column. For example, at the conditions of run #13, it is estimated the residence time in the void volume is ~ 1 s, while the residence time for the MTZ in the column is ~ 23 s.

Despite the previous evidence that suggests the void volume effect is negligible, a brief study on the effect of void volume in our system was first performed for the experimental system. Correcting for external void volume effects usually involves using a zero void bypass column to estimate the effect of the external void volume on the response to breakthrough. This response is then subtracted from the breakthrough curve when the adsorbent material is used. A different and simpler procedure was used just to show that external volume effects in our system were negligible. In our experimental setup, we have the ability to move the mass spectrometer closer to the exit of the column, effectively eliminating half of the external void volume. This prevents us from using the exit flow meter, however, it does allow us to compare the composition response under the same conditions using two different external void volumes.

Two different gas velocities are highlighted to illustrate how the void volume effects change with velocity. The lower velocity example (Figure B4) shows the void volume has a very slight effect on the breakthrough response, but that this difference is not detectable at the higher velocity example in Figure B5. As previously mentioned, void volume effects should affect lower gas velocity experiments more, so this was not a surprising result. Considering all of the experiments in this study was run at gas velocities near the velocity in Figure B4 or much higher, it is reasonable to assume that the void volume affects are negligible for these experiments.

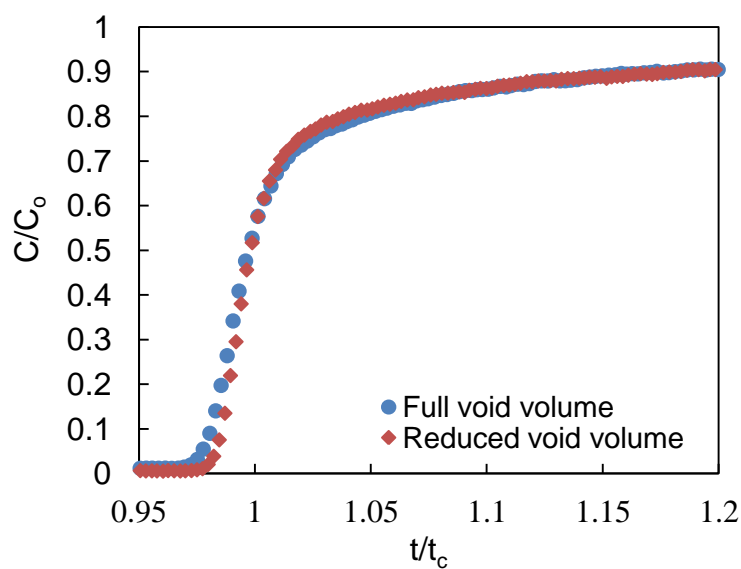


Figure B4. Breakthrough response for two different void volumes. Conditions: superficial velocity: 1.5 cm/s, $N_2/He = 70/30$, pressure: 240 kPa, room temperature

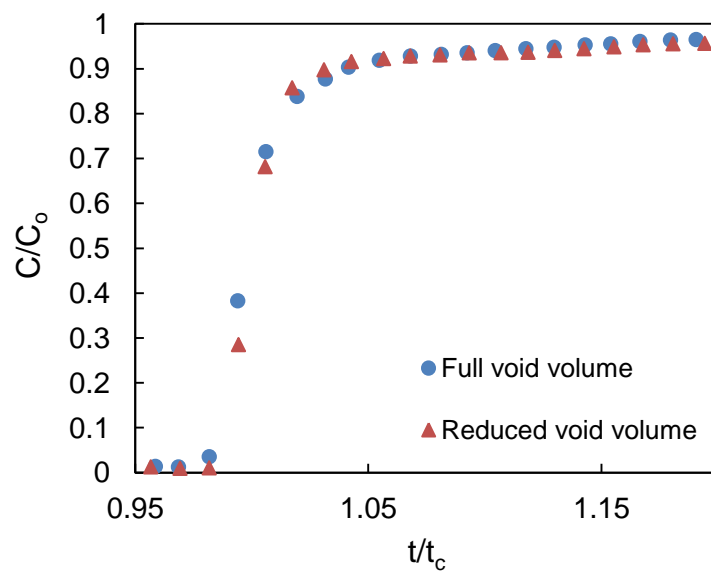


Figure B5. Breakthrough response for two different void volumes. Conditions: superficial velocity: 7.4 cm/s, $N_2/He = 85/15$, pressure: 155 kPa, room temperature

B.6. Effect of using wrong MTC on breakthrough profile

The consequence of using the wrong correlation to predict an overall MTC is visually illustrated in Figure B6. Using the Case 1 prediction from Section 4.1 of the main text results in a significantly steeper breakthrough curve compared to the more accurate Case 4 prediction. The Case 1 prediction results in a nearly two-fold reduction in MTZ time compared to the Case 4 prediction when the 0.05 and 0.9 limits used to define the MTZ are used. Assuming the wave velocities are approximately equivalent, this results in a MTZ length prediction that is nearly twice as small as demonstrated experimentally.

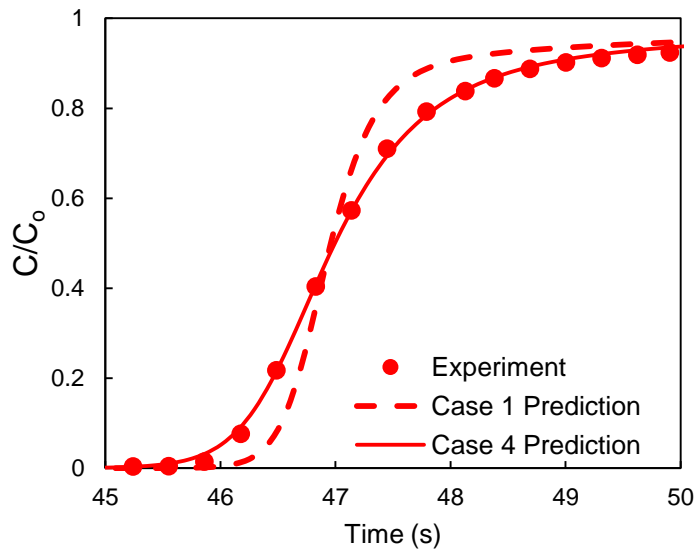


Figure B6. Comparison of breakthrough profiles using different predictions for an overall MTC. Experimental breakthrough curve at 267 kPa, room temperature and an inlet N_2/O_2 gas mixture of 0.75/0.25. The average superficial velocity across MTZ was 2.8 cm/s

APPENDIX C

PRESSURE DROP EXPERIMENTS

C.1. Column pressure profile

Figure C1 provides both simulation and experimental pressure profiles for Cycle #10 at the product end of the process. It demonstrates the simulator captures the pressure change reasonably well when plotted against experimental data. There is some discrepancy between the model and experiment during the high pressure production step. It is difficult to determine if this is due to the experimental setup or a simulation limitation. Nevertheless, it seems to have little effect on the ability of the model to reasonably approximate the oxygen recovery and BSF as evidenced by the comparison of experimental and simulation process results.

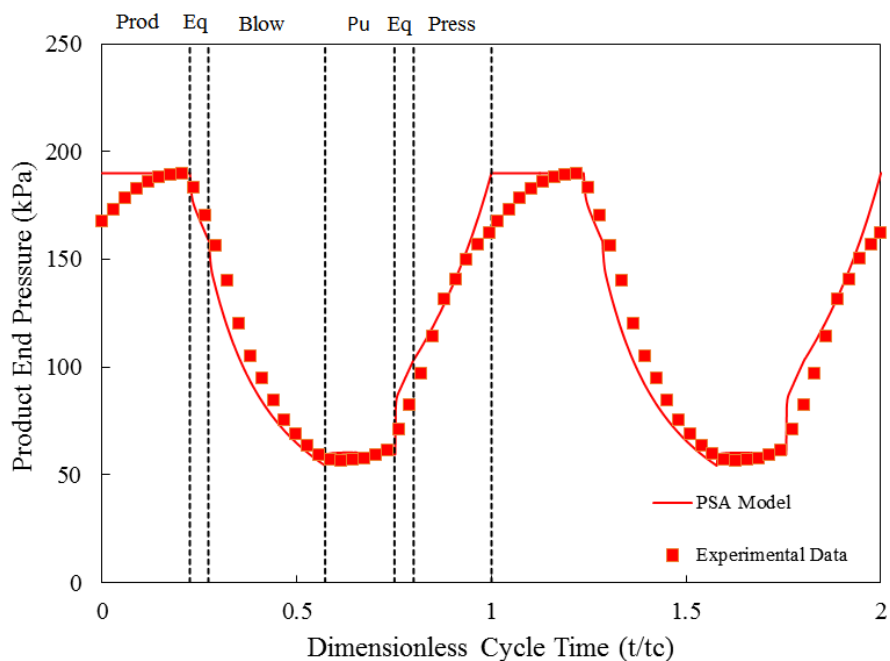


Figure C1. Experimental and simulated pressure profile for Cycle #10.

C.2. Tabulated experimental results

Table C2. Short columns experimental results.

	% Oxygen Recovery	BSF (lbs. solid/TPD O ₂)
Cycle 1	48.2	164
Cycle 2	47.3	114
Cycle 3	45.5	81
Cycle 4	41.0	51

Pressure ratio 4.5, P/F ratio 0.4, product purity:
96% oxygen, production step pressure ~195 kPa

Table C3. Long columns experimental results.

	% Oxygen Recovery	BSF (lbs. solid/TPD O ₂)
Cycle 5	34.5	303
Cycle 6	33.2	219
Cycle 7	30.9	172
Cycle 8	26.3	116
Cycles 5-8: Pressure ratio 2.5, P/F ratio 0.6, product purity: 96% oxygen , production step pressure ~195 kPa		
Cycle 9	51.3	113
Cycle 10	50.3	80
Cycle 11	45.4	55
Cycle 12	43.9	52
Cycles 9-12: Pressure ratio 4.5, P/F ratio 0.4, product purity: 96% oxygen , production step pressure ~195 kPa		

APPENDIX D

MINIMUM BSF EXPERIMENTS

D.1. Tabulated experimental results for minimum BSF study

Table D1. Long columns experimental results, pressure ratio 3.5

	Total cycle time (s)	% Oxygen Recovery	BSF (lbs. solid/TPD O ₂)
Cycle 1	6	18.8	140
Cycle 2	3.9	14.3	119
Cycle 3	3.3	12.7	116
Cycle 4	3.2	11.0	132
Cycle 5	6	19.4	138
Cycle 6	4.2	15.3	123
Cycle 7	3.36	12.2	123
Cycle 8	3.12	11.1	126
Cycle 9	5.28	17.0	140

Pressure ratio 3.5, P/F ratio 0.45, product purity 96%, oxygen
production step pressure ~195 kPa

Table D2. Long columns experimental results, pressure ratio 3

	Total cycle time (s)	% Oxygen Recovery	BSF (lbs. solid/TPD O ₂)
Cycle 10	6.2	15.3	195
Cycle 11	3.1	8.8	167
Cycle 12	2.72	6.6	193
Cycle 13	2.92	7.5	184
Cycle 14	4.9	13.4	176
Cycle 15	3.92	11.6	161

Pressure ratio 3, P/F ratio 0.47, product purity: 96% oxygen , production
step pressure ~195 kPa

Table D3. Long columns experimental results, pressure ratio 2.5

	Total cycle time (s)	% Oxygen Recovery	BSF (lbs. solid/TPD O ₂)
Cycle 16	6.4	10.8	318
Cycle 17	5.3	10.1	276
Cycle 18	3.2	7.0	240
Cycle 19	2.6	3.8	353
Cycle 20	2.9	5.4	276
Cycle 21	2.6	4.2	318
Cycle 22	4.4	9.3	259
Cycle 23	3.8	8.9	231

Pressure ratio 2.5, P/F ratio 0.5, product purity: 96% oxygen , production
step pressure ~195 kPa

Table D4. Short columns experimental results, pressure ratio 3.5

	Total cycle time (s)	% Oxygen Recovery	BSF (lbs. solid/TPD O ₂)
Cycle 24	6	14.5	168
Cycle 25	3.6	9.0	151
Cycle 26	3.1	6.4	175
Cycle 27	3.3	7.6	159
Cycle 28	4.84	12.7	153
Cycle 29	4.2	10.9	151
Cycle 30	8.4	17.0	199
Cycle 31	3.9	9.5	153
Cycle 32	3.5	7.6	170
Cycle 33	3.2	6.3	185

Pressure ratio 3.5, P/F ratio 0.45, product purity 96%, oxygen
production step pressure ~195 kPa

Table D5. Short columns experimental results, pressure ratio 3

	Total cycle time (s)	% Oxygen Recovery	BSF (lbs. solid/TPD O ₂)
Cycle 34	6.4	12.1	226
Cycle 35	6.4	12.2	230
Cycle 36	3.7	7.1	210
Cycle 37	3.2	5.3	235
Cycle 38	2.94	4.3	255
Cycle 39	4.64	9.2	210
Cycle 40	9.28	13.4f	287

Pressure ratio 3, P/F ratio 0.47, product purity: 96% oxygen , production
step pressure ~195 kPa

NOMENCLATURE

b_0 = adsorption equilibrium constant for site 1 of DSL model

C_i = gas phase concentration of species i

$C_{i,f} = C_i$ ahead of MTZ

C_T = total gas phase concentration

$c_{p,g}$ = specific heat of gas

$c_{p,s}$ = specific heat of solid adsorbent

$c_{p,w}$ = specific heat of column wall

$c_{v,a}$ = specific heat of adsorbed phase

$c_{v,g}$ = specific heat of gas

d_0 = adsorption equilibrium constant for site 2 of DSL model

D_L = axial dispersion coefficient

D_m = molecular diffusivity

$d_{b,i}$ = inner column diameter

$d_{b,o}$ = outer column diameter

d_p = adsorbent particle diameter

h_{ext} = wall-ambient heat transfer coefficient

h_s = gas-solid heat transfer coefficient

h_w = gas-wall heat transfer coefficient

k_i = mass transfer coefficient of component i

k_g = gas thermal conductivity

k_s = adsorbent thermal conductivity

k_w = wall thermal conductivity

n_i = adsorbed phase concentration over an adsorbent particle of component i

n_i^* = equilibrium amount adsorbed of component i

$n_{s,1}$ = adsorption equilibrium capacity constant for site 1 of DSL model

$n_{s,2}$ = adsorption equilibrium capacity constant for site 2 of DSL model

$n_{i,f}$ = n_i ahead of MTZ

P = pressure

Pr = Prandtl number

Q_b = heat of adsorption for site 1 of DSL model

Q_d = heat of adsorption for site 2 of DSL model

Q_i = heat of adsorption of component i

R = ideal gas constant

Re = Reynolds number

T = temperature

t = time

tc = time for stoichiometric center to leave column

T_{amb} = ambient temperature

T_g = gas temperature

T_s = solid temperature

T_w = wall temperature

u = interstitial gas velocity

u_w = wave (constant profile) velocity

y_i = gas phase composition of component i

z = axial coordinate

Greek Letters

γ_1 = axial dispersion constant

γ_2 = axial dispersion constant

ε_b = bed/column porosity

ε_p = particle porosity

λ_w = ratio of column outer diameter to inner diameter

μ_g = gas viscosity

ρ_b = column bulk density

ρ_g = gas density

ρ_w = wall density

Subscripts

i,j = component

REFERENCES

1. Wakao, N.; Funazkri, T., Effect of fluid dispersion coefficients on particle-to-fluid mass transfer coefficients in packed beds: correlation of Sherwood numbers. *Chemical Engineering Science* **1978**, *33* (10), 1375-1384.
2. Ruthven, D. M., *Principles of adsorption and adsorption processes*. John Wiley & Sons: 1984.
3. Mathias, P. M.; Kumar, R.; Moyer, J. D.; Schork, J. M.; Srinivasan, S. R.; Auvil, S. R.; Talu, O., Correlation of Multicomponent Gas Adsorption by the Dual-Site Langmuir Model. Application to Nitrogen/Oxygen Adsorption on 5A-Zeolite. *Industrial & Engineering Chemistry Research* **1996**, *35* (7), 2477-2483.
4. Todd, R. S.; Webley, P. A., Pressure Drop in a Packed Bed under Nonadsorbing and Adsorbing Conditions. *Industrial & Engineering Chemistry Research* **2005**, *44* (18), 7234-7241.
5. Wu, C.-W.; Kothare, M. V.; Sircar, S., Column Dynamic Study of Mass Transfer of Pure N₂ and O₂ into Small Particles of Pelletized LiLSX Zeolite. *Industrial & Engineering Chemistry Research* **2014**, *53* (45), 17806-17810.

6. Gritti, F.; Felinger, A.; Guiochon, G., Influence of the errors made in the measurement of the extra-column volume on the accuracies of estimates of the column efficiency and the mass transfer kinetics parameters. *Journal of Chromatography A* **2006**, *1136* (1), 57-72.
7. Rajendran, A.; Kariwala, V.; Farooq, S., Correction procedures for extra-column effects in dynamic column breakthrough experiments. *Chemical Engineering Science* **2008**, *63* (10), 2696-2706.